School of Physics
and Astronomy

Detection, reconstruction and interpretation of unmodelled gravitational-wave transients

Ronaldas Macas

Submitted for the degree of Doctor of Philosophy
School of Physics and Astronomy
Cardiff University

June 30, 2020

Summary of thesis

In this thesis we aim to answer a number of key questions related to unmodelled gravitational-wave (GW) transients, namely: (1) how can we detect an unmodelled GW transient ('burst'); (2) how well can we reconstruct GW burst parameters; (3) how can we infer the structure of an unmodelled GW source based on the observed signal.

Chapter 1 introduces GW astronomy: how gravitational waves are produced, what are the main categories of GW sources, and how GW detectors work. We end the chapter with a summary of the Advanced LIGO (Laser Interferometer Gravitational-wave Observatory) and Virgo observing runs.

In Chapter 2 we describe the most promising sources of unmodelled GW transients such as gamma-ray bursts (GRBs), supernovae (SNe), isolated neutron stars and fast radio bursts (FRBs). We focus on the short GRB–compact binary coalescence (CBC) and long GRB–supernova progenitor models.

In the following chapter (§3) we present X-Pipeline, a coherent search pipeline for GW bursts. We define a theoretical framework necessary to perform a coherent analysis with X-Pipeline, and describe how X-Pipeline can be used for searches for GWs associated with GRBs. In the second part of the chapter we report results of such analyses for the LIGO–Virgo Observing runs 2 and 3a.

Chapter 4 presents a study that answers the question no. 2, i.e. how well can we reconstruct GW burst parameters, especially the waveform $h(t)$. We perform an injection study with BayesWave, a Bayesian parameter estimation algorithm, using binary black hole (BBH) signals in LIGO–Virgo data. We assess BayesWave performance against the first-principle estimates in three key areas: sky localisation accuracy, signal/noise discrimination, and waveform reconstruction accuracy.

Finally, Chapter 5 introduces a novel technique to reconstruct source mass density perturbations $\delta\rho(t, r, \theta, \phi)$ from the GW signal $h(t)$. We start by deriving the algorithm and testing it with multiple sample sources. We describe in more detail why the algorithm is unable to reconstruct the radial evolution of a BBH merger, and provide a Bayesian framework that could solve this issue by including additional constraints. We end the chapter by discussing the method's limitations, possible solutions and future development work.

Contents

List of Figures

List of Tables

"We dance round in a ring and suppose,
But the Secret sits in the middle and knows."

Robert Frost

Interesting but totally useless facts

- Notes taken: 913 pages
- Hours worked: 6240
- Cups of coffee: 0 [1]
- Money spent for computing: $\geq \$28,992$
- Chocolate consumed: $\geq 32\,\mathrm{kg}$

[1] Not accounting for coffee consumed during work travel (conferences, summer schools, etc.) which is essential for any human being.

Acknowledgments

I have been very fortunate to meet many great people in my life. I wish to express my sincere gratitude to those people without whom it would not be possible to write my thesis.

First and foremost, I would like to thank my supervisor Patrick Sutton. Thank you for being professional, always finding time for weekly meetings, and never giving up on a problem and ceasing to amaze me with your theoretical knowledge! We worked on multiple really interesting projects and I had a great time of being supervised by you.

Next I would like to thank Francesco Pannarale who together with Patrick introduced me to gravitational waves during the summer internship here at Cardiff. Both of you motivated me to work hard and choose this career path. Thanks to Francesco for answering all my questions during the first year of PhD and being a friend! I also learned many great things from other supervisors: Kastytis Zubovas and Vladas Vansevicius from FTMC, Chris Messenger, Siong Heng, Graham Woan and Martin Hendry from Glasgow University, Reinhard Prix from AEI Hannover, and Sheila Dwyer from LIGO Hanford.

I have to thank to the whole Cardiff University gravitational physics group. It almost doubled in size during my PhD and I am very happy to see so many people working here at Cardiff! Thanks for answering all my random questions in group meetings and being so friendly.

I also must thank to all members of LIGO and Virgo collaborations for being at the forefront of the gravitational-wave community. You are setting a very high standard on collaborative science and it is outstanding how much the science has progressed since the very first detection GW150914. It is hard to imagine what waits for us!

Thank you also to my examiners for reading my thesis and (hopefully) suggesting how to make it better. I hope you find this thesis topic as interesting as I do.

Special thanks goes to Cardiff University basketball club. I had so much fun during all practices, games and the nights out.

Finally, I would like to thank my family for supporting me through all my life. Thanks to my mom and my grandfather for being the best examples I could ask for. I aspire to be like you.

Collaborative work

The following sections of this thesis contain work that has been co-authored with others:

- Chapter 3 presents results from the most recent LIGO–Virgo observing runs 2 and 3a. This chapter is based on the O2 and O3a LIGO–Virgo collaboration papers, [49] and [74]. The author was on the paper writing team for both of these papers. The author analysed about 1/3 of all GRBs for both observing runs, and produced all figures in mentioned papers that are in Chapter 3. This work used X-Pipeline [144, 177] that has been developed by many people, as well as the LIGO–Virgo data that has been collected and vetted by a collaborative effort.
- Chapter 4 is based on Pannarale, Macas and Sutton (2019) [142] article about assesing BayesWave performance. The author performed the injection study, produced results on the waveform reconstruction, and wrote a significant portion of the paper. This study uses BayesWave that has been developed by many people [60, 114].

Chapter 1

Introduction to gravitational-wave astronomy

In this chapter we will go through the derivation of the weak-field Einstein equations, GW polarisation and the quadrupole moment approximation based on [54] and [159]. We will briefly mention the four main categories of gravitational-wave sources and will describe how an interferometer works. We will finish the chapter with a review of the most recent LIGO–Virgo observing runs.

1.1 Gravitational waves

Einstein back in 1915 proposed that the geometry of spacetime and the mass-energy content of spacetime are fundamentally interlinked [69]. Or as once John A. Wheeler said: 'Spacetime tells matter how to move; matter tells spacetime how to curve' [127]. This mathematically can be expressed in the Einstein field equations

$$R_{\mu\nu} - \frac{1}{2} R\, g_{\mu\nu} \equiv G_{\mu\nu} = 8\pi G\, T_{\mu\nu}\,, \tag{1.1}$$

where $R_{\mu\nu}$ is the Ricci curvature tensor, R is the Ricci scalar and $g_{\mu\nu}$ is the metric. $G_{\mu\nu}$ is the Einstein tensor that defines the curvature of the spacetime, G and c are the Gravitational and speed of light constants respectively, and $T_{\mu\nu}$ is the stress-energy tensor. Since the Ricci tensor and scalar are defined in terms of derivatives of the metric up to second order, Eq. (1.1) is a second order differential equation.

Not even one year later Einstein published an article on the linearized theory of the Einstein field equations that speculated about 'ripples' of the background spacetime known as gravitational waves [70]. Gravitational radiation, similarly to electromagnetic waves, were supposed to carry energy. Einstein himself at the time was skeptical of the detection of such waves because there were no known sources that could produce an observable 'ripple'. Even more, it was not clear if gravitational waves could transfer energy – maybe they were simply an artifact of chosen coor-

dinates? After decades of uncertainty, Richard Feynman at a conference in Chapel Hill in 1957 proposed a thought experiment, the 'sticky bead argument', showing that gravitational waves indeed carry energy [118].

1.1.1 Einstein's equations for weak gravitational fields

Let us consider a spacetime far from any gravitational-wave source such that it is 'nearly' flat. We can define the infinitesimal spacetime interval ds between two points as

$$ds^2 = g_{\mu\nu} dx^\mu dx^\nu, \tag{1.2}$$

where $g_{\mu\nu}$ is the metric tensor.

Then we can approximate such spacetime as a spacetime with a flat Minkowski metric $\eta_{\mu\nu} = diag(-1, 1, 1, 1)$ and a perturbation $h_{\mu\nu}$ on it giving

$$g_{\mu\nu} = \eta_{\mu\nu} + h_{\mu\nu}, \tag{1.3}$$

where

$$|h_{\mu\nu}| \ll 1 \tag{1.4}$$

everywhere in the spacetime. Note that Eq. (1.4) is not valid for *all* coordinate systems, we merely choose coordinates where this equation is correct. Such approximation would not be correct in the strong-field regime, e.g. near a black hole.

Using the Lorentz transformation in Special Relativity for velocity v in the x direction

$$(\Lambda^\mu{}_\nu) = \begin{pmatrix} \gamma & -v\gamma & 0 & 0 \\ -v\gamma & \gamma & 0 & 0 \\ 0 & 0 & 1 & 0 \\ 0 & 0 & 0 & 1 \end{pmatrix}, \gamma = (1 - v^2)^{-1/2}, \tag{1.5}$$

we can transform the metric tensor $g_{\mu\nu}$ (Eq. (1.3)) to another frame moving with velocity v

$$\begin{aligned} g_{\overline{\mu\nu}} &= \Lambda^\mu{}_{\overline{\mu}} \Lambda^\nu{}_{\overline{\nu}} \eta_{\mu\nu} + \Lambda^\mu{}_{\overline{\mu}} \Lambda^\nu{}_{\overline{\nu}} h_{\mu\nu} \\ &= \eta_{\overline{\mu\nu}} + h_{\overline{\mu\nu}}, \end{aligned} \tag{1.6}$$

where we define

$$h_{\overline{\mu\nu}} \equiv \Lambda^\mu{}_{\overline{\mu}} \Lambda^\nu{}_{\overline{\nu}} h_{\mu\nu}. \tag{1.7}$$

We see that the perturbation $h_{\mu\nu}$ transforms as if it is a tensor in Special Relativity even though it is just a part of the metric $g_{\mu\nu}$ in Eq. (1.3). Essentially, we can think of $h_{\mu\nu}$ as a 'tensor' acting on a flat spacetime.

We can also show that Eqs. (1.3) and (1.4) are left identical to the first order

after a small coordinate change produced by a 'vector field' ξ^α

$$x^{\alpha'} = x^\alpha + \xi^\alpha(x^\beta), \tag{1.8}$$

where the components α are functions of position.

Substituting Eq. (1.8) into Eq. (1.3) gives

$$g_{\alpha'\beta'} = \eta_{\alpha\beta} + h_{\alpha\beta} - \xi_{\alpha,\beta} - \xi_{\beta,\alpha} \tag{1.9}$$

where we neglect second or higher order terms.

Comparing our derived Eq. (1.9) with the original $g_{\mu\nu}$ expression in Eq. (1.3) we see that the small coordinate change has effectively changed $h_{\alpha\beta}$ as

$$h_{\alpha\beta} \to h_{\alpha\beta} - \xi_{\alpha,\beta} - \xi_{\beta,\alpha}. \tag{1.10}$$

If $|\xi^\alpha{}_{,\beta}|$ is small, then the new $h_{\alpha\beta}$ is small which is just the same as before in the original expression Eq. (1.3). This is a so called *gauge transformation* which allows us to simplify many equations by choosing a ξ^a that makes $h_{\alpha\beta}$ to have desired properties. In particular, the Riemann tensor $R_{\alpha\beta\mu\nu}$ simplifies to first order as

$$R_{\alpha\beta\mu\nu} = \frac{1}{2}(h_{\alpha\nu,\beta\mu} + h_{\beta\mu,\alpha\nu} - h_{\alpha\mu,\beta\nu} - h_{\beta\nu,\alpha\mu}). \tag{1.11}$$

After a trivial calculation of the Ricci scalar R, the Einstein tensor $G_{\alpha\beta}$ from Eq. (1.1) becomes

$$G_{\alpha\beta} = -\frac{1}{2}\big[\overline{h}_{\alpha\beta,\mu}{}^{,\mu} + \eta_{\alpha\beta}\overline{h}_{\mu\nu}{}^{,\mu\nu} - \overline{h}_{\alpha\mu,\beta}{}^{,\mu} - \overline{h}_{\beta\mu,\alpha}{}^{,\mu} + \mathcal{O}(h^2{}_{\alpha\beta})\big], \tag{1.12}$$

where $\overline{h}_{\alpha\beta}$ is trace reverse tensor $\overline{h}_{\alpha\beta} \equiv h_{\alpha\beta} - \frac{1}{2}\eta_{\alpha\beta}h$.

It can be shown that we can always find a gauge transformation that allows us to set $\overline{h}^{\mu\nu}_{,\nu} = 0$, also known as Lorentz gauge. This allows us to further simplify the Einstein tensor $G_{\alpha\beta}$ as

$$G^{\alpha\beta} = -\frac{1}{2}\Box\overline{h}^{\alpha\beta}, \tag{1.13}$$

where $\Box$ is d'Alembert operator

$$\Box \equiv -\frac{\partial^2}{\partial t^2} + \Delta^2. \tag{1.14}$$

Finally, substituting $G^{\alpha\beta}$ from Eq. (1.13) to Eq. (1.1) and switching indices for consistency $\{\alpha\beta\} \to \{\mu\nu\}$ we arrive at the weak-field Einstein equation

$$\Box\overline{h}^{\mu\nu} = -16\pi T^{\mu\nu}. \tag{1.15}$$

Eq. (1.15) tells that the stress-energy tensor $T^{\mu\nu}$ creates a small perturbation $h^{\mu\nu} \ll 1$

propagating through the spacetime. Also, note that d'Alembert $\Box$ is the wave operator, therefore Eq. (1.15) shows us that $h^{\mu\nu}$ is a wave.

1.1.2 The propagation of gravitational waves

Consider a region of spacetime that is weak-field but not stationary, and far away from any sources. In such case we can use the weak-field Einstein Eq. (1.15) where the stress-energy tensor $T^{\mu\nu} = 0$. After applying boundary conditions we are left with the equation of motion in the transverse-traceless (TT) gauge

$$\Box h^{TT}_{\mu\nu} = 0, \tag{1.16}$$

where $h^{TT}_{\mu\nu}$ is a purely spatial, traceless and transverse object. Following a similar procedure as in electromagnetism, assume that the equation of motion has a complex plane wave solution

$$h^{TT}_{\mu\nu} = C_{\mu\nu} e^{ik_\sigma x^\sigma}, \tag{1.17}$$

where $C_{\mu\nu}$ is a constant and symmetric (0, 2) tensor.

Eq. (1.16) provides a constraint on the wave vector

$$k_\sigma k^\sigma = 0, \tag{1.18}$$

which means that the wave vector is null, and the gravitational wave travels at the speed of light. The component k^0 is simply the frequency of the wave, and so we can write $k^\mu = (w, k^1, k^2, k^3)$. The nullity of $\vec{\mathbf{k}}$ implies

$$w^2 = |\mathbf{k}|^2, \tag{1.19}$$

which is the dispersion relation for gravitational waves. For a wave traveling in the x^3 direction, we write

$$k^\mu = (w, 0, 0, k^3) = (w, 0, 0, w), \tag{1.20}$$

where $k^3 = w$ due to Eq. (1.19). Since the wave is transverse, $k^\mu C_{\mu\nu}$ and also $C_{0\nu}$ both vanish, therefore

$$C_{3\nu} = 0. \tag{1.21}$$

This leaves the only non-zero components C_{11},C_{12}, C_{21} and C_{22}. Because $C_{\mu\nu}$ is traceless and symmetric, the plane wave traveling in x^3 direction with frequency w

is defined by two independent components

$$C_{\mu\nu} = \begin{pmatrix} 0 & 0 & 0 & 0 \\ 0 & C_{11} & C_{12} & 0 \\ 0 & C_{12} & -C_{11} & 0 \\ 0 & 0 & 0 & 0 \end{pmatrix}. \tag{1.22}$$

We will show later that C_{11} and C_{12} correspond to GW strain polarizations h_+ and $h_\times$ respectively.

The effect of waves on free particles

Previously derived equations suggest that gravitational waves should manifest themselves as stretching (or squeezing) of the spacetime. Let us consider an effect of a gravitational wave passing through a ring of particles, similarly to Feynman's suggested example of sticky beads. The distance between particles is defined using geodesic deviation

$$\frac{d^2}{d\tau^2} S^\mu = R^\mu{}_{\nu\rho\sigma} U^\nu U^\rho S^\sigma, \tag{1.23}$$

where $U^\nu(x)$ is a single vector field and S^μ is a separation vector.

For slowly-moving particles Eq. (1.23) to the lowest order becomes

$$\frac{\partial^2}{\partial t^2} S^\mu = \frac{1}{2} S^\sigma \frac{\partial^2}{\partial t^2} h^{TT\mu}{}_\sigma. \tag{1.24}$$

Assuming that a gravitational wave is moving in the x^3 direction, we see that separations are affected only in the S_1 and S_2 directions, i.e. perpendicular to the wave vector just as in electromagnetism.

Before our next step rename the components of $C_{\mu\nu}$

$$h_+ = C_{11},\ h_\times = C_{12}, \tag{1.25}$$

so that

$$C_{\mu\nu} = \begin{pmatrix} 0 & 0 & 0 & 0 \\ 0 & h_+ & h_\times & 0 \\ a & h_\times & -h_+ & 0 \\ 0 & 0 & 0 & 0 \end{pmatrix}. \tag{1.26}$$

For the case where $h_\times = 0$, Eq. (1.24) becomes

$$\frac{\partial^2}{\partial t^2} S^1 = \frac{1}{2} S^1 \frac{\partial^2}{\partial t^2} (h_+ e^{ik_\sigma x^\sigma}) \tag{1.27}$$

and

$$\frac{\partial^2}{\partial t^2} S^2 = -\frac{1}{2} S^2 \frac{\partial^2}{\partial t^2} (h_+ e^{ik_\sigma x^\sigma}) \tag{1.28}$$

which can be solved to the lowest order

$$S^1 = \left(1 + \frac{1}{2}h_+ e^{ik_\sigma k^\sigma}\right) S^1(0) \tag{1.29}$$

and

$$S^2 = \left(1 - \frac{1}{2}h_+ e^{ik_\sigma k^\sigma}\right) S^2(0). \tag{1.30}$$

The solution shows that particles in the $x - y$ plane separated in the x^1 direction will oscillate in the x^1 direction. Similarly, particles separated in the x^2 direction will oscillate in the x^2 direction. Over time, this makes an effect of 'pulsating' + shape as shown in Fig. 1.1. An equivalent analysis can be done for the case where $h_+ = 0$

$$S^1 = S^1(0) + \frac{1}{2}h_\times e^{ik_\sigma k^\sigma} S^2(0) \tag{1.31}$$

and

$$S^2 = S^2(0) + \frac{1}{2}h_\times e^{ik_\sigma k^\sigma} S^1(0). \tag{1.32}$$

Here a ring of particles would oscillate in the shape of $\times$ (Fig. 1.1). It becames clear that both h_+ and $h_\times$ are independent modes of linear polarization of gravitational waves.

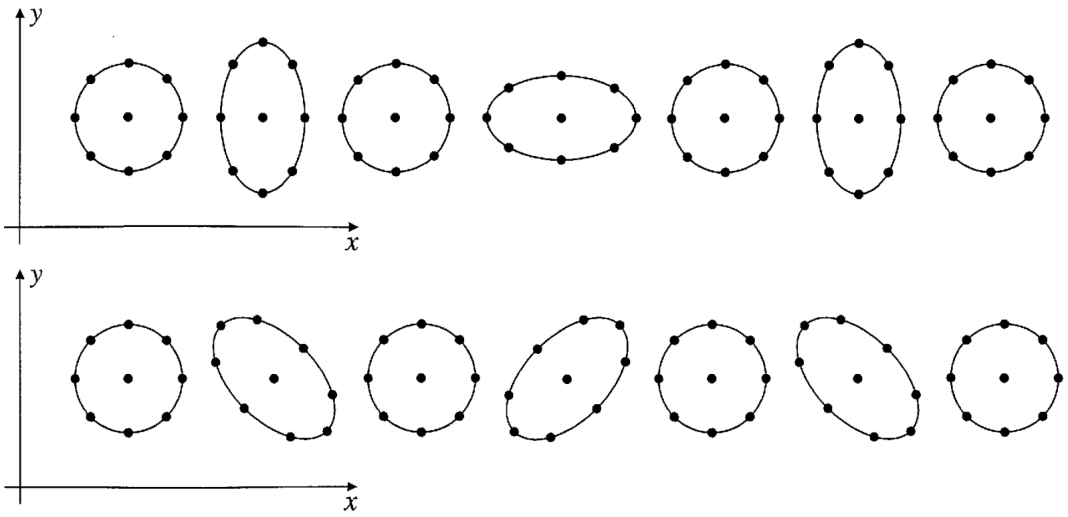

Figure 1.1: Above: the effect of a plus polarisation gravitational wave passing through a ring of particles. Below: the effect of a cross polarisation gravitational wave passing through a ring of particles. The figure was plotted for gravitational-wave strain $h_{+/\times} = \frac{1}{2}$ while realistic sources could produce up to $h = \mathcal{O}(10^{-21})$ at the Earth. Consecutive images show the distortion at moments in time separated by one quarter of the wave period [54].

1.1.3 Production of gravitational waves

We previously saw that gravitational waves are similar to their electromagnetic (EM) counterparts, in particular the wave is transverse and travels at the speed of light. We also know that EM waves are produced by the electric dipole moment. Let us see if that is the case with gravitational waves.

An analogue to the electromagnetic dipole moment is the mass dipole moment $\mathbf{d}$

$$\mathbf{d} = \sum_{A_i} m_i \mathbf{x}_i, \tag{1.33}$$

where m_i is the rest mass and $\mathbf{x}_i$ is the position of a particle A_i.

Following the analogy of electromagnetism, the second derivative of the mass dipole moment should produce radiation. We can see that this is *not* the case because the first derivative of the dipole moment is conserved

$$\dot{\mathbf{d}} = \sum_{A_i} m_i \dot{\mathbf{x}} \equiv \mathbf{p}, \tag{1.34}$$

where $\mathbf{p}$ is the total linear momentum of the system.

We can also see that the gravitational analogue to the magnetic dipole moment μ is conserved too

$$\mu = \sum_{A_i} (\mathbf{x}_i) \times (m_i \mathbf{v}_i) \equiv \mathbf{J}, \tag{1.35}$$

where $\mathbf{J}$ is the total angular momentum of the system. We can conclude that contrary to electromagnetism there is no gravitational dipole radiation. Let us have a look at the next order, quadrupole radiation.

The quadrupolar nature of gravitational waves

Remember that gravitational waves are produced at a source with non-zero stress-energy tensor

$$\Box \overline{h}_{\mu\nu} = -16\pi G T_{\mu\nu}\,. \tag{1.36}$$

As a first step, substitute the Green function $G(x^\sigma - y^\sigma)$

$$\Box_x G(x^\sigma - y^\sigma) = \delta^{(4)}(x^\sigma - y^\sigma), \tag{1.37}$$

which is the solution of the wave equation for delta-function source, to Eq. (1.36). We arrive to

$$\overline{h}_{\mu\nu}(x^\sigma) = -16\pi G \int G(x^\sigma - y^\sigma) T_{\mu\nu}(y^\sigma) d^4 y. \tag{1.38}$$

The solution of $\overline{h}_{\mu\nu}(x^\sigma)$ that represents the accumulated effect of signals to the

past of the points under consideration (a.k.a. 'retarded' Green function) becomes

$$G(x^\sigma - y^\sigma) = -\frac{1}{4\pi|\mathbf{x}-\mathbf{y}|}\delta\big[|\mathbf{x}-\mathbf{y}| - (x^0-y^0)\big]\ \theta(x^0-y^0), \tag{1.39}$$

where we define the spatial vectors $\mathbf{x} = (x^1, x^2, x^3)$ and $\mathbf{y} = (y^1, y^2, y^3)$, with norm $|\mathbf{x}-\mathbf{y}| = [\delta_{ij}(x^i - y^i(x^j - y^j))]^{1/2}$. The theta function $\theta(x^0 - y^0)$ is 1 when $x^0 > y^0$ and zero otherwise.

Using Eq. (1.39) in Eq. (1.38) we get

$$\overline{h}_{\mu\nu}(t,\mathbf{x}) = 4G\int \frac{1}{|\mathbf{x}-\mathbf{y}|}T_{\mu\nu}\left(t - |\mathbf{x}-\mathbf{y}|, \mathbf{y}\right)d^3y. \tag{1.40}$$

Similarly to electromagnetism, we can think of Eq. (1.40) as the accumulated effect at $(t, \mathbf{x})$ of energy and momentum from sources at $(t - |\mathbf{x}-\mathbf{y}|, \mathbf{y})$.

Now we want to see how Eq. (1.40) manifests far away from the source. Consider a non-relativistic source $\phi(t,\mathbf{x}) \equiv T_{\mu\nu}(t,\mathbf{x})$ that is far away oscillating at the frequency w. It is easier to work in the frequency domain here, so let us define the Fourier transform

$$\begin{aligned}\tilde{\phi}(w,\mathbf{x}) &= \frac{1}{\sqrt{2\pi}}\int dt\ e^{iwt}\phi(t,\mathbf{x}),\\ \phi(t,\mathbf{x}) &= \frac{1}{\sqrt{2\pi}}\int dw\ e^{-iwt}\tilde{\phi}(w,\mathbf{x}).\end{aligned} \tag{1.41}$$

Taking the transform of $\overline{h}_{\mu\nu}$ in Eq. (1.40) we get

$$\begin{aligned}\tilde{\overline{h}}_{\mu\nu}(w,\mathbf{x}) &= \frac{1}{\sqrt{2\pi}}\int dt\ e^{iwt}\overline{h}_{\mu\nu}(t,\mathbf{x})\\ &= 4G\int d^3y\ e^{iw|\mathbf{x}-\mathbf{y}|}\frac{\tilde{T}_{\mu\nu}(w,\mathbf{y})}{|\mathbf{x}-\mathbf{y}|}\\ &= 4G\frac{e^{iwr}}{r}\int d^3y\ \tilde{T}_{\mu\nu}(w,\mathbf{x}),\end{aligned} \tag{1.42}$$

where the last step has been based on the assumption that the source is slowly moving and is far away.

The right hand side of Eq. (1.42) can be solved by integration by parts

$$\int d^3y\ \tilde{T}^{ij}(w,\mathbf{y}) = \int \partial_k(y^i\tilde{T}^{kj})d^3y - \int y^i(\partial_k\tilde{T}^{kj})d^3y, \tag{1.43}$$

where the first term is zero because it is a surface integral. For the second term we use the Fourier-space version of the conservation law $T^{\mu\nu}{}_{,\mu} = 0$

$$-\partial_k\tilde{T}^{k\mu} = iw\tilde{T}^{0\mu} \tag{1.44}$$

giving

$$\begin{aligned}\int d^3y\ \tilde{T}^{ij}(w,\mathbf{y}) &= iw\int y^i\tilde{T}^{0j}d^3y \\ &= \frac{iw}{2}\int (y^i\tilde{T}^{0j}+y^j\tilde{T}^{0i})d^3y \\ &= \frac{iw}{2}\int \Big[\partial_k(y^iy^j\tilde{T}^{0k}) - y^iy^j(\partial_k\tilde{T}^{0k})\Big]d^3y \\ &= -\frac{w^2}{2}\int y^iy^j\tilde{T}_{00}d^3y \\ &= -\frac{w^2}{2}\tilde{I}_{ij}(w),\end{aligned} \tag{1.45}$$

where we defined $\tilde{I}_{ij}(t)$ to be the quadrupole moment tensor of the energy density of the source

$$\tilde{I}_{ij}(t) \equiv \int y^iy^jT^{00}(t,\mathbf{y})d^3y. \tag{1.46}$$

This allows us to rewrite Eq. (1.42)

$$\tilde{\bar{h}}_{ij}(w,\mathbf{x}) = -2Gw^2\ \frac{e^{iwr}}{r}\tilde{I}_{ij}(w) \tag{1.47}$$

or alternatively in the time domain

$$\bar{h}_{ij}(t,\mathbf{x}) = \frac{2G}{r}\ \frac{d^2I_{ij}(t-|\mathbf{x}-\mathbf{y}|)}{dt^2}. \tag{1.48}$$

Eq. (1.48) shows that gravitational radiation is produced by a quadrupole moment at leading order. Contrary to the electromagnetic force, mass charge is only positive, therefore it makes sense that gravitational waves require quadrupole radiation, i.e. one order further than the dipole radiation for electromagnetism.

Note that this derivation made a number of assumptions, in particular we supposed that the source is slowly moving and is far away. Such simplifications allowed us to neglect all terms of $\mathcal{O}(r^{-2})$ and even some $\mathcal{O}(r^{-1})$ terms that are not dominant in the slow-motion approximation. Due to these reasons Eq. (1.48) is called quadrupole moment *approximation*.

1.2 Gravitational-wave sources

According to the quadrupole approximation Eq. (1.48), gravitational waves are proportional to the second time derivative of the quadrupole moment of the mass-energy density. This essentially means that any non-spherically symmetric accelerating body will emit gravitational waves. Here we will present four main (and *subjective*) categories of GW sources.

1.2.1 Compact binary sources

Probably the best known gravitational wave source is a binary star. In classical physics two bodies orbiting around each other remain in the same orbit indefinitely due to orbital angular momentum conservation. However, Einstein's General Relativity shows that such a source loses angular momentum due to gravitational waves. This in turn shrinks the radius of the orbit further increasing the emission of GWs that eventually leads to a merger of the binary system.

To see how gravitational waves are produced in this case, consider two stars of mass M at a distance R from their common centre of mass. Assuming that the stars are in circular orbit with angular frequency Ω, the path of a star A is expressed as

$$x_A^1 = R\cos\Omega t, \qquad x_A^2 = R\sin\Omega t, \tag{1.49}$$

and for star B

$$x_B^1 = -R\cos\Omega t, \qquad x_B^2 = -R\sin\Omega t. \tag{1.50}$$

The energy density T^{00} of the binary system becomes

$$\begin{aligned} T^{00}(t,\mathbf{x}) = M\delta(x^3)\big[&\delta(x^1 - R\cos\Omega t)\delta(x^2 - R\sin\Omega t) \\ &+ \delta(x^1 + R\cos\Omega t)\delta(x^2 + R\sin\Omega t)\big], \end{aligned} \tag{1.51}$$

which substituting into Eq. (1.46) gives the quadrupole moment

$$\begin{aligned} I_{11} &= 2MR^2\cos^2\Omega t = MR^2(1+\cos 2\Omega t) \\ I_{22} &= 2MR^2\sin^2\Omega t = MR^2(1-\cos 2\Omega t) \\ I_{12} = I_{21} &= 2MR^2(\cos\Omega t)(\sin\Omega t) = MR^2\sin 2\Omega t \\ I_{i3} &= 0. \end{aligned} \tag{1.52}$$

Finally, we use the quadrupole approximation Eq. (1.48) to estimate the metric perturbation $\overline{h}_{ij}$ along the x^3 axis (the orbital axis) to be

$$\overline{h}_{ij}(t,\mathbf{x}) = \frac{8GM}{r}\Omega^2R^2\begin{pmatrix} -\cos 2\Omega t_r & -\sin 2\Omega t_r & 0 \\ -\sin 2\Omega t_r & \cos 2\Omega t_r & 0 \\ 0 & 0 & 0 \end{pmatrix}. \tag{1.53}$$

We can see that gravitational-wave strain is proportional to $1/r$ contrary to electromagnetism's inverse square law $1/r^2$; this is because we measure GW amplitude rather than energy. Also, note that the characteristic frequency of a gravitational wave is 2Ω, i.e. twice the orbital frequency of the binary system.

For a binary system with the following parameters

$$M_{total} \sim 20\,\mathrm{M}_{\odot} \tag{1.54}$$

$$r \sim 100\,\mathrm{Mpc} \tag{1.55}$$

$$f \sim 100\,\mathrm{Hz} \tag{1.56}$$

$$R \sim 10\,\mathrm{R}_{\mathrm{Schwarzschild}} = 10^5\,\mathrm{m} \tag{1.57}$$

the gravitational wave strain is $h \sim 10^{-21}$. This is the typical amplitude of a GW signal we could expect to observe with ground-based interferometers.

More precise calculations of $h(t)$ are done by solving the Einstein equations with the Post-Newtonian expansion and numerical relativity, see Blanchet (2006) [40] and Bishop (2016) [39] for reviews.

GW150914

We saw previously that two orbiting bodies emit gravitational waves that reduces the system's angular momentum and radius. Such systems are expected to produce a maximum gravitational wave strain of $h \sim 10^{-21}$ at 100 Hz, i.e. the last few orbits of the binary system. On September 14, 2015, both LIGO Livingston and Hanford observatories measured excess power that could only be explained as a transient gravitational-wave signal [45]. The signal had characteristic binary merger 'chirping' from 35 to 250 Hz that produced peak GW strain of 1.0×10^{-21}. The best-fit template from matched filtering analysis found that the first-ever detected gravitational-wave signal was caused by a black hole binary system (Fig. 1.2). Two black holes of masses $36^{+5}_{-4}\,M_{\odot}$ and $29^{+4}_{-4}\,M_{\odot}$ merged about 410^{+160}_{-180} Mpc away to produce a secondary black hole of mass $62^{+4}_{-4}\,M_{\odot}$. The mass difference of the final black hole and primary black holes of $3^{+0.5}_{-0.5}\,M_{\odot}$ was radiated away in gravitational waves. The peak GW luminosity was 3.6×10^{56} erg/s, ten times more than the luminosity of the observable Universe in electromagnetic waves [112].

Black hole systems such as GW150914 are probably the strongest sources of gravitational waves. This is due to several reasons. Firstly, a black hole is the most compact source meaning that the quadrupole moment for a given total mass is relatively big in Eq. (1.48). Also, two bodies orbiting around each other form a highly non-linear system compared with, for example, a supernova, which is mostly spherically symmetric. Finally, because of its compactness the merger happens at a higher frequency than any other system of identical mass, and we know that the amplitude of GW strain correlates with frequency ($\bar{h}_{ij} \propto \Omega^2$ from Eq. (1.53)).

Another compact binary coalescence source is a binary neutron star (BNS) system. The first-ever BNS detection GW170817 and its implications for astrophysics are going to be discussed in §2.1.1. There are other compact binary sources such as white dwarfs, yet they are not compact enough to be observed in ground-based

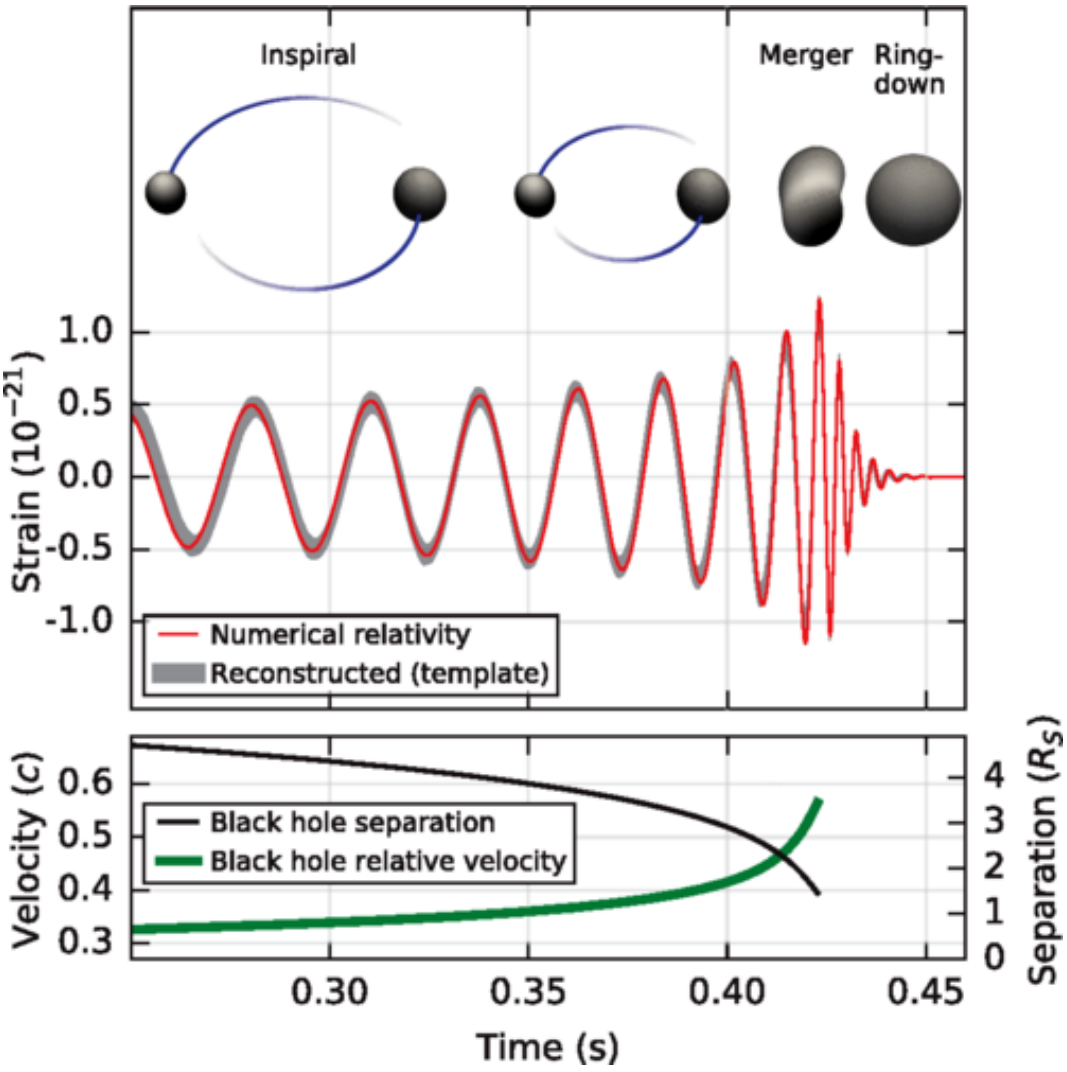

Figure 1.2: The first-ever detection of gravitational waves, GW150914. Above: The signal of compact binary sources has three distinctive phases: inspiral, merger and ringdown. Numerical relativity waveform (red), computed by solving Einstein equations, agrees well with the waveform templated models (grey). Below: Black hole separation (black) and black hole relative velocity (green). Black holes collided being about one Schwarzchild radius away at $\sim 0.6\,c$ velocity. Figure is taken from [45].

detectors due to their sub-Hz merger frequency [89]. As of July 2020, no sources other than compact binaries have been detected with gravitational waves.

1.2.2 Periodic signals

There are sources that emit continuous gravitational waves at almost constant frequency. We expect to observe such waves from an accreting X-ray binary (e.g. Scorpius X-1) where the more massive star is spun-up by accreting matter from the companion star [8]. A highly spinning star with an envelope of accreting matter would have a non-zero quadrupole moment that could be detected. Another potential source is a pulsar. Pulsars are rapidly spinning neutron stars (in the order of 100 Hz rotational frequency) that produce a repetitive beamed emission of electromagnetic waves [85]. It has been suggested that such stars could have an up to 10 cm 'bump' due to the magnetic field making the moment of inertia $I_{ij} \neq 0$ [91]. Such sources would emit much weaker but long-lasting GWs, about $h \sim \mathcal{O}(10^{-25})$ for a system in the Milky Way [94]. Continuous-wave sources have relatively simple waveforms which means that matched filtering techniques can be used. It could be possible to detect $h \sim \mathcal{O}(10^{-25})$ signal by accumulating enough signal-to-noise ratio (SNR) over a long period of time. Most recent LIGO–Virgo studies from Observing run 2 provided upper limits for specific sources such as Scorpius X-1 and for all-sky searches. Currently, the best upper limit is $h_0 \approx 1.7 \times 10^{-25}$ at 120 Hz for an all-sky search [48].

1.2.3 Stochastic background radiation

Similarly to the electromagnetic cosmic microwave background, there should exist a gravitational-wave background. The stochastic GW background is a superposition of many gravitational wave events that originated as early as 10^{-30} s after the Big Bang [65], for example inflation from the early Universe, cosmic strings and many unresolved low SNR binary black hole mergers [12]. The superposition of these and other sources contributes to the stochastic gravitational background. Due to uncertainty in theoretical models, the expected background energy density spectrum $\Omega_{GW}(f)$ varies from 10^{-15} to 10^{-8} [159]. Most recent results produce a limit on the energy density for a background of compact binary coalescences to be $\Omega_{GW} < 4.8 \times 10^{-8}$ at 25 Hz [35].

1.2.4 Bursts

As the name suggests, a GW burst is a short emission of gravitational-wave energy. Potential GW burst sources include core-collapse supernovae (CCSN), long gamma-ray bursts, as well as more exotic scenarios such as cosmic strings and neutron star glitches [9, 128, 137, 169]. Contrary to sources from previous GW categories, GW bursts are hard to model because doing so often requires unknown high energy and

nuclear physics. For example, the core collapse supernovae explosion mechanism is still uncertain, as are the precise physics behind the collapsar model of long gamma-ray bursts. Due to the lack of templates, an unmodelled GW burst search is performed using excess power and coherence methods [47, 100, 117, 144]. While less sensitive than searches with templates, such searches are robust in that they can detect GWs with a priori unknown waveforms. We will discuss one of these searches in more detail in Chapter 3. Some models suggest that a CCSN 10 kpc away could produce $h \sim \mathcal{O}(10^{-21})$ assuming that $10^{-7}\, M_\odot$ radiated in GWs [156].

1.3 Gravitational-wave detectors

As we learned in §1.1, gravitational waves perturb the spacetime. The magnitude of this effect is enormously small within the order of $h \equiv \frac{\Delta L}{L} \approx 10^{-21}$. For comparison, the size of a nucleus is about a Fermi

$$1\,\mathrm{fm} = 10^{-15}\,\mathrm{m}. \tag{1.58}$$

This means that a kilometre-scale gravitational-wave detector must be sensitive to distance changes that are orders of magnitudes smaller than the nucleus' size. One of the most convenient ways to measure such small distance changes is using light.

1.3.1 Michelson interferometer

The Michelson interferometer was used in the famous 1887 Michelson-Morley experiment to disprove the existence of aether, a substance thought to be required for electromagnetic wave propagation through space [126]. The principle of interferometry is quite simple: allow two identical light beams to travel in different directions, reflect them back using mirrors and measure the coherence between the two beams that came back. If there has been a change in length of light travel between the two beams, say caused by aether, then there will be a change in the relative phase of the light waves.

Gravitational-wave interferometers work in a similar way. Firstly, the laser is directed through the input port to the beam splitter. The beam splitter sends light to the X and Y arms (Fig. 1.3), where they bounce back and forth multiple times between test masses in the Fabry-Perot cavity [42]. This allows to build up the power between mirrors making the interferometer more sensitive to a passing gravitational wave. Finally the light beams are combined at the beam splitter and directed to the photodetector. If the optical path length of light in X and Y arms is different, then the incoming wave at the photodetector will be out of phase relatively to the original one.

Let us convince ourselves how a spacetime perturbation can cause a difference in the light travel distance (or time) between the X and Y arms. Consider a grav-

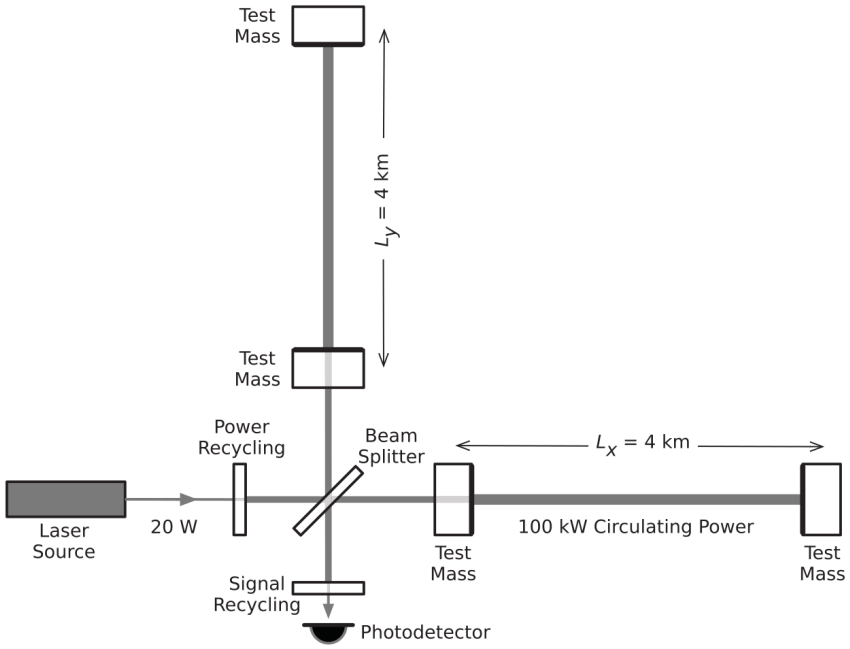

Figure 1.3: Simplified diagram of a gravitational-wave interferometer during LIGO's first observing run in 2015. A 20 W laser produces light that is split into two coherent beams with a beam splitter. Then light travels in the X and Y arms where a Fabry-Perot cavity allows to accumulate 100 kW circulating power. The coherence between the light from the X and Y arms is measured at the photodector. Figure taken from [45].

itational wave traveling in the $\hat{z}$-direction passing through the interferometer with arms of length L positioned along the $\hat{x}$ and $\hat{y}$ directions respectively. The total length of the interferometer arm in the $\hat{x}$-direction is given by

$$\Delta L_x = L(1 + \frac{1}{2}h_{xx}) + \mathcal{O}(h^2) \tag{1.59}$$

which was derived using the geodesic deviation equation (1.23).

For a photon emitted at time t_{start}, the time of the photon arrival at position $x = L$ (in the detector frame) is just the integral of ΔL_x:

$$\begin{aligned} t_{far} &= t_{start} + \int_0^L [1 + h_+(t(x))]^{1/2} dx \\ &= t_{start} + L + \frac{1}{2}\int_0^L h_+(t_{start} + x)dx, \end{aligned} \tag{1.60}$$

where in the second line we assumed that h_+ is small and that $t(x) \approx t_{start} + x$.

Once the photon is reflected back, similar arguments follow to find the total time for the return trip

$$t_{return} = t_{start} + 2L + \frac{1}{2}\int_0^L h_+(t_{start} + x)dx + \frac{1}{2}\int_0^L h_+(t_{start} + L + x)dx. \tag{1.61}$$

When a gravitational wave passes through the interferometer, the gravitational-wave strain h is non-zero which means that t_{return} is different from $t_{start} + 2L$. Therefore we can measure the metric of the wave simply by monitoring the rate of change of the return time as the wave passes. Differentiating Eq. (1.61) with respect to t_{start} gives

$$\frac{\mathrm{d}t_{return}}{\mathrm{d}t_{start}} = 1 + \frac{1}{2}\big[h_+(t_{start} + 2L) - h_+(t_{start})\big]. \tag{1.62}$$

The equation tells us that the rate of change of the return time depends only on the metric at photon emission and receving times, t_{start} and $t_{start} + 2L$ respectively. Note that this result holds as long as the frequency of the light is much higher than the frequency of the gravitational wave.

Here we have considered an example where a GW travels along the $\hat{z}$-direction. In the next section we generalise to the case of an arbitrary propagation direction. We will see that an interferometer is not equally sensitive for all sky directions which leads to the antenna response pattern.

1.3.2 Interferometer antenna pattern

Consider a GW passing through a detector from a general direction. Suppose that the GW is traveling in some local frame of reference (x', y', z') along the $\hat{z}'$-axis. The GW polarisation matrix in the local frame is defined as

$$h'_{ij} = \begin{pmatrix} h'_+ & h'_\times & 0 \\ h'_\times & -h'_+ & 0 \\ 0 & 0 & 0 \end{pmatrix}. \tag{1.63}$$

Now we need to relate the GW frame with the detector frame (x, y, z). The observed h_{ij} in the detector frame is related to that in the local frame by

$$h_{ij} = \mathcal{R}^k_i \mathcal{R}^k_j h'_{kl}. \tag{1.64}$$

$\mathcal{R}$ is the transformation matrix for a rotation over the angle θ around the y'-axis and a rotation over the angle ϕ around the x'-axis

$$\mathcal{R} = \begin{pmatrix} \cos\phi & \sin\phi & 0 \\ -\sin\phi & \cos\phi & 0 \\ 0 & 0 & 0 \end{pmatrix} \begin{pmatrix} \cos\theta & 0 & \sin\theta \\ 0 & 1 & 0 \\ -\sin\theta & 0 & \cos\theta \end{pmatrix}, \tag{1.65}$$

where we assumed the most general case of the GW frame aligned with the polarisation axis. The overall result is that x' and y' axes of the GW frame are aligned with the detector X and Y arms given that z and z' axes are aligned. Figure 1.4 shows the relative orientation of the GW and detector frames.

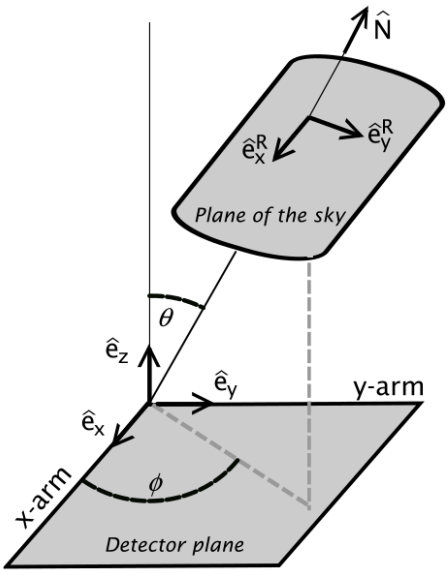

Figure 1.4: Relative orientation of the gravitational-wave and detector frames. Figure taken from [156].

Using Eqs. (1.64) and (1.65) we find that

$$h_+ = \frac{1}{2}h'_+(1+\cos^2\theta)\cos 2\phi + h'_\times \cos\theta \sin 2\phi. \tag{1.66}$$

Eq. (1.66) allows us to express the detector antenna response s as

$$s = F_+(\theta,\phi)h_+ + F_\times(\theta,\phi)h_\times, \tag{1.67}$$

where $F_{+,\times}$ correspond to the antenna response for the respective GW polarisations

$$\begin{aligned} F_+(\theta,\phi) &= \frac{1}{2}(1+\cos^2\theta)\cos 2\phi, \\ F_\times &= \cos\theta \sin 2\phi. \end{aligned} \tag{1.68}$$

Figure 1.5 shows the antenna response $(F_+^2 + F_\times^2)^{1/2}$ for a detector aligned with the $\hat{x}$ and $\hat{y}$ axes. The detector is most sensitive for waves coming from a direction orthogonal to the plane of the detector. The detector also has blindspots where its sensitivity drops to zero, specifically for a wave coming from a direction bisecting the two arms at $\theta = \frac{\pi}{2}, \phi = \pm\frac{\pi}{4}$ or $\phi = \pm\frac{3\pi}{4}$.

The width of antenna patterns makes the gravitational-wave interferometer more similar to a microphone than a telescope. This in turn has its own advantages and disadvantages: the interferometer cannot be pointed at a source therefore has a fixed sensitivity at a sky position relative to Earth, however it 'listens' to the whole sky with an exception of four blindspots. Because GW interferometers directly measure strain, any increase in sensitivity results in roughly a cubic increase in the number of sources, e.g. a two times more sensitive interferometer corresponds to eight times

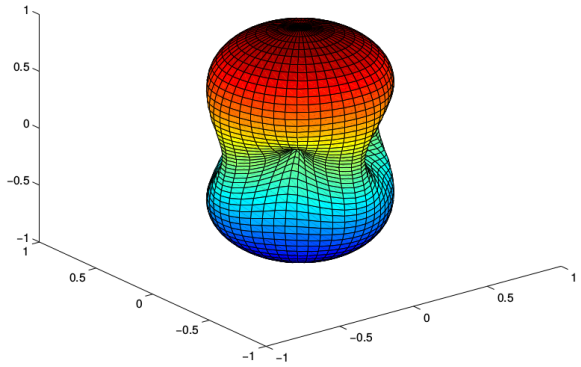

Figure 1.5: Antenna response pattern for an interferometer aligned with the $\hat{x}$ and $\hat{y}$ axes. The plot clearly shows quadrupolar nature of GWs. A detector is most sensitive to directions orthogonal to the plane of the arms. Note that such a design also has four blindspots. Figure taken from [156].

bigger observable volume.

1.3.3 Interferometer noise

The sensitivity of an interferometer to measure changes in strain h varies with frequency. Generally the LIGO detectors are most sensitive around 100 Hz as seen in Fig. 1.6. In order to understand why displacement sensitivity is measured in units of $\mathrm{mHz}^{-1/2}$ we need to look at how the noise is estimated in the first place.

The cross-correlation of two functions $s_1(t)$ and $s_2(t)$ is given by

$$s_1 * s_2(\tau) = \frac{1}{\sqrt{2\pi}} \int_{-\infty}^{\infty} s_1(t) s_2(t+\tau) dt, \tag{1.69}$$

where τ is the time offset [157]. Eq. (1.69) measures how similar functions $s_1(t)$ and $s_2(t)$ are at a time offset τ.

We characterise the noise by cross-correlating the noise with itself as a function of time offset, i.e. we perform auto-correlation. Assuming there is no signal present in the detector, the auto-correlation of noise $s(t)$ in the frequency domain is given by

$$\frac{1}{2} S_n(f) = \int_{-\infty}^{\infty} s * s(\tau) e^{-i2\pi f\tau} d\tau, \tag{1.70}$$

where we defined $s(t) * s(t) \equiv \frac{1}{2} S_n(f)$ to be the Power Spectral Density (PSD), a measure of how noise varies in a detector over frequency.

Auto-correlation is just a number, thus the unit of PSD must be the inverse of Hz. It is rather more common to use Amplitude Spectral Density (ASD), also known as displacement sensitivity, which is the square root of PSD. Figure 1.6 shows LIGO Hanford displacement sensitivity on July 4, 2018. Peak displacement sensitivity is about $4 \times 10^{-20}\,\mathrm{mHz}^{-1/2}$ at 100 Hz which corresponds to $\frac{4\times10^{-20}\,\mathrm{mHz}^{-1/2}\times\sqrt{100\mathrm{Hz}}}{4000\mathrm{m}} =$

1.0×10^{-22} strain sensitivity.

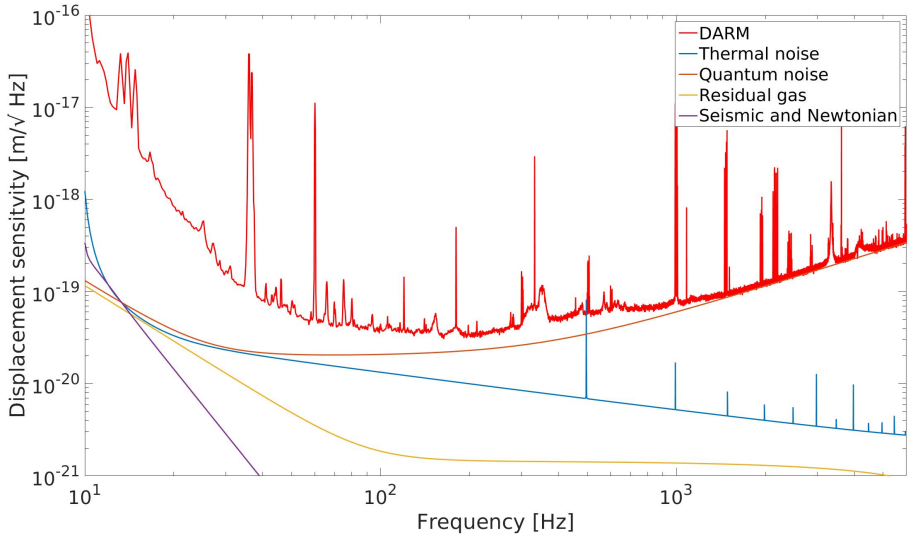

Figure 1.6: LIGO Hanford displacement sensitivity on July 4, 2018 during the second observing run (red). Fundamental noise sources limit detector sensitivity at mid and high frequencies where the residual gas noise is dominating.

In order to understand why Hanford detector is most sensitive around 100 Hz, we need to consider different noise contributions that combined together make a noise budget.

Fundamental noise

There are many noise sources in a detector, ranging from ocean waves hitting the coast to a thirsty raven [67, 152]. While some of them can be mitigated, other sources are so fundamental that they cannot be reduced without drastic detector improvements or redesign. Examples of fundamental noise sources are given below.

Detectors are subject to *thermal noise* caused by thermal fluctuations of the optical mirror coatings and moving test masses. *Quantum noise* arises due to fluctuating laser amplitude in the arm cavities and time uncertainty when photons hit the photodetector. The arms of an interferometer have residual gas molecules that interfere with the laser beam resulting in *residual gas noise*. Furthermore, the ground under the detector moves and wind exerts a force on buildings changing the local gravity field, both characterised as *seismic and Newtonian noise* [31]. These four fundamental noises explain well the higher and mid-frequency noise as seen in Fig. 1.6, however the major contribution of low frequency noise comes from technical noise sources.

Technical noise

Contrary to fundamental noise sources, technical sources, once identified and carefully studied, can be in principle mitigated [64]. Such noise arises from electronics, control loops, charging noise and other similar effects. Figure 1.7 shows three significant low frequency technical noise sources during the second Observing run at the Hanford observatory: *Alignment sensing control*, *Length sensing control* and *jitter*.

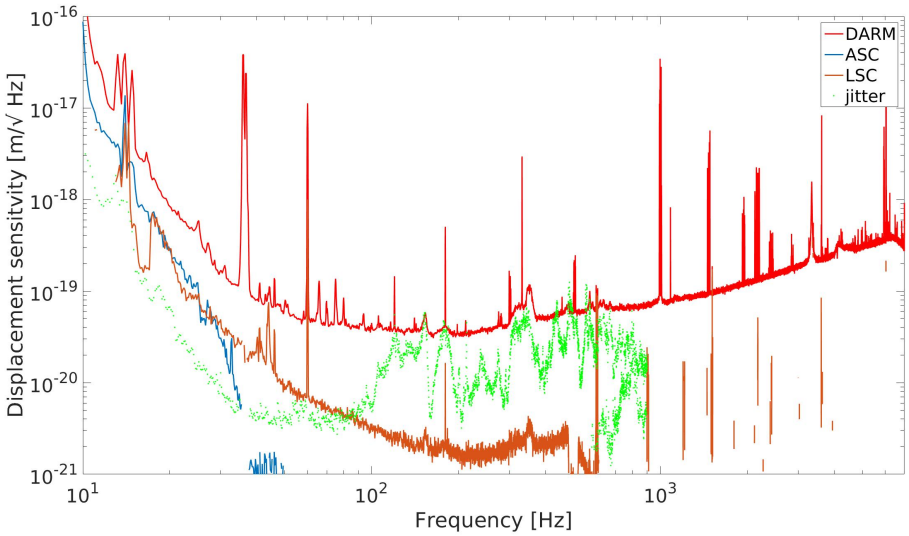

Figure 1.7: Jitter (green) contributes mostly towards mid frequency noise. Alignment sensing control (blue) and length sensing control (brown) are prevelant at lower frequencies. The main contributor to low frequency noise is an unknown mystery noise speculated to be caused by scattering light [31].

Alignment and length sensing control systems strongly couple to differential arm motion (DARM) as their main purpose is to keep the interferometer in lock. Jitter – pointing fluctuations of the laser to a test mass – was more prevelant in the Hanford detector than in the Livingston detector. This particular jitter was caused by a point absorber on one of test masses [19].

Non-stationary noise

Gravitational-wave interferometers are one of the most precise instruments in the world. Because of that detectors are subject not only to stationary and predictable noise sources but also to short and often loud noise transients called *glitches*. They can be caused by a variety of reasons, for example a helicopter flying over an interferometer or a reflected light that couples to a photodetector [36, 139]. Due to their uncertain nature glitches can be misclassified as an excess power in a detector caused by an astrophysical source, potentially leading to a false detection. There are multiple ways to address the issue: glitch classification by machine learning algorithms [120], glitch removal by unmodelled wavelet fitting [60], or requiring coherence

between multiple detector data [144]. The review by Cuoco et al. [72] summarises machine learning techniques that could be used for removing non-stationary noise. The most common technique is to monitor auxiliary and environmental sensor channels; many glitches will appear there whereas GWs will not. The times of glitches in the auxiliary channels can then be used to 'veto' transients at the same time in the GW channel.

1.3.4 Global network

The first LIGO detector was built in 2002 and since then there have been many improvements that increased the sensitivity more than tenfold. As of 2020, there are five detectors in operation: LIGO Livingston, LIGO Hanford, Virgo, KAGRA and GEO600. A global network of interferometers is essential for triangulation and for detecting sources that require coherence, e.g. stochastic and burst signals. See the summary below of detectors that are currently observing or under construction [17].

Advanced LIGO Livingston and LIGO Hanford. Identical 4 km arm length interferometers in Livingston, LA, and Hanford, WA, USA. After an upgrade from the initial LIGO phase, observations began in 2015. The planned design sensitivity of 330 Mpc range for BNS systems should be reached around 2025.

Advanced Virgo. 3 km arm length interferometer near Pisa in Italy. After an upgrade from the initial Virgo phase, observations began in 2017. The planned design sensitivity of 150–260 Mpc should be reached around 2025.

KAGRA. 3 km arm length cryogenically cooled underground interferometer in Japan that started observations in 2020. Planned design sensitivity of at least 130 Mpc should be reached around 2025.

GEO600. 600 m arm length interferometer that is mostly used for testing new tehnologies due to its relatively low sensitivity.

LIGO India. 4 km arm length interferometer that is currently under construction in India. The design of LIGO India is identical to the other LIGO detectors. Construction is estimated to finish around 2025 with target sensitivity of 330 Mpc.

Sky localisation with a network of GW detectors

A single detector is unable to localise a transient source, therefore a network of detectors is required for multi-messenger astronomy. Since gravitational waves travel at the speed of light, we can use the time of arrival of a gravitational wave at a detector to *triangulate* the source.

For two detectors separated by a linear distance $\mathbf{D}$ and a GW source at a position $\mathbf{R}$ on the celestial sphere, the expected difference between time of arrival is given by

$$\Delta t_0 = t_{01} - t_{02} = \mathbf{D} \cdot \mathbf{R}. \tag{1.71}$$

In reality each detector is noisy which means that t_{01} and t_{02} are drawn from distributions rather than delta functions. Triangulation accuracy can be improved by placing detectors as far apart as possible thus increasing the travel time between detectors. In addition, adding more detectors to the network also helps simply by having more measurements of Δt_0, as long as newly positioned detectors are at different locations than other detectors.

Localisation by gravitational wave detectors is relatively poor compared to electromagnetic telescopes. For example, the first ever detection of GW150914 had a 50% localisation area of $150\,\mathrm{deg}^2$ which is orders of magnitude larger than any modern optical telescope. A network of four or even five detectors would allow to localise the source within square degrees of the sky necessary for efficient EM follow-up [77, 78].

1.3.5 LIGO and Virgo observing runs

Observing run 1

Here we briefly mention the most recent LIGO–Virgo observing runs. More detailed information can be found in the Living Reviews article [170].

Initial LIGO underwent an upgrade and began observations in September 2015. The LIGO Hanford and Livingston detectors reached the sensitivity of $\sim 80\,\mathrm{Mpc}$ and 70 Mpc respectively, and observed for about three months. During Observing run 1 (O1) the first ever direct detection of gravitational waves was made, GW150914, as well as other two binary black hole signals were observed, GW151012 and GW151226 [27, 28].

Observing run 2

The second observing run started on November 30, 2016 with Virgo joining in August 1, 2017. LIGO Hanford and Livingston detectors improved their sensitivities up to $80 - 100\,\mathrm{Mpc}$ while Virgo has reached 25 Mpc range. During the nine month observing run seven black hole mergers as well as the merger of a BNS system GW170817 have been detected [19].

Observing run 3

LIGO–Virgo third observing run started on April 1, 2019 and ended on March 27, 2020 due to COVID-19 pandemic [110]. During the first part of observations LIGO Livingston, LIGO Hanford and Virgo detectors were sensitive up to the BNS range of 135 Mpc, 108 Mpc and 45 Mpc respectively [73]. A total of 80 public alerts were published of possible GW detections, however 24 were retracted leaving 56 possible candidate events for the third observing run [109]. For an event to be considered a public alert the false-alarm-rate (FAR) threshold of $3.8 \times 10^{-8}\,\mathrm{Hz}$ (one per 10

months) for CBC searches or 7.9×10^{-9} Hz (one per 4 years) for unmodelled burst searches must be passed. Candidate events ranked by the highest probability origin are as follows:

- 38 BBH systems
- 6 BNS systems
- 5 NS–BH systems
- 4 Mass gap systems[1]
- 3 Terrestial

Postface

In this chapter we have introduced the theoretical background for gravitational waves: we have derived Einstein's equations for weak gravitational fields, used these equations to define two polarisations, and revealed the quadrupolar nature of GWs (§1.1). We also have presented four main categories of GW sources: compact binaries, periodic signals, stochastic background and bursts (§1.2). Finally, we have described gravitational-wave interferometers with their corresponding antenna patterns, as well as the main sources of interferometer noise. We briefly mentioned the current and near future network of GW detectors and summarized the most recent observing runs (§1.3).

In the next chapter we will talk about GW burst sources: short and long gamma-ray bursts, core-collapse supernovae, isolated neutron stars and fast radio bursts. We will also review several examples of physics and astrophysics enabled by GW observations.

[1]Mass gap is a hypothetical mass limit of 3–5$M_\odot$ between the heaviest neutron star and the lightest black hole [103].

Chapter 2

Gravitational-wave bursts

In the previous chapter we solved Einstein's field equations in the weak-field regime, and found that this results in gravitational waves. We also briefly described four main categories of GW sources: compact binary sources, periodic signals, stochastic background radiation and bursts. Furthermore, we presented the basic principle of a GW interferometer and its main noise sources. The chapter ended with a summary of the most recent LIGO–Virgo observing runs.

In this chapter we introduce the most promising sources of unmodelled GW transients ('GW Bursts'). We start by describing gamma-ray bursts, a phenomenon that has been electromagnetically observed for more than 50 years. Subsequent sections discuss supernovae, isolated neutron stars and fast radio bursts, their possible emission mechanisms and expected GW signatures. Finally, the chapter will present the most recent science enabled by multimessenger astronomy with gravitational waves.

2.1 Gamma-ray bursts

Gamma-ray bursts are one of the most violent phenomena in the Universe. These are short bursts of $1 - 1000\,\mathrm{keV}$ energy that vary over miliseconds [119]. Fast variability provides a clue as to what could power a GRB: no physical processes can propagate faster than light, therefore $c\Delta T = 300\,\mathrm{km}$ for $\Delta T = 1\,\mathrm{ms}$. For a comparison, the Sun's diameter is $1.4 \times 10^6\,\mathrm{km}$ meaning that the GRB central engine must be orders of magnitude smaller. However some GRBs can last up to minutes with variability of seconds indicating a much larger scale than $300\,\mathrm{km}$ [93].

The astronomy of GRBs started in a serendipitous way. Back in the Cold War era, the U.S. and the Soviet Union signed a Partial Test Ban Treaty which allowed nuclear weapon tests to be conducted only underground, i.e. no testing in space or oceans. In order to monitor if the Soviet Union complied with the treaty, the U.S. built six satellites to search for signatures associated with nuclear weapon testing. An optical flash of a nuclear explosion could be shielded, however high energy radiation (e.g. X-rays or gamma rays) is harder to mask. Therefore the

network of 'Vela' satellites was built to search for gamma-ray bursts produced by nuclear explosions. While the Vela network detected many gamma-ray signatures related to Earth and Solar activity, e.g. lightning bolts and solar flares (and no bursts related to experiments performed by the Soviet Union), a GRB from July 2, 1967 stood out. It lasted more than eight seconds with variability on a timescale of less than a second, not similar to any of the previously seen bursts. Over the next few years a number of similar unknown origin bursts were detected which led to the idea that these bursts could be of cosmic origin. As a result, Klebesadel, Strong and Olson published a paper 'Observations of Gamma-Ray Bursts of Cosmic Origin' in 1973 [98]. At the time there was a lot of confusion; remember that satellites were supposed to monitor gamma rays from nuclear explosions happening at Earth but the same type of signatures were seen at *cosmic* distances!

At first the origin of cosmic GRBs was unknown. There were a number of explanations ranging from comets colliding with white dwarfs to SN explosions in other galaxies. The review by Nemiroff (1994) [134] listed 118 different models attempting to explain the GRB formation. The first substantial breakthrough was done by BATSE (The Burst and Transient Source Experiment) which found that GRBs are isotropically distributed over the sky (Fig. 2.1) [161]. This in turn indicated that GRBs are either: (1) very abundant and close (within 100 pc) range so that no correlation with the Galactic plane is just an observational effect, or (2) of cosmological origin so that the isotropic distribution is a result of the homogeneous and isotropic Universe. Unfortunately, gamma rays could not be used for distance measurements without having prior information about the source itself, for example instrinsic brightness. Distance estimation required finding a GRB counterpart in other wavebands to measure the spectroscopic redshift. With this in mind Italy and the Netherlands constructed BeppoSAX, a joint satellite that was able to pinpoint a GRB within a sky area of a few arcminutes instead of degrees like BATSE [2]. After less than a year of BeppoSAX's observations, the William Herschel Telescope observed a counterpart of GRB 970228 with an estimated redshift $z = 0.695$ (4.3 Gpc) [151]. This ended the debate about whether GRBs are local or extragalactic phenomena.

A distance measurement allows us to estimate the total energy required to power a GRB. Following the inverse-square law we find that $F = 4.3 \times 10^{-6}\,\mathrm{erg/cm^2}$ of GRB 970228 corresponds to $E_{total} = 5.2 \times 10^{51}\,\mathrm{erg}$ [4]. This is more than ten orders of magnitude bigger than the Sun's output per year. However note that the calculation assumed isotropic emission which might not be the case. Relaxing this assumption would reduce the energy requirements for a progenitor by several magnitudes, as well as imply that we only see GRBs that are directed at us[1]. Nevertheless such enormous energy is available only in extreme single-event cosmological phenomena, such as stellar explosions.

[1] A jet with beaming angle of $\sim 5^\circ$ reduces the energy requirement by factor of 250 [106].

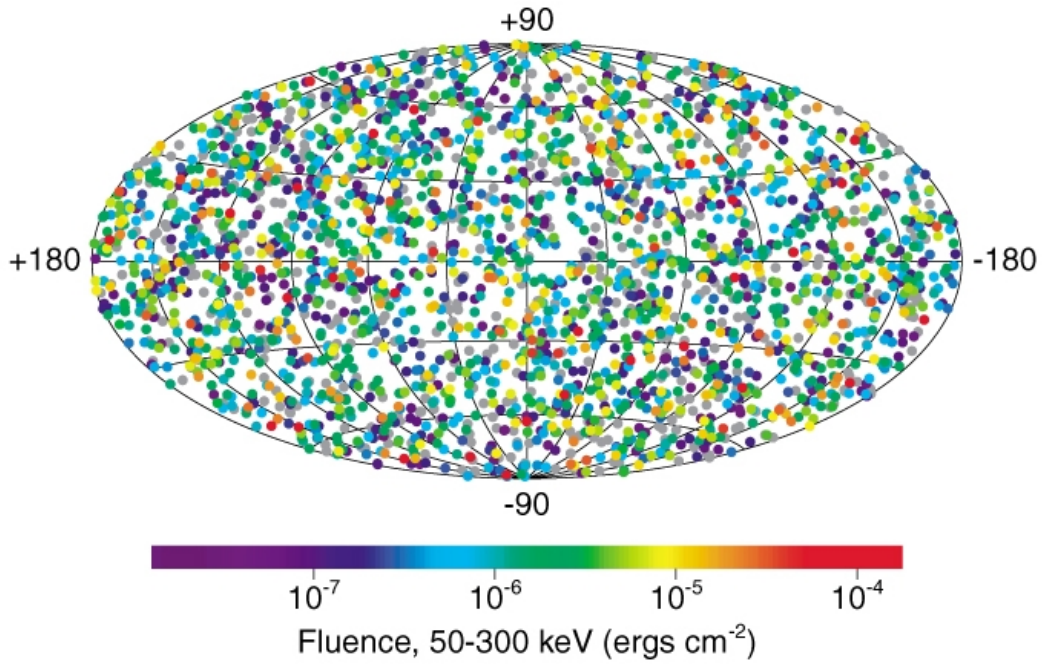

Figure 2.1: Sky position and fluence (time-integrated flux) of 2704 GRBs observed by BATSE. The image clearly shows that GRBs are distributed isotropically through the sky and do not follow the Galactic plane. Figure taken from [1].

In order to explain how a jet (i.e. non-isotropic emission) could be formed in stellar explosions, *the fireball shock* model has been proposed [145]. The model assumes that a large amount of energy has been released in a small volume (we will discuss later mechanisms for short and long GRBs that could provide the required energy). It begins from a radiation dominated phase in which energy from the left-over matter falling into the remnant is carried by photons creating a 'fireball'. As the fireball expands, a matter dominated phase starts with energy from the photons being transferred to the outer layer of left-over matter, mostly protons and electrons. A strong magnetic field directs this fireball to the polar regions where the fireball reacts with the surrounding matter producing multiple shock waves. It is speculated that the GRB jet is formed by neutrino-antineutrino annihilation in exactly these shock waves [105]. Due to internal shocks and magnetic fields, the jet is highly collimated with angle $\theta \approx 2/\gamma$ radians, where γ is the Lorentz factor of the jet with values up to several hundred [82].

Is there any evidence that GRBs are beamed and have highly collimated jets? This question was answered by observing a so called *jet-break*. Assuming that GRBs are beamed, the jet travels freely through the space at relativistic speeds. At some point the relativistic outflow encounters the interstellar medium which slows down the jet. The slowdown of a jet reduces the Lorentz factor given by $\gamma = \gamma_0(t/t_0)^{-3/2}$, where γ_0 is the initial Lorentz factor at time t_0. When a jet is reduced to $\gamma = 1/\theta$, it is considered not to be relativistic any more, and the afterglow is expected to fade

more rapidly. This point of time is when a jet 'breaks out', and has been observed in multiple GRB observations. Figure 2.2 shows the lightcurve of GRB 990510 with a clear break in spectra around 1 day of observations, therefore proving that GRBs are indeed beamed.

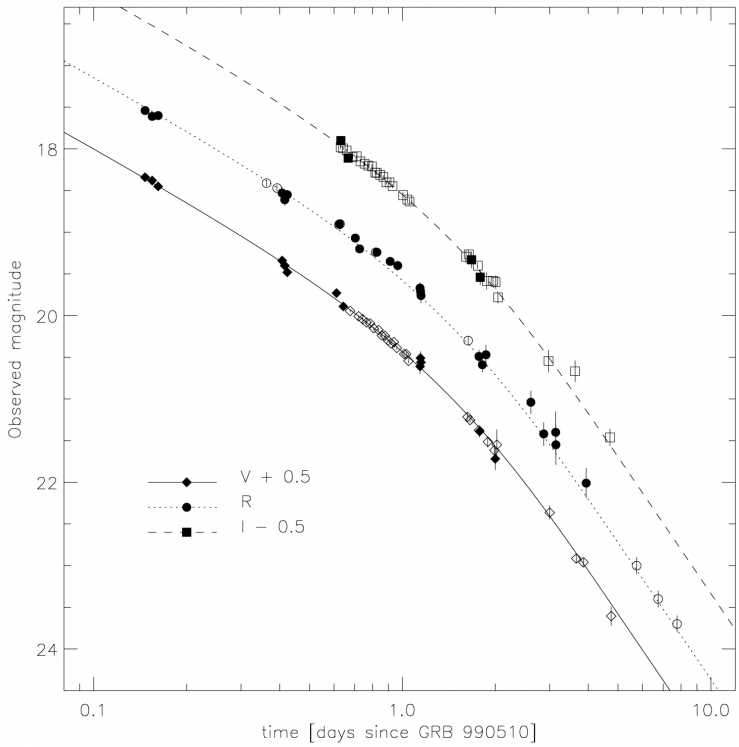

Figure 2.2: The afterglow of GRB 990510 with a rapid break around 1 day of observations. The break in the lightcurve is interpreted as a point in time when the jet 'breaks out' and becomes non-relativistic. An observation of the jet-break proves that GRBs are beamed. Figure taken from [6].

Another important discovery made by BATSE is related to the energy and duration of a GRB. After observing more than a thousand GRBs, it became clear that there are two relatively distinct populations (Fig. 2.3). There are short hard bursts with typical $T_{90\%} \sim 0.5\,\mathrm{s}$ and 300 keV energy, and long soft bursts with typical $T_{90\%} \sim 30\,\mathrm{s}$ and 85 keV energy, all quantities measured in the observer's frame. $T_{90\%}$ is an integrated time when 90% of the total fluence of a GRB lightcurve is observed [2]. Not only are the duration and energy different for the two populations of GRBs, but also the minimum variability time scale of short and long GRB spectra differs by a factor of ~ 10 [121]. Such extreme differences among observed GRBs suggested that there should be at least two different mechanisms responsible for the GRB emission.

[2] $T_{90\%}$ also depends on the equipment used to measure the quantity, so the same GRB could have different $T_{90\%}$ values if estimated by different sensors. In addition, $T_{90\%}$ is a detector frame measured quantity meaning that a GRB at a redshift z lasts a factor of $(1+z)$ longer than in the source frame.

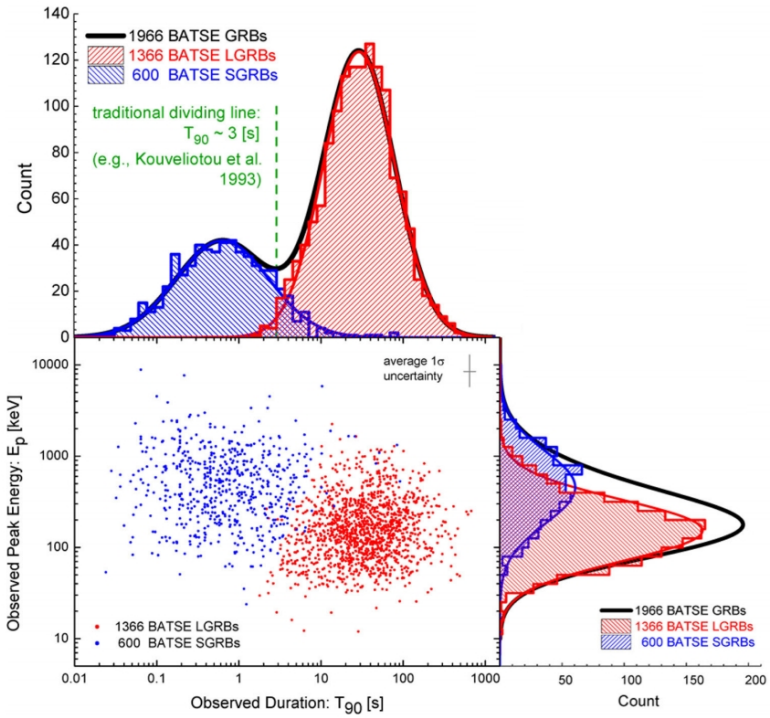

Figure 2.3: Duration $T_{90\%}$ and observed peak energy E_p of 1966 BATSE GRBs. GRBs can be divided in two distinct categories based on their duration: GRBs with $T_{90\%} \sim 0.5\,\mathrm{s}$ are considered to be short and GRBs with $T_{90\%} \sim 30\,\mathrm{s}$ are long. Short and long GRBs have less distinct differences in peak energy E_p: typical $E_{p,\,short} \sim 300\,\mathrm{keV}$ and $E_{p,\,long} \sim 85\,\mathrm{keV}$. On average BATSE observed short and long GRBs with ratio 3:7 respectively. Figure taken from [160].

2.1.1 Short GRB–compact binary connection

It became clear that GRBs must be powered by extremely energetic physical processes in order to explain the observable flux at extragalactic distances. The two most likely scenarios that could provide such an amount of energy are the collapse of a massive star [179] and a merger of two compact objects [108]. The merger of two compact objects seemed to be the more reasonable guess for the progenitor of short GRBs. Firstly, the variability of $\sim 1\,\mathrm{ms}$ in short GRB spectra requires the central engine to be smaller than a stellar-size object [150]. Also, there have been observed BNS systems in our galaxy that will merge within a Hubble time, e.g. the famous Hulse-Taylor binary [88]. Furthermore, the approximate merger rate of binary neutron stars ($< 12,600\mathrm{Gpc}^{-3}\mathrm{yr}^{-1}$) [29] is similar to the inferred rate of short GRBs ($530\mathrm{Gpc}^{-3}\mathrm{yr}^{-1}$) [164] assuming that short GRBs have beaming angle of 20°. Finally, a binary merger system has more than enough gravitational potential energy to power a GRB assuming that accretion is the main energy source. To show this, consider the amount of energy available when the left-over matter after the collision is accreted onto the remnant [41]

$$E_{acc} = \eta M c^2, \tag{2.1}$$

where

$$\eta = \frac{-GMm/r_{large} + GMm/r_{edge}}{mc^2} \approx \frac{GM}{r_{edge}c^2}. \tag{2.2}$$

E_{acc} is amount of energy available for accretion onto the central body of mass M. The efficiency factor η depends on the potential energy difference between the accreted mass m at starting radius r_{large} and accretion radius r_{edge} which is the radius of the central body. For $0.1M_\odot$ accretion onto a remnant with $r_{edge} \sim r_{NS} \sim 10\,\mathrm{km}$, the efficiency factor η is equal to 0.15 [41]. This results to $E_{acc} = 2.7 \times 10^{52}\,\mathrm{erg}$ for a NS which is orders of magnitude bigger than the $E_{iso} = 10^{48} - 10^{51}\,\mathrm{erg}$ required for GRBs.

While there was theoretical and observational evidence suggesting that a binary neutron star could be a short GRB progenitor, for many years there was no direct observation of compact binary coalescence associated with a GRB. This was changed by the LIGO and Virgo gravitational-wave detectors in 2017.

GW170817 – GRB 170817A

On August 17th, 2017, the LIGO Hanford and Livingston interferometers observed the strongest GW signal detected so far with SNR of 32.4 and false-alarm-rate of $2.5 \times 10^{-13}\,\mathrm{Hz}$. It has been identified as a binary neutron star merger GW170817 with $M_{total} = 2.74^{+0.04}_{-0.01}\,M_\odot$ and component masses in the range $1.17 - 1.60\,M_\odot$ that collided $40^{+8}_{-14}\,\mathrm{Mpc}$ away [15]. Just $1.74 \pm 0.05\,\mathrm{s}$ later a short gamma-ray burst, GRB 170817A, was observed by the Fermi and INTEGRAL instruments (Fig. 2.4). In-

terestingly enough, GW170817 was not detected by the Virgo interferometer which meant that the BNS merger was in one of Virgo's blindspots (§1.3.2). The detection by LIGO and non-detection by Virgo together with the localisation from the GRB satellites reduced the localisation area to less than 30 $\deg^2$. Less than eleven hours after the GW170817–GRB 170817A event, the late-time EM emission, i.e. *afterglow*, was observed by optical telescopes. The counterpart named AT2017-gfo was associated with a nearby galaxy NGC 4993 at a distance 40 Mpc away. The identification of an electromagnetic counterpart enabled observations across the EM spectrum ranging from radio to X-ray [87]. Having distance and flux measurements from EM observations, it became evident that GRB 170817 was an extremely faint GRB with $L_{iso} = (1.6 \pm 0.6) \times 10^{47}\,\mathrm{ergs}^{-1}$. This has implications for GRB physics and the viewing angle (discussed more in [32]). The observation of GW170817–GRB 170817A is the first unambiguous association of compact binary star coalescence with a short GRB.

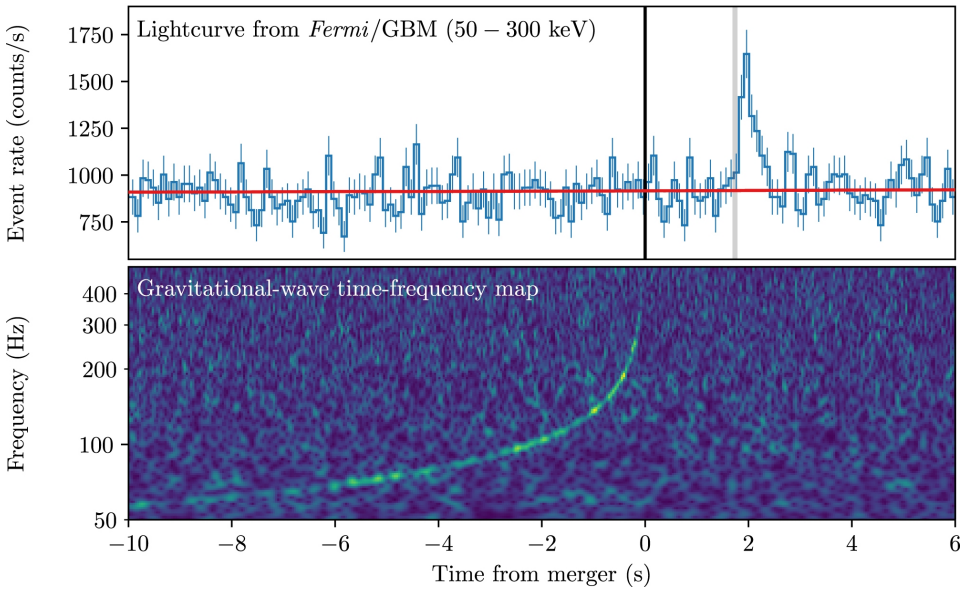

Figure 2.4: Above: Lightcurve of the short GRB 170817A observed by Fermi GBM in the 50 − 300keV range. The red line indicates the background estimated from Goldstein et al. (2016). The vertical black line notes time of the GW170817 merger and the vertical grey line notes the start of GRB 170817A. Below: Time-frequency map of GW170817 observed by LIGO. GRB 170817A arrives about 1.74 ± 0.05 s after the BNS merger GW170817. Figure taken from [32].

The unprecedented follow-up campaign that involved more than 70 observatories allowed astronomers to investigate the short GRB emission mechanism as never before [33]. Two neutron stars of mass $\sim 1.4\,M_\odot$ colliding at relativistic speeds have an enormous amount of kinetic energy[3]. Numerical studies suggest that a GRB jet was produced by about $0.1\,M_\odot$ falling back onto the remnant [63]. It is not clear

[3]Assuming that the BNS collided at $v \sim 0.1\,c$, $E_{kinetic} = 2.5 \times 10^{53}$ erg.

whether the GW170817 event resulted in a black hole or a massive neutron star; this uncertainty is due to: (1) the unknown equation of state (EoS) of a NS, (2) the absence of the post-merger part of the GW signal, and (3) uncertainty in the total mass of the GW170817 merger. The post-merger part of the signal was not seen because of the poor interferometer sensitivity above 1 kHz combined with the relatively weak post-merger GW emission (compared to the inspiral signal) [16]. Unmodelled signal analysis allowed to put a constraint on the GW emission of the post-merger signal. Abbott et al. (2017) estimates an upper limit of 4.8–19.6$M_{\odot}c^2$ energy emitted in the short duration (≤ 1 s) post-merger signal of GW170817 [16]. However, only a few percent of a solar mass is emitted via GWs by a short-lived hypermassive NS according to numerical simulations [79]. This suggests that a post-merger emission from a similar event could be detected only with next-generation detectors.

Further afterglow observations provided more evidence for the BNS merger–GRB connection hypothesis, and yielded new insights into the production of heavy elements. Apart from the GRB jet there was $10^{-3} - 10^{-2}\,M_{\odot}$ material ejected from the system fairly isotropically [14]. Such ejecta produces strong EM radiation also known as a *kilonova* which is a consequence of radiocative decay of heavy r-process [4] elements. The polar kilonova component is more energetic and evolves faster which manifests as optically blue emission. The tidal tail ejecta is less energetic than the polar component and evolves slower (on the order of 10-20 days) resulting in an optically red emission signature. The afterglow of AT2017-gfo had an apparent red component suggesting that the event was observed off-axis (Fig. 2.5). Further EM measurements confirmed this hypothesis and estimated that the GRB was observed about $11 - 33^{\circ}$ off-axis [87], while the more recent analysis by Mogushi et al. (2019) suggests an observing angle of about $7 - 22^{\circ}$ [129]. This could explain why GRB 170817A was unusually faint compared to other GRBs, in fact more than three orders of magnitudes fainter than any other GRB ever observed (see Fig. 4 in [32]).

Neutron star – black hole merger

The observation of GW170817–GRB 170817A proved that BNS mergers can produce a short GRB. Similarly to a BNS system, a binary containing a NS and a BH is also a compact source and has enough gravitational potential energy to power the engine of a GRB [68]. Contrary to the BNS case, a NS-BH binary is not expected to always have an EM counterpart: numerical simulations show that in some cases the NS could be swallowed by the BH without a tidal disruption necessary to power a GRB [80,141]. Whether a NS is disrupted by a BH depends on the equation of state,

[4] The rapid neutron-capture process (r-process) requires to capture neutrons and form stable elements on shorter timescale than the radioactive decay. This is possible only in extremely energetic phenomena like BNS mergers. The r-process is one of the very few nuclear reactions that produces elements heavier than iron.

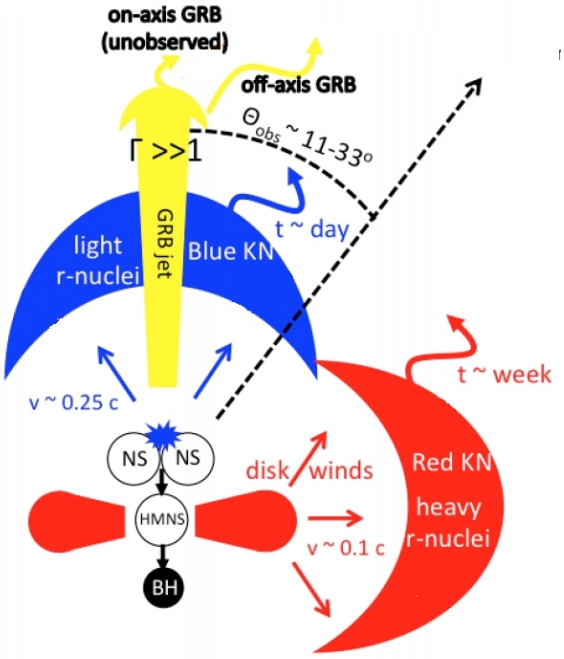

Figure 2.5: Schematic illustration of the EM counterpart for GW170817. The polar region of the kilonova is more energetic and is seen as blue emission while the tidal tail ejecta is slower, less energetic and is seen as red emission. Optical follow-up of GRB 170817A observed not only the blue component but also some part of the red emission component indicating that the event was observed off-axis. Figure taken from [125].

mass and spin of the black hole. For binaries where a non-spinning black hole is about three times more massive than a neutron star (mass ratio $q \leq 3$), tidal forces are too weak to disrupt a neutron star [181]. If a black hole is spinning instead, the innermost stable circular orbit (ISCO) is reduced allowing more massive BHs than $q \geq 3$ to disrupt a NS. For example, a fully spinning BH ($|a_{BH}| = 1$) have six times smaller ISCO than a non-spinning BH [181]. Stone et al. (2013) estimate that the fraction of all short GRBs that could be accounted for NS-BH mergers, f_γ, depends upon the black hole mass and spin distributions, and lies somewhere in between of 0.1–0.3 [162]. There has been no gravitational-wave detection of an NS-BH system powering a GRB so far, however future detection (and non-detection) rates will help to determine the fraction of GRBs that can be accounted by NS-BH mergers [58].

Searching for GWs associated with short GRBs

The detection of GW170817–GRB 170817A proved that short GRBs emit gravitational waves observable by second generation detectors LIGO and Virgo. The GW170817 signal was strong enough to be detected by an online search pipeline, approximately 6 minutes after the signal reached the detectors [33]. For weaker GW signals not detected by the all-sky searches, a targeted matched-filtering analysis with PyGRB has been performed during the advanced detector era [46, 49, 178]. PyGRB uses a phenomenological waveform model that has an inspiral, merger and ringdown parts for two-point particle system [97]. Waveform templates are restricted to NS and BH masses and spins that may produce a GRB via the tidal disruption of the NS [143]. The inclination angle is also constrained to 0° or 180° in order to reduce the false-alarm-ratio at the expense of relatively small loss of GW amplitude [178]. During the LIGO–Virgo observing run O3a PyGRB analysed 32 GRBs and found no significant GW events. Given that there were no significant events, exclusion distances $D_{90\%}$ were estimated for the BNS and NSBH waveforms. Abbott et al. (submitted, [74]) reports 119 Mpc, 231 Mpc, 160 Mpc median exclusion distances $D_{90\%}$ for the BNS, NSBH spin-aligned and NSBH generic spins waveforms, respectively.

2.1.2 Long GRB–supernova connection

Long GRBs are 2–1000 s duration and have softer spectra than short GRBs. In order to explain how long GRBs are formed, a collapsar model was proposed by Woosley in the 1990's [179]. A star is in a equilibrium state when there are two forces counteracting each other: nuclear fusion producing an outward pressure and gravity acting as the inward force. At late stages of the evolution of a massive star, nuclear fusion proceeds until silicon is burned and an iron core is created. At this point fusion stops in the core, and once the nuclear fusion stops the only repulsive force is electron degeneracy pressure. For stars that are above the Chandrasekhar

mass $M = 1.4\,M_\odot$, electron degeneracy pressure is not enough to counteract gravity causing the star to collapse. The collapse generates a shock wave that blows off the outer layers of the star, producing a supernova and a remnant with an accretion disk. The exact mechanism by which this happens is not known; two proposed mechanisms will be discussed in more detail in §2.2. It is believed that for long GRB formation a massive rapidly spinning star is needed to overcome neutron degeneracy pressure and form a BH remnant with an accretion disc rather than a NS remnant.

In order to create a jet, there must be enough material to power the central engine for tens of seconds but at the same time the material should not block the jet. According to Woosley, the polar regions of the ejecta become sufficiently evacuated after several seconds to allow for $> 0.1\,M_\odot$ accretion that creates a highly collimated jet ($\gamma \sim 100$, opening angle only $\sim 5°$). This is a very similar accretion process to the one discussed in §2.1.1 for short GRBs, except that the progenitor is a stellar collapse to a BH instead of a binary star merger.

How can a central engine for long GRBs produce GWs? Both Piro and Pfahl (2007) [146] and Davies et al. (2002) [62] suggest that an accretion disk around a BH could fragment into one nuclear-density lump making a rapidly spinning two compact body system. Such a system could produce $h_{100\,\mathrm{Hz}} = 3\times10^{-22}$ at 100 Mpc [146]. LIGO and Virgo long GRB follow-up searches currently use Accretion Disk Instability (ADI) waveforms that are based on similar arguments. The ADI model argues that GWs are emitted by a magnetically suspended torus that extracts rotational energy from a central BH [172, 173]. This model allows up to $0.25 M_\odot c^2$ energy emitted via GWs for waveforms up to 236 s duration [46] resulting up to $h \sim 10^{-21}$ GWs at 100 Mpc [173].

Multiple observations of long GRBs coincident with supernovae confirm the hypothesis that long GRBs are caused by the collapse of a massive (M_{ZAMS}[5] $\gg 20 M_\odot$) rapidly rotating star. SN 1998bw has been associated with GRB 980425, the closest GRB observed so far observed at only $z = 0.0085$ [168]. Spectra of SN 1998bw did not show prominent hydrogen and helium lines (Type 1c SN) indicating that the progenitor could have been a massive star such as a Wolf-Rayet star. Forming a GRB jet requires a *rapidly spinning* massive star; otherwise polar regions of the remnant cannot be sufficiently evacuated for a jet to escape. This suggests that only Type 1 b/c SN could produce a GRB, and only about 1% of massive stars would have such conditions (remaining 99% of massive stars do not have sufficient angular momentum) [180]. As a result, expected rates of core-collapse supernovae (CCSN) and long GRBs differ by two orders of magnitude: $\mathcal{R}_{CCSN} = (4\text{–}24)\times10^4\,\mathrm{Gpc^{-3}yr^{-1}}$ for CCSN [123] and $\mathcal{R}_{long\ GRB} = (2\text{–}18)\times10^2\,\mathrm{Gpc^{-3}yr^{-1}}$ for long GRBs [55].

The picture of the long GRB–SN connection and the collapsar model is far from complete. Wolf-Rayet stars are thought to be progenitors of long GRBs because they are massive and do not have an outer layer of hydrogen [83]. The main mechanism

[5] M_{ZAMS} - mass of a zero age main sequence star.

to shed the hydrogen layer is through stellar winds. High metallicity stars can blow away up to $10^{-4}\,M_{\odot}\mathrm{yr}^{-1}$ in stellar winds but that also removes the star's angular momentum crucial for the GRB jet formation [41]. Therefore such progenitors are unlikely to produce a rapidly spinning compact object. Recently an alternative route has been proposed: mass transfer to a companion star would allow to form a GRB at the Solar metallicity and beyond [51]. Further afterglow observations and a detection of GWs from long GRBs would provide useful details about the collapsar model and progenitor [92, 146].

2.2 Supernovae

Supernovae are divided in two broad classes based on spectra. Type I SN do not have hydrogen lines indicating that this type of SN lost its outer hydrogen layer while Type II SN has prominent hydrogen lines. Type I SN are further categorized by whether they have prominent silicon and helium lines, and are divided in subtypes *a*, *b* and *c*. All supernovae (Type I b, c and Type II) except for the type Ia are core-collapse origin. Type Ia SN are caused by a thermonuclear explosion of a white dwarf that accreted matter from a companion star. It is expected that both explosion mechanisms (CCSN and thermal runaway) produce gravitational waves, however we will concentrate more on the GW emission from core-collapse SN.

In the previous section we briefly discussed the collapsar model that explained how a massive star collapses under it's own gravity. It is unknown how exactly an explosion (supernova) is created, however there are two suggested mechanisms: neutrino-driven convection and magnetohydrodynamic (MHD) explosion. See Kotake (2012) for a review [102]. In summary, MHD explosions rely on extracting rotational energy of a collapsing progenitor core via magnetic fields. Such an explosion requires a rapidly spinning pre-collapse core that transfers rotational energy to the magnetic field by field wrapping or by the magnetorotational instability [37]. After the inner core collapse is halted by neutron degeneracy and the implosion is rebounded, the magnetic field creates very asymmetric explosions that are essential for producing GWs [176]. However only about 1% of massive stars are expected to have such conditions [180]. The alternative mechanism, neutrino-driven convection, applies to slow or non-rotating collapsing stars. After the bounce shock is formed, neutrinos interact with matter thus creating a 'prompt convection' that produces GWs. Over time a Standing-Accretion-Shock-Instability (SASI) leads to a more violent convection that results in increased GW amplitude. Figure 2.6 summarises neutrino-driven convection and MHD explosion mechanisms.

Detecting gravitational waves from a CCSN would be extremely rewarding. CCSNe are a critical part of stellar evolution, responsible for chemical enrichment of the universe, and they create NSs and BHs. Unfortunately the exact amount of energy that goes to producing GWs is unknown. Some simulations suggest that

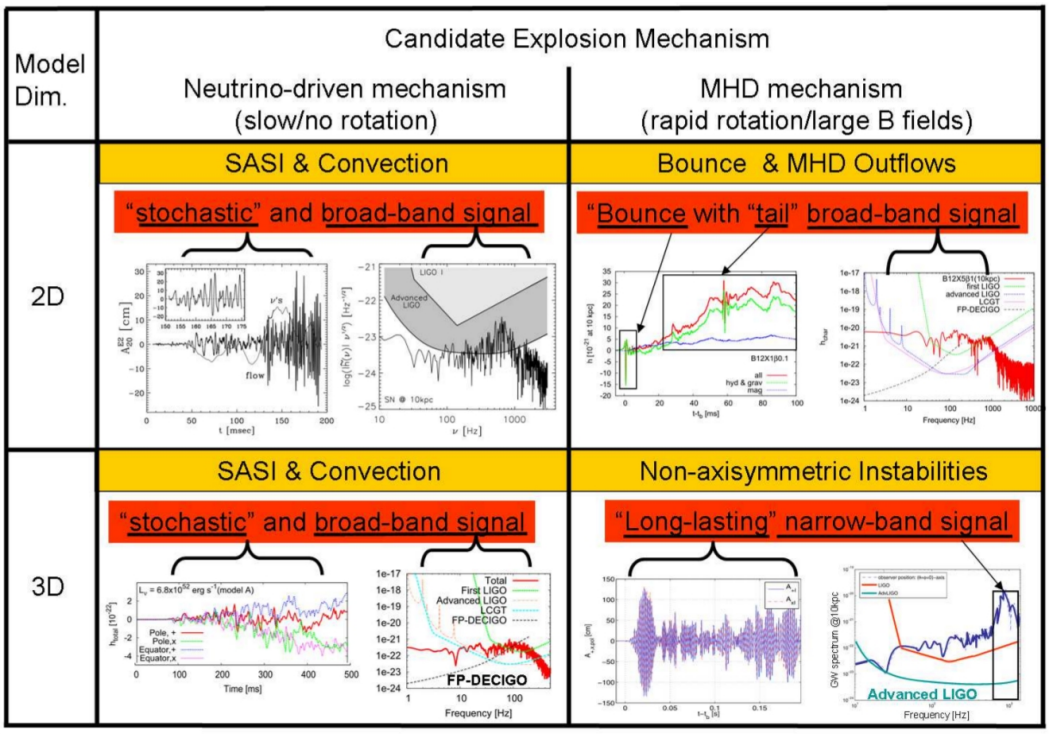

Figure 2.6: Graphical summary of the potential CCSN explosion mechanisms and corresponding emission processes. Yellow color indicates different emission processes while red color indicates GW signatures. Each column has a representative waveform (left) and the GW spectrum (right). Left column shows 2D (top) and 3D (bottom) neutrino-driven mechanisms while right column shows 2D (top) and 3D (bottom) magnetohydrodynamic mechanisms. Figure taken from [102].

about 10^{-12} to $10^{-8}\,M_{\odot}c^2$ could be emitted in GWs over a higher frequency range of ground based GW detectors, specifically from 150 to 1100 Hz [102]. The GW signal originates from the inner core (highest density part), therefore a GW signal from a CCSN would allow to determine whether a neutrino-driven convection or magnetorotational explosion is the driving mechanism for the explosion. If the core is rapidly spinning, GWs would also allow to measure the angular momentum of the collapsing core [20]. Furthermore, such detection is likely to be accompanied by a neutrino detection allowing to put constraints on the structure of a NS and the exact time of an explosion [130,132]. For models that assume a neutrino-driven shock wave as the main explosion mechanism, current searches are sensitive up to 5 kpc. For magnetorotationally-driven explosions, the distance increases up to ~ 50 kpc [50]. Such distances indicate that gravitational-wave emission from core-collapse supernovae can be detected within the Milky Way and several other satellite galaxies at best. A galaxy like Milky Way is expected to have 1 or 2 supernova explosions per century making the observation of GWs from CCSN unlikely. Nonetheless there is a chance to detect a signal if an event like SN1987A[6] happens. Third generation ground-based GW detectors would be able to detect even a neutrino-driven SN at ~ 50 kpc.

2.3 Isolated neutron stars

Magnetars – neutron stars with extremely strong magnetic fields reaching up to 10^{11} T, a hundred times stronger than a typical NS magnetic field – have been observed to emit repeating bursts of soft gamma rays (SGRs) [169]. It has been suggested that such emission originates from starquakes, rapid adjustments of a NS crust, that release huge amounts of energy in a fraction of a second. Some of that energy could be emitted by the fundamental ('f') mode that produces GWs. For a neutron star the f-mode is in the range of 1–2 kHz and ~ 0.1 ms duration [23].

One of the strongest known magnetar starquakes was observed on December 27, 2004 [25]. SGR 1806-20 released 1.0×10^{47} erg, and even though it is 14.5 kpc away the blast caused Earth's ionosphere to expand due to incoming gamma rays. The amount of magnetic energy available for SGR is comparable to the energy available for a GRB central engine, and can reach 10^{48}–10^{49} erg [61]. Searches for GWs associated with SGR 1806-20 found no candidates and put upper limits on the GW emission of $h_{rss} = 4.5 \times 10^{-22}\,\mathrm{Hz}^{-1/2}$ ($E_{GW}^{iso,90\%} = 4.29 \times 10^{-8} M_{\odot}c^2$) [25].

Levin and Hoven (2011) estimated that only a small fraction of magnetic field energy is converted into f-modes, therefore the detection of GWs from magnetars is unlikely with the current generation of detectors [107]. However Stropnitzky and Profumo (2014) claim that SGR pulsar glitches from isolated neutron stars 'are promising targets for gravity wave searches by current and next-generation

[6] SN 1987A is a Type II SN that exploded in the Large Magellanic Cloud, 51.4 kpc away.

detectors' [163]. Andersson and Comer (2001) estimate that the gravitational wave amplitude, h, for such events lies between 10^{-23} and 10^{-35} in the frequency range 1–1000 Hz, depending on the model [22]. These results suggest that only galactic SGRs may be detectable with advanced LIGO and Virgo detectors. The most recent search for GWs from 23 known magnetars provided null results with an upper limit of $h_{rss} = 1.1 \times 10^{-22}$ at 150 Hz [18].

2.4 Fast radio bursts

Fast radio bursts (FRBs) are millisecond-duration pulses in radio frequency discovered in 2007 [116]. FRBs resemble individual pulses of galactic pulsars but the instrinsic FRB flux is about a billion times larger. More than a hundred FRBs have been detected [3], yet it is not understood what astrophysical phenomena causes these transients.

Similarly to pulsars, FRB signals are distinctively dispersed by the interstellar medium and intergalactic medium. When an EM wave travels through cold plasma, its travel speed depends on frequency. As a result, the FRB pulse time of arrival is non-uniform across the frequency range (Fig. 2.7). The delay between different frequencies is quantified by the Dispersion Measure DM $= \int_0^d ds\ n_e$, where d is distance to the source and n_e is electron density. The DM allows us to determine the distance to the source if the line-of-sight electron density is known or vice-versa. Comparing the dispersion measure of FRBs with pulsar data, it can be seen that FRBs are likely to be an extragalactic phenomena (Fig. 2.8).

This claim has been supported by the first-ever localised FRB in 2012 found to be 972 Mpc away [104,154]. FRB 121102 emitted 9 bursts over 83 hours of observation, and is the first repeating FRB of only 4 confirmed cases[7]. Observation of repeating and non-repeating FRBs means that there could be multiple populations of FRB progenitors [140] or just that repetition times may vary significantly for different FRBs.

There have been multiple explanations for FRBs, ranging from solar sails of an extragalactic civilization to exploding black holes [96, 113]. Any plausible model needs to explain so far observed properties of FRB: high intrinsic flux, repeatability, and high abundance (30-40 FRBs per day). One of the most promising explanations is young, highly magnetized stars (Fig. 2.9). After a magnetar is formed, magnetized and/or spin-driven wind shocks ionize the left-over ejecta material. The ionized material creates a synchrotron radio emission that corresponds to a fast radio burst. This hypothesis has gained additional support by the very recent observation of FRB 200428 and magnetar SGR 1935+2154 [57]. If FRBs are indeed highly magnetized stars, then we should expect GW emission similar to the one discussed in §2.3. In such case FRBs would be detectable with GWs only within our galaxy.

[7] As of May 2020

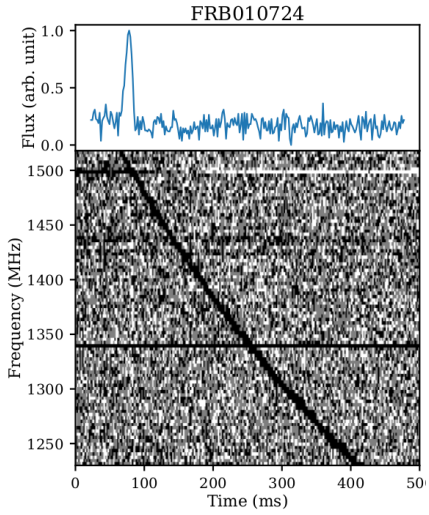

Figure 2.7: The first-reported FRB 010724 has a distinct dispersion with dispersion measure DM = 375 pc cm^{-3}. Top: de-dispersed spectra of FRB 010724. Bottom: original spectra of FRB 010724 showing clear evidence of dispersion as low frequencies arrive later. Figure taken from [59].

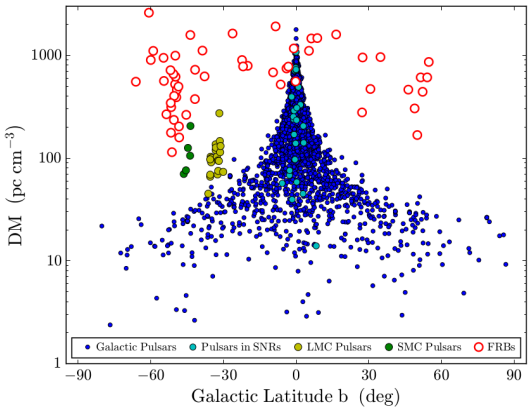

Figure 2.8: Dispersion measure plotted against Galactic latitude for FRBs and pulsars. Overall the FRB dispersion measure is higher on average, ranging from 100 to 2600 pc cm^{-3} versus 3 − 1700pc cm^{-3} for pulsars. Figure taken from [59].

2.5 Unknown gravitational-wave bursts

Every time a new observational tool has been used, a completely unexpected phenomenon was discovered revolutionising our understanding of the Universe. When Galileo pointed a telescope to the sky, he discovered that a band of diffuse light arching the sky consists of individual stars unresolvable by the human eye. It is now known as the Milky Way galaxy. Once Wilson and Penzias turned on Holmdel Horn Antenna in New Jersey, USA, they observed an annoying background hiss which was later identified as a cosmic microwave background. GRBs were detected with satellites originally intended to search for signatures of nuclear weapon tests. These and many other examples suggest that the opened GW window could lead to a detection of unknown phenomena.

There are several educated guesses that we could make about an unknown source. Using Eq. (30) from [165], we can estimate an effective sensitive distance for a brief GW burst around a central frequency f_0

$$\mathcal{R}_{eff} \simeq \left(\frac{G}{2\pi^2} \frac{E_{GW}}{S(f_0) f_0^2 \rho_{det}^2} \right), \tag{2.3}$$

where G is gravitational constant, E_{GW} is energy emitted in GWs, $S(f_0)$ is the one-sided noise power spectrum, and ρ_{det}^2 is match-filtered SNR required for detection.

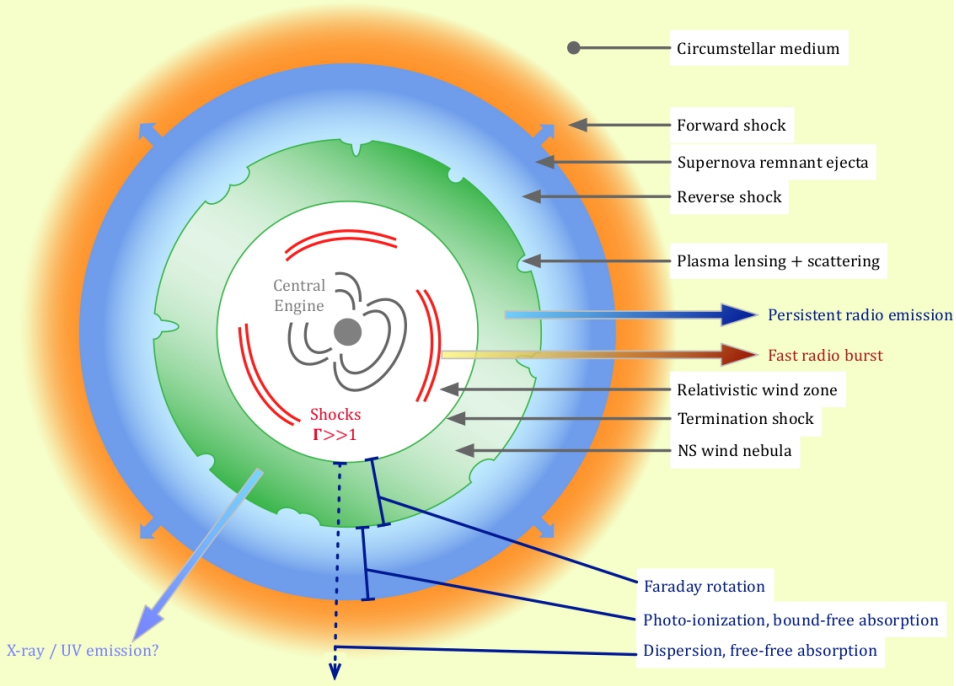

Figure 2.9: One of suggested mechanisms to explain the FRB emission. After a new magnetised star is formed, left-over ejecta material (blue) is ionized by spin-down and/or magetically-driven wind shocks producing a hot nebula (yellow). The ionized material creates a synchrotron radio emission which undergoes dispersion, free-free absorption and Faraday rotation - features that correspond to a FRB. Illustration taken from [59].

For our calculations we assume $\rho_{det} = 8$.

For an unknown GW source that emits GWs at energies that may be typical of a CCSN ($E_{GW,Burst} \approx 10^{-7}\, M_{\odot}c^2$), an effective sensitive detection range $\mathcal{R}_{eff}$ is 35 kpc at 100 Hz for Advanced LIGO. If the source however is highly relativistic like a BBH merger ($E_{GW,BBH} \approx 3\, M_{\odot}c^2$), $\mathcal{R}_{eff}$ would be 190 Mpc at 100 Hz. For future ground-based third generation GW detectors these distances would be higher by a factor of ~ 10 at 100 Hz and ~ 100 at 10 Hz. Figure 2.10 shows how effective sensitive distance $\mathcal{R}_{eff}$ varies over frequency for Advanced LIGO at design sensitivity and for Einstein Telescope.

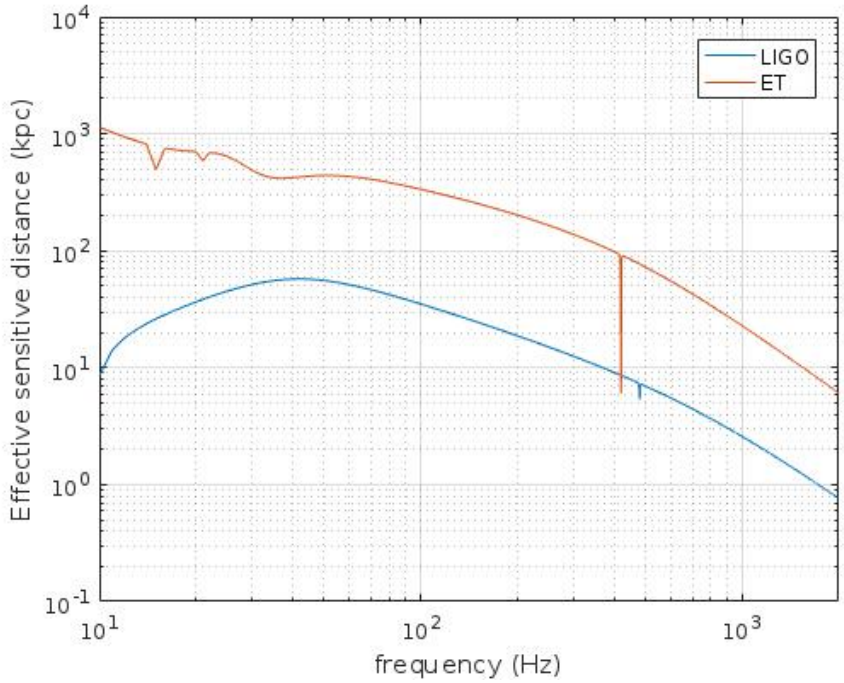

Figure 2.10: Effective sensitive distance $\mathcal{R}_{eff}$ of GW sources assuming $E_{GW,Burst} \approx 10^{-7} M_{\odot}c^2$ and $\rho_{det} = 8$ for Advanced LIGO and Einstein Telescope. GW burst sources are detectable roughly within tens of kpc (Mpc) range with Advanced LIGO (Einstein Telescope).

The EM signature of such signals and the possibility of an EM follow-up is highly uncertain. Some GW sources such as BBH mergers are expected not to emit any EM waves while a BNS merger can produce a GRB and a kilonovae, and are detectable on extragalactic scales [33].

2.6 Physics and astrophysics with gravitational waves

There are many questions unanswered about GW burst sources, e.g. the CCSN explosion mechanism and the nature of FRB progenitors just to name a few. An observation of GW emission related to any of these sources could be a very useful

probe. Here we will briefly review the science already enabled by GW astronomy, as well as what could be learnt from GW bursts.

Speed of gravity. GRB 170817A was observed 1.74 ± 0.05 s later than the GW signal GW170817. Optical observations estimated that the distance to the source was 40 Mpc. Knowing that the time delay between the BNS merger and the launch of the jet would not be more than a few seconds, we can use this information to put a constraint on the speed of gravitational waves. The fractional speed difference between electromagnetic and gravitational waves is $\lesssim 10^{-15}$, about 13 magnitudes lower than any previous measurement [32]. Such a constraint rules out some alternative gravity theories and dark-matter emulator models [43].

Hubble constant. The Hubble constant H_0 measures the expansion of the Universe and follows the simple relation

$$H_0 = \frac{v}{d_L}, \tag{2.4}$$

where v and d_L are velocity and luminosity distance of an object respectively.

For relatively close sources (redshift $z \ll 1$), Eq. (2.4) simplifies to

$$H_0 \approx \frac{cz}{d_L}. \tag{2.5}$$

Currently, CMB measurements from the early universe indicate $H_0 = 67.8 \pm 0.9\,\mathrm{kms^{-1}Mpc^{-1}}$ [147]. Local universe measurements using Type Ia SN give $H_0 = 73.48 \pm 1.66\,\mathrm{kms^{-1}Mpc^{-1}}$, a value that is 3.7σ away from the CMB measurements [7]. It has been argued that this difference is caused by either systematic errors in one (or both) methods or new unknown physics [81].

The coincident EM–GW detection of GW170817 allowed estimation of the Hubble constant H_0 by a completely new and independent method. GW parameter estimation provided a posterior on the luminosity distance to the source while optical observations of the afterglow AT2017-gfo determined the source redshift $z = 0.01$. Using Eq. (2.5) the Hubble constant was found to be $H_0 = 70^{+12}_{-8}\,\mathrm{kms^{-1}Mpc^{-1}}$ which lies in between the CMB and Type Ia SN measurements (Fig. 2.11) [30]. The relatively large error bars on the estimated H_0 value are dominated by the GW distance uncertainty.

However for the majority of GW detections (particularly for BBHs) it is not expected to find EM counterparts. In place of the (unknown) redshift of the source we use the redshifts of galaxies within the 3-dimensional volume estimated to contain the source, the idea proposed by Schutz in 1986 [34, 158]. Future GW observations with EM *and without EM counterparts* may enable us to measure the Hubble constant H_0 with 1% uncertainty over the the next five years [56].

Equation of State. The equation of State (EoS) is a relationship between thermodynamic quantities, for example pressure dependence on density. Determin-

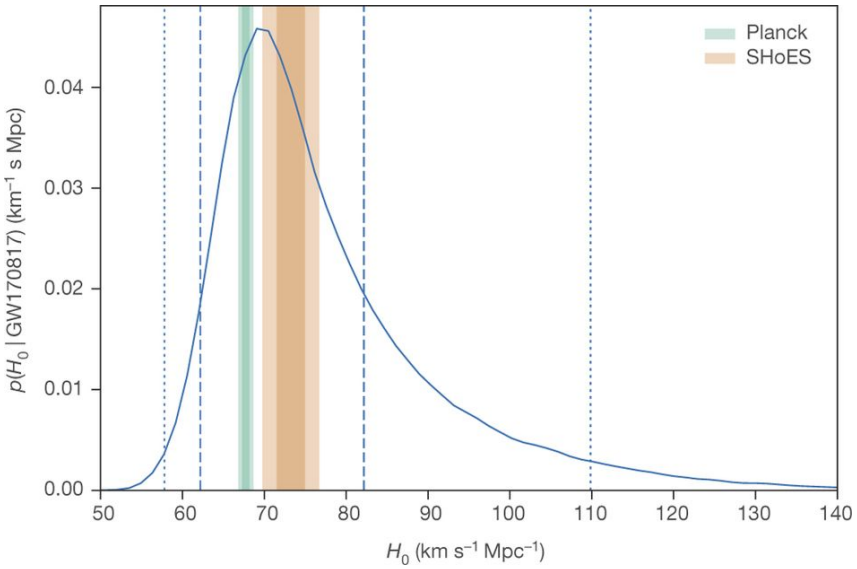

Figure 2.11: Comparison of the Hubble constant H_0 estimate found by CMB measurements (green), Type Ia SN (orange) and GW170817 with its counterpart information (blue). GW observations determine the Hubble constant to be $H_0 = 70^{+12}_{-8}\,\mathrm{kms}^{-1}\mathrm{Mpc}^{-1}$ at 68.3% credible interval. Dashed and dotted vertical lines indicate 1σ (68.3%) and 2σ (95.4%) credible intervals respectively. The relatively large error bars on the GW H_0 measurement are dominated by the GW distance uncertainty. Figure taken from [30].

ing the exact EoS of a NS would allow to estimate the NS composition, radius and mass relationship, and other macroscopic properties such as the tidal deformability and moment of inertia. Understanding the equation of state would also help to investigate other topics related to high temperature and density, e.g. early Big Bang times or hadronic interactions [153]. GW170817 and its counterpart AT2017-gfo observations allowed to constrain the EoS by placing an upper bound on the tidal deformability $\tilde{\Lambda}$, and ruled out some extreme case EoSs (Fig. 2.12).

Other GW sources such as isolated neutron stars could also constrain the EoS. For example, NS oscillations caused by a magnetar flare or a pulsar glitch would allow to identify and characterize NS modes that depend on the EoS [26, 122].

Postface

In this chapter we have reviewed possible GW burst sources and their emission mechanisms. We started by introducing GRBs: the history of GRB observations, the difference between short and long GRBs, their relation to compact binary mergers and CCSNe, and the discovery of GW170817 (§2.1). We also have presented other possible GW burst sources such as core-collapse supernova (§2.2), isolated neutron stars (§2.3), FRBs (§2.4) and unknown GW bursts (§2.5). The chapter ends with examples of the science enabled by GWs and what could be learnt from

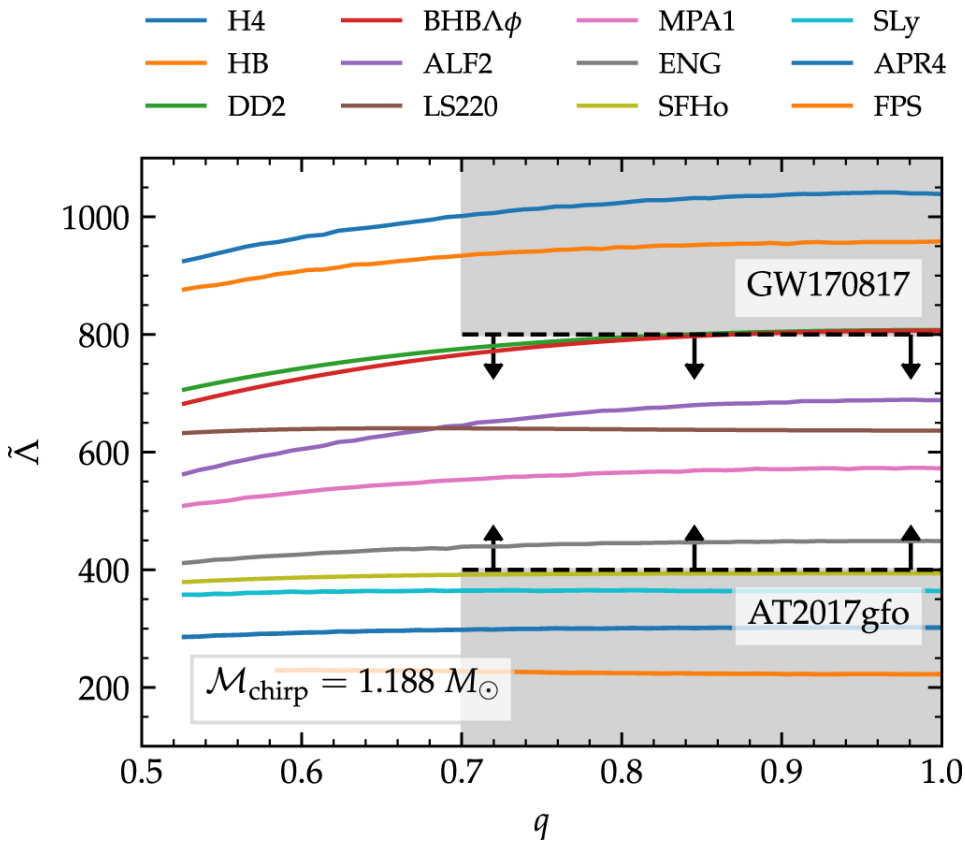

Figure 2.12: The figure illustrates constraints on the tidal deformability parameter $\tilde{\Lambda}$ (Eq. (1) from [149]) from joint GW and EM observations of GW170817. The shaded region is the exclusion region with 90% confidence level estimated by GW observations (above) and EM observations (below). For reference, the value of $\tilde{\Lambda}$ predicted by various candidate EoSs are indicated by colored lines (listed in order from top to bottom). We see that several proposed EoSs are ruled out by these observations. Colored lines indicating the value of tidal deformability $\tilde{\Lambda}$ are a function of the mass ratio q for a fixed chrip mass $\mathcal{M}_{chirp} = 1.88 M_\odot$. Figure taken from [149].

GW bursts (§2.6).

The following questions motivate the content and organization of this thesis:

- How can we detect an unmodelled GW transient?
- How well can we reconstruct GW burst parameters such as sky location and especially the waveform $h(t)$, and robustly distinguish true signals from glitches?
- How can we infer the structure of the GW source from its waveform $h(t)$?

The next chapter (§3) deals with the first question and describes a targeted GRB search as an example of a GW burst search. Chapter 4 describes a study that assessed BayesWave performance in three key areas: signal/glitch discrimination, gravitational waveform $h(t)$ reconstruction and sky localisation accuracy. Finally, Ch. 5 presents a novel method to reconstruct density perturbations $\delta\rho(t, r, \theta, \phi)$ of the source from the GW signal $h(t)$.

Chapter 3

Search for gravitational waves associated with gamma-ray bursts

In the previous chapter we presented possible GW burst sources such as GRBs, FRBs, supernovae and isolated neutron stars. Many of these sources do not have precise GW models due to currently unknown physics and computational limitations, which in turn poses a problem of how to detect such sources with gravitational waves.

In this chapter we will introduce a search for gravitational waves associated with GRBs using X-Pipeline, a software package designed for detecting unmodelled GWs. We will describe how X-Pipeline works, followed by the most recent results from the LIGO–Virgo observing runs 2 and 3a: the detection of GW170817, the search for candidate GWs associated with other GRBs, exclusion distances, and implications for the short GRB rate. The X-Pipeline description is based on the article Sutton et al. (2010) [144] while the O2 and O3a results are based on Abbott et al. (2019) [49] and [74]

3.1 Unmodelled gravitational-wave search with X-Pipeline

Suppose there is a gravitational wave $h_+(t,\vec{x})$, $h_\times(t,\vec{x})$ passing through the Earth from a direction $\hat{\Omega}$. Data from a detector $\alpha \in [1,...,D]$ contains the signal and noise n_α,

$$d_\alpha(t) = F_\alpha^+(\hat{\Omega})h_+(t) + F_\alpha^\times(\hat{\Omega})h_\times(t) + n_\alpha(t), \tag{3.1}$$

where we assume that data streams are time-shifted according to the position of detector α and the incident direction $\hat{\Omega}$ so that the signal is simultaneous in all detectors. $F^+(\hat{\Omega})$ and $F^\times(\hat{\Omega})$ are the antenna response factors previously described in §1.3.2. We also define $h_{+,\times}(t) \equiv h_{+,\times}(t,\vec{r}_0)$, where $\vec{r}_0$ is an arbitrary reference position.

Quantity	Continuous	Discrete
time series	x(t)	x[j]
frequency series	$\tilde{x}(f)$	$f_s^{-1}\tilde{x}[k]$
time integral	$\int dt$	$f_s^{-1}\sum_j$
frequency integral	$\int df$	$f_s N^{-1}\sum_k$
delta function (time)	$\delta(t-t')$	$f_s\delta_{jj'}$
delta function (frequency)	$\delta(f-f')$	$Nf_s^{-1}\delta_{kk'}$

Table 3.1: Variables used in this chapter expressed in continuous and discrete notation.

Data is sampled discretely, therefore we use discrete notation. The Fourier transform $\tilde{x}[k]$ of a time series $x[j]$ is defined as

$$\begin{aligned}\tilde{x}[k] &= \sum_{j=0}^{N-1} x[j]e^{-i2\pi jk/N},\\ x[j] &= \frac{1}{N}\sum_{k=0}^{N-1}\tilde{x}[k]e^{i2\pi jk/N},\end{aligned} \tag{3.2}$$

where N is the number of sample points in the time domain. See Table 3.1 for other terms converted from continuous to discrete notation with sampling rate f_s.

By defining the one-sided noise Power Spectral Density $S_\alpha[k]$ of the noise $\tilde{n}_\alpha$

$$\langle\tilde{n}_\alpha^*[k]\tilde{n}_\beta[k']\rangle = \frac{N}{2}\delta_{\alpha\beta}\delta_{kk'}S_\alpha[k], \tag{3.3}$$

we can further define the noise-spectrum-weighted quantities

$$\tilde{d}_{w\alpha}[k] = \frac{\tilde{d}_\alpha[k]}{\sqrt{\frac{N}{2}S_\alpha[k]}}, \tag{3.4}$$

$$\tilde{n}_{w\alpha}[k] = \frac{\tilde{n}_\alpha[k]}{\sqrt{\frac{N}{2}S_\alpha[k]}}, \tag{3.5}$$

$$F_{w\alpha}^{+,\times}(\hat{\Omega},k) = \frac{F_\alpha^{+,\times}(\hat{\Omega})}{\sqrt{\frac{N}{2}S_\alpha[k]}}, \tag{3.6}$$

with the normalisation of the whitened noise

$$\langle\tilde{n}_{w\alpha}^*[k]\tilde{n}_{w\beta}^*[k']\rangle = \delta_{\alpha\beta}\delta_{kk'}. \tag{3.7}$$

We can now rewrite Eq. (3.1) in matrix notation

$$\tilde{\mathbf{d}} = \mathbf{F}\tilde{\mathbf{h}} + \tilde{\mathbf{n}}, \tag{3.8}$$

where $\tilde{\mathbf{d}}$, $\mathbf{F}$ and $\tilde{\mathbf{n}}$ are noise weighted quantities, and $\tilde{\mathbf{h}}$ is the Fourier transformed gravitational wave $\{h_+(t), h_\times(t)\}$. Note that the whitened noise is uniform over frequency (Eq. (3.7)), therefore the matrix $\tilde{\mathbf{F}}$ (Eq. (3.8)) incorporates all network

sensitivity per frequency and sky position bin.

Maximum likelihood and null energy

Assuming Gaussian noise in a detector α, we can express the probability of recording data $\tilde{\mathbf{d}}$ when a gravitational wave $\tilde{\mathbf{h}}$ passes as

$$P(\tilde{\mathbf{d}}|\tilde{\mathbf{h}}) = \frac{1}{(2\pi)^{D/2}} \exp\left[-\frac{1}{2}\left|\tilde{\mathbf{d}} - \mathbf{F}\tilde{\mathbf{h}}\right|^2 \right], \tag{3.9}$$

where the variance of the Gaussian is unity due to the whitening condition.

For a set $\{\tilde{\mathbf{d}}\}$ of N_p time-frequency pixels,

$$P(\tilde{\mathbf{d}}|\tilde{\mathbf{h}}) = \frac{1}{(2\pi)^{N_p D/2}} \exp\left[-\frac{1}{2}\sum_k \left|\tilde{\mathbf{d}}[k] - \mathbf{F}[k]\tilde{\mathbf{h}}[k]\right|^2 \right], \tag{3.10}$$

where k is the pixel number. Then the likelihood ratio L of hypotheses that (1) the data contains a gravitational-wave signal versus (2) the data contains no gravitational-wave signal is given by

$$L \equiv \ln \frac{P(\{\tilde{\mathbf{d}}\}|\{\tilde{\mathbf{h}}\})}{P(\{\tilde{\mathbf{d}}\}|\{0\})} = \frac{1}{2}\sum_k \left[\left|\tilde{\mathbf{d}}\right|^2 - \left|\tilde{\mathbf{d}} - \mathbf{F}\tilde{\mathbf{h}}\right|^2 \right]. \tag{3.11}$$

In order to solve Eq. (3.11), we need to know $\tilde{\mathbf{h}}$. The most probable value of $\tilde{\mathbf{h}}$ is the one that maximizes the likelihood ratio, i.e.

$$0 = \left.\frac{\partial L}{\partial \tilde{\mathbf{h}}}\right|_{\tilde{\mathbf{h}}=\tilde{\mathbf{h}}_{max}}, \tag{3.12}$$

giving

$$\tilde{\mathbf{h}}_{\mathbf{max}} = (\mathbf{F}^\dagger\mathbf{F})^{-1}\mathbf{F}^\dagger\tilde{\mathbf{d}}, \tag{3.13}$$

where the superscript † denotes the conjugate transpose. We finally derive the maximum likelihood by substituting the solution for $\tilde{\mathbf{h}}_{max}$ into Eq. (3.11)

$$E_{ML} \equiv E_{SL} \equiv 2L(\tilde{\mathbf{h}}_{\mathbf{max}}) = \sum_k \tilde{\mathbf{d}}^\dagger \mathbf{P}^{GW} \tilde{\mathbf{d}}, \tag{3.14}$$

which is the definition of 'standard energy' in X-Pipeline. Maximum likelihood is also defined as standard likelihood in X-Pipeline, i.e. $E_{SL} \equiv E_{ML}$, and we will use both terms interchangeably. Also note that the factor of 2 is purely for convenience. The projection operator operator $\mathbf{P}^{GW}$ in Eq. (3.14) is defined as

$$\mathbf{P}^{GW} \equiv \mathbf{F}(\mathbf{F}^\dagger\mathbf{F})^{-1}\mathbf{F}^\dagger. \tag{3.15}$$

Since we used $\tilde{\mathbf{h}}_{max}$ to find E_{SL}, the standard likelihood is therefore the maximum amount of energy in the data consistent with the hypothesis that the data

contains a GW signal from the direction $\hat{\Omega}$.

The total energy is defined as

$$E_{tot} = \sum_k \left|\tilde{\mathbf{d}}\right|^2, \tag{3.16}$$

which is simply the auto-correlation of data summed over all detectors in the network. We refer to a statistic constructed purely from auto-correlation terms as an 'incoherent' statistic, as opposed to a 'coherent' statistic such as E_{SL}.

Having the total energy E_{tot} and the maximum energy consistent with the data containing a gravitational-wave signal E_{SL}, we can define the null energy

$$E_{null} \equiv E_{tot} - E_{SL} = \sum_k \tilde{\mathbf{d}}^\dagger \mathbf{P}^{null} \tilde{\mathbf{d}}, \tag{3.17}$$

where $\mathbf{P}^{null} = \mathbf{I} - \mathbf{P}^{GW}$. The null energy is the opposite of E_{SL} – it is the *minimum* amount of energy in the data inconsistent with the hypothesis that the data contains a signal, i.e. it is the minimum energy that must be due to noise.

For a coherent search with a known localisation (e.g. GRB triggered X-Pipeline search), the use of the standard likelihood E_{SL} as a detection statistic allows to perform a more sensitive search because the incoherent noise E_{null} is removed from the data stream. This results in ~ 1.3 factor sensitivity improvement compared to the cross-correlation statistic [144]. It is possible to use other projection operators to compute the energy associated with individual GW polarisations, e.g. E_+, $E_\times$, $E_{circular}$, and they are derived in [144, 177].

Incoherent energies and background rejection

We previously argued that the standard likelihood E_{SL} allows to perform a more sensitive search than an incoherent search based on total energy E_{tot} because it removes the noise contribution E_{null}. Coherent searches work well under the assumption that noise is Gaussian and stationary, however we know that this is not the case for GW interferometers. A glitch in a single detector can produce large values of E_{SL}; this in turn increases the false alarm rate. Here we outline a method proposed by Chatterji et al. (2006) [155] to surpress glitches by comparing cross-correlation and auto-correlation terms of E_{null}, a projection of the data $\mathbf{d}$ that contains only noise.

Eq. (3.17) can be rewritten as follows

$$E_{null} = \sum_k \sum_{\alpha,\beta} \tilde{d}^\dagger_\alpha P^{null}_{\alpha\beta} \tilde{d}_\beta, \tag{3.18}$$

where terms with indices $\alpha \neq \beta$ are cross-correlation terms and terms with indices $\alpha = \beta$ are auto-correlation terms.

We do not expect for glitches to be correlated across detectors, therefore in such cases E_{null} is dominated by the auto-correlation components:

$$E_{null} \approx I_{null} \equiv \sum_k \sum_\alpha P^{null}_{\alpha\alpha} \left|\tilde{d}_\alpha\right|^2 \qquad \text{(glitches)}, \tag{3.19}$$

where the incoherent null energy I_{null} is the auto-correlation part of the null energy.

For a GW signal we expect E_{null} to be small by definition, however the incoherent energy (auto-correlation components) consists of the sum of positive-definite terms [1]. As a result, we have the following condition

$$E_{null} \ll I_{null} \qquad \text{(GW)}. \tag{3.20}$$

Eqs. (3.19) and (3.20) allows us to construct a coherent veto test

$$I_{null}/E_{null} > C, \tag{3.21}$$

where C is some constant greater than 1. X-Pipeline is able to automatically select the value of C based on data quality. This makes the coherent veto test a very effective method to remove glitches hence reducing the false alarm rate. Eq. (3.21) describes the simplest example of a test to pass GWs and reject noise glitches. More complicated relations between I_{null} and E_{null} can be used and X-Pipeline has several of those tests built-in, e.g. the α test from Was et al. (2012) [177]. In each case X-Pipeline selects the threshold C by comparing background noise glitches to simulated GWs. Analogous tests can be derived for other coherent likelihoods such as E_+, $E_\times$, etc.

3.2 X-Pipeline workflow

In this section we will describe how X-Pipeline coherently analyses the data using a GRB trigger. Once a GRB notice is received, the sky location and time of the trigger are used as input parameters. Then the user needs to define other search parameters such as

1. a set of detectors;
2. intervals of data to be analysed;
3. a set of coherent energies to compute;
4. other search parameters, e.g. FFT lengths.

At the first step X-Pipeline whitens the data (Eq. (3.4)) which is then time-shifted for each sky position provided by the Gamma-ray Coordinates Network trig-

[1] I_{null} is essentially a weighted sum of SNR^2 in each detector.

ger. After that the data are divided into segments and Fourier-transformed producing time-frequency maps for individual detectors, all in parallel for each sky position. Finally, time-frequency maps from each detector are coherently combined and coherent energies are computed, e.g. the standard likelihood E_{SL} from Eq. (3.14). Figure 3.1a shows the time-frequency map of GW170817 for the Hanford-Livingston-Virgo detector network.

Clustering

To identify potential GW signals, X-Pipeline uses a pixel clustering technique. For a particular statistic, a pre-defined threshold is applied that removes low significance pixels. Figure 3.1b shows the remaining 1% loudest pixels after applying a pre-defined threshold cut for GW170817 standard likelihood E_{SL}. Remaining pixels are grouped into clusters where the user may specify a different connectivity criterion, e.g. next-nearest neighbors [167]. Each cluster is considered as a candidate event, and for each candidate event the corresponding statistics E and I are just the sum of the statistics from individual pixels. Our clustering technique works well for GW signals that have a compact time-frequency representation ('single blobs'). It works less well for signals that have power spread over a large time-frequency, such as inspirals. There are two reasons for this behaviour: (1) extended signals may be returned as several separate low-energy clusters and (2) a signal spread over many pixels has more noise contamination. We discuss these effects more in Chapter 4. Pixel clustering increases sensitivity of a coherent search by ~ 1.2 factor comparing to the cross-correlation statistic [144]. Combining this increase with the one from using the standard likelihood E_{SL} as a detection statistic (§3.1) gives a total improvement in sensitivity of about 1.6 comparing to the cross-correlation statistic.

Pixel clustering is repeated with different parameters because a GW signal is not known a priori. For example, a short FFT length results in a good time resolution but poor frequency resolution, and vice-versa for long FFT lengths. After repeating the analysis with different parameters, X-Pipeline selects clusters that have the largest significance as candidate events. Candidate events are then ranked by their significance and coherent veto tests (§3.1) are performed in order to remove glitches. Furthermore, any candidates that coincide with data quality vetoes are discarded. In the next section we will have a look at how a detection is made when candidate events are ranked by their significance.

Detection procedure

X-Pipeline searches for GWs associated with GRBs within a $[-600, 60]$ s window around the GRB trigger time. This so called *on-source* window is astrophysically motivated to include emission scenarios from the GRB progenitors [44, 133]. Before

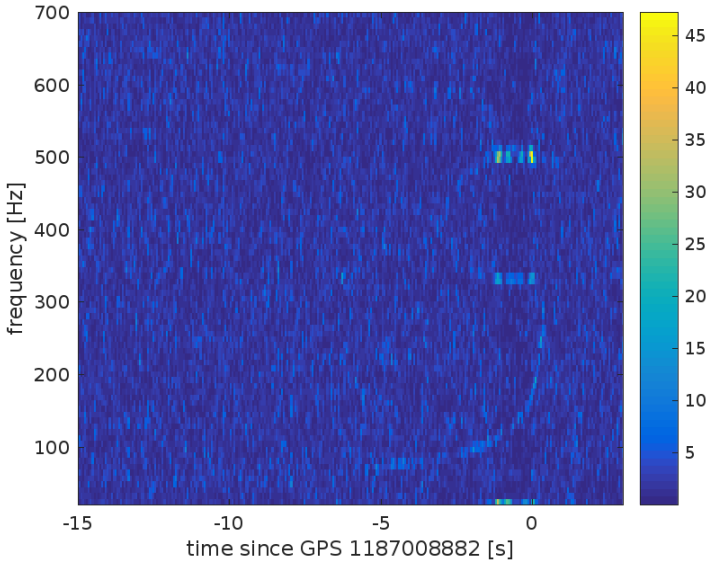

(a)

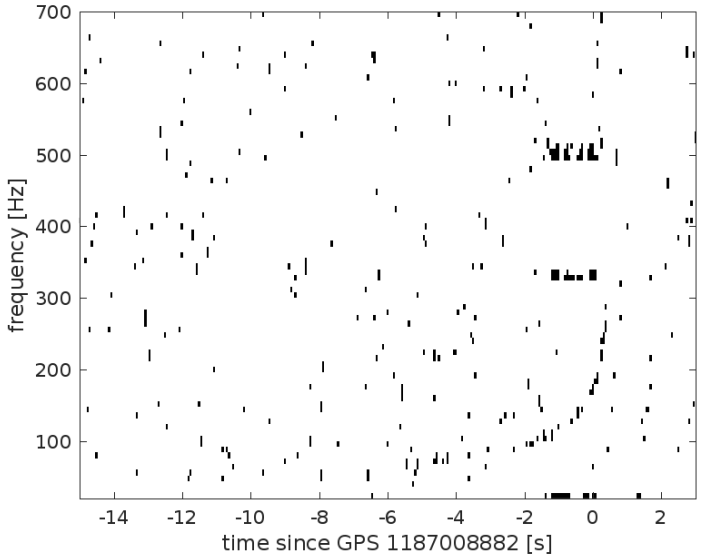

(b)

Figure 3.1: Above: Coherent Livingston-Hanford-Virgo time-frequency map of the standard likelihood E_{SL} for GW170817. Excess power around 330 Hz and 500 Hz is caused by the power leakage from gating a glitch present in the Livingston detector data -1.1 s before T_0, where $T_0 = 1187008882.4$ s. Below: 1% loudest pixels from the plot above. Remaining pixels are clustered together to produce triggers. The chirping GW170817 signal can be clearly seen in both plots.

analysing the on-source window, firstly the *off-source* data is analysed to estimate the background. The off-source window contains data that has no GWs coincident with GRBs, therefore it is entirely made of noise. A typical off-source window is $\pm 1.5\,\mathrm{h}$ around the GRB trigger time, excluding the on-source interval.

To estimate the background the *loudest event* statistic is used. The off-source window is divided into 660 s segments (same duration as the on-source window), and each segment is analysed as previously discussed, i.e. the data are time-shifted, coherently combined, clustered and passed through coherent veto tests. For each segment candidate events that pass the coherent veto tests are recorded as background noise triggers. This allows us to assign a false alarm probability (also known as 'p-value') to each on-source event as the fraction of the loudest off-source events that are louder than the on-source event. It is worth noting that the coherent veto cut thresholds are defined as those that give the lowest average h_{rss} (discussed in the next section) limits at a user-specified FAP – typically 1%.

For a GW detection we require that the most significant on-source candidate event must be louder than any trigger from the off-source window; it also must pass the coherent veto tests. Comparing the loudest on-source window event to the background noise from the off-source window allows to estimate a GW event probability as low as 5%. Time-shifting of data from multiple detectors allows to lower this probability to sub-1% level given that the on-source event is louder than the background. A '5 sigma' GW detection requires FAP $< 1/(3.6 \times 10^6)$.

Upper limits

If there is no statistically significant on-source candidate event, we can put an upper limit on the strength of GWs associated with GRBs. To estimate this limit we use the root-sum-squared amplitude h_{rss}

$$h_{rss} = \sqrt{\int_{-\infty}^{+\infty} dt \big[h_+^2(t) + h_\times^2(t)\big]}. \tag{3.22}$$

For LIGO–Virgo GW–GRB searches, $h_{rss,\,90\%}$ is used which is minimum amplitude for which there is a 90% or greater chance that such a signal, if present in the on-source region, would have produced a cluster with significance larger than the most significant on-source event [144].

In order to find $h_{rss,\,90\%}$, the on-source window analysis is repeated but with an added artificial signal, an *injection*. We typically perform analyses with circular sine-Gaussian (CSG) injections, defined by

$$\begin{bmatrix} h_+(t) \\ h_\times(t) \end{bmatrix} = \frac{1}{r}\sqrt{\frac{E_{GW}}{f_0 Q}\frac{5G}{4\pi^{3/2}}} \begin{bmatrix} (1+\cos^2\iota)\cos(2\pi f_0 t) \\ 2\cos\iota\sin(2\pi f_0 t) \end{bmatrix} \exp\left[-\frac{(2\pi f_0 t)^2}{2Q^2}\right], \tag{3.23}$$

where ι is the rotation axis inclination angle, f_0 is the signal frequency (equal to twice

Waveform Label	M ($M_\odot$)	χ	η	Duration (s)	Frequency (Hz)	E_{GW} ($M_\odot c^2$)
ADI-A	5	0.30	0.050	39	135-166	0.02
ADI-B	10	0.95	0.200	9	110-209	0.22
ADI-C	10	0.95	0.040	236	130-251	0.25
ADI-D	3	0.70	0.035	142	119-173	0.02
ADI-E	8	0.99	0.065	76	111-234	0.17

Table 3.2: ADI waveform parameters. The second and third columns are the mass and the dimensionless spin parameter of the central BH. The fraction of the disk mass that forms clumps is given by η in the fourth column. The remaining columns give waveform duration, frequency band and the energy emitted in GWs [46].

the rotation frequency), and Q is the number of cycles for which the quadrupolar mass moment is large. For our analysis waveforms with $Q = 9$, $E_{GW} = 10^{-2}\, M_\odot c^2$ and signal frequencies $f_0 = [70, 100, 150, 300]$ Hz were generated [46]. These waveforms are based on the expectation that the GRB central engine is a rapidly spinning instability that leads to a rotating quadrupolar mass distribution. Another type of waveform used in the GW–GRB searches is the Accretion Disc Instability (ADI) waveform [173]. These waveforms are motivated by the idea that the central engine of long GRBs must be a stellar-mass BH surrounded by a massive accretion torus. In such an extreme scenario GWs are produced by clumps of matter in the accretion disk where the source of energy is the spindown of the central BH [138]. ADI waveforms have charateristic frequency in the range 110–251 Hz and duration in the range 9–236 s; see Table 3.2 for all model parameters.

Injections are repeated for a range of h_{rss} values until $h_{rss,\,90\%}$ is found. The exclusion distance $D_{90\%}$ can be estimated by re-arranging Eq. (2.3):

$$D_{90\%} = \left(\frac{G}{\pi^2} \frac{E_{GW}}{f_0^2\; h_{rss,90\%}} \right)^{1/2}, \tag{3.24}$$

where each term has its usual meaning. The exclusion distance $D_{90\%}$ is the distance within which 90% of the injected signals are louder than the most significant on-source trigger, i.e. we can exclude with 90% confidence the hypothesis that the GRB was within this distance and produced a GW of the type tested.

3.3 Search results from LIGO–Virgo observing runs 2 and 3a

The second LIGO–Virgo observing run started on November 30, 2016 and ended on August 25, 2017, with Virgo joining the network on August 1, 2017. LIGO detector

sensitivity varied over the run between 65 Mpc and 100 Mpc BNS range[2]. Virgo sensitivity was about 25 Mpc. During the observing run 275 GRBs were reported by the Fermi, Swift and InterPlanetary Network satellites. A subset of 98 GRBs were selected for a coherent search using X-Pipeline because they were observed at times when at least two of the LIGO–Virgo detectors were operating. Analysing 98 out of 275 GRBs is consistent with a LIGO network duty factor of 45% during O2.

The first part of the LIGO–Virgo observing run 3 (O3a) took place from April 1 until October 1, 2019. Over the course of O3a the LIGO Livingston, LIGO Hanford and Virgo interferometers had median 134 Mpc, 113 Mpc and 45 Mpc BNS range sensitivities respectively. Fermi and Swift reported 142 GRBs during O3a and 105 of them were analyzed by X-Pipeline, which again coincides with the network duty factor of at least two detectors to be 82%. While the duty factor of the LIGO detectors slightly improved since O2, the main increase in the coherent network duty factor is due to adding a third detector to the network, Virgo. Indeed, 85 out of 105 GRBs have available Virgo data, and 44 of those GRBs are two-detector GRBs where Virgo is one of the two detectors. Because Virgo was about two (three) times less sensitive than than LIGO Hanford (LIGO Livingston) in O3a, this had consequences for the GRB median exclusion distance, later to be discussed in more detail. See the further breakdown of GRBs analysed in O2 and O3a by their category in Fig. 3.2.

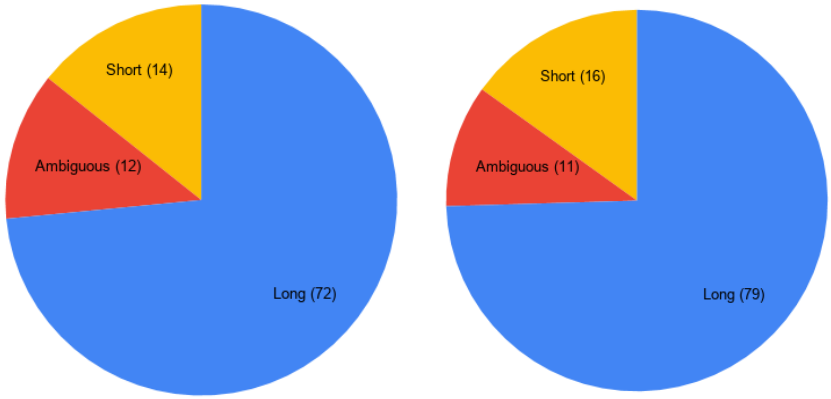

Figure 3.2: Distribution of analysed GRBs in O2 (left) and O3a (right). In our performed searches we assume that all GRBs with $T_{90\%} + \delta T_{90\%} < 2\,\mathrm{s}$ are short, $T_{90\%} + \delta T_{90\%} > 4\,\mathrm{s}$ are long. The remaining GRBs are defined as ambiguous. The total number of analysed GRBs in observing runs 2 and 3a is similar, approximately 100. $T_{90\%}$ is an integrated time when 90% of the total fluence of a GRB lightcurve is observed.

Both the O2 and O3a X-Pipeline GRB analyses were using identical search parameters:

[2]BNS range is a standard figure of merit for detector sensitivity. It is the position- and orientation-averaged distance at which the matched-filtering BNS signal of SNR = 8 is detected.

- On-source window: 660 s
- Off-source window: 10 800 s
- Time-frequency block size: 256 s
- FFT lengths: $[2, 1, \frac{1}{2}, \frac{1}{4}, \frac{1}{8}, \frac{1}{16}, \frac{1}{32}, \frac{1}{64}, \frac{1}{128}]$ s
- Frequency range: $[20, 500]$ Hz
- GRB localisation error box size: 2σ tiling
- Clustering connectivity: 3×3^3 (next-nearest neighbors)

3.3.1 GW170817–GRB 170817A

The BNS coalescence GW170817 was first detected by a low latency pipeline GstLAL, approximately 6 minutes after the signal reached the GW detectors; the corresponding GRB was detected by Fermi and INTEGRAL satellites [33]. It is not surprising that the BNS coalescence was detected by an online all-sky GW search because GW170817 is the strongest GW signal ever recorded with SNR = 32.4 [15]. In order to test how well the event is detected with an unmodelled GW search and to assign a FAP of GW170817 associated with GRB 170817A, we performed the X-Pipeline analysis for this GRB.

All three detectors (LIGO and Virgo) were operating at the time of GRB 170817A, however the LIGO Livingston intereferometer had a glitch just 1.1 s before the BNS merger time (Fig. 2 in [15]). Before performing our analysis the glitch was manually removed by applying a Tukey window, i.e. the glitch was gated out of the data. The analysis of GRB 170817A used Fermi GBM localisation and default X-Pipeline search parameters except for the clustering parameter. A clustering grid of 7×7 was used instead of default 3×3 because we expect long duration signals such as BNS mergers to be spread over more time-frequency pixels than short GW signals. We found that X-Pipeline detected GW170817 with a 4.2σ significance and was by far the loudest event in the O2 and O3a analyses [49, 74]

3.3.2 P-value

Following the procedure outlined in §3.2, X-Pipeline provides an estimate of the p-value for the loudest on-source event per GRB. Figure 3.3 shows the p-value plots for both observing runs, O2 (above) and O3a (below). We can see that for both O2 and O3a analyses the p-values closely follow the no-signal hypothesis (dashed line), and are within the 2σ range (dotted line).

[3] 3×3 clustering is used in the GRB analysis to be more sensitive to short bursts of GWs rather than long duration GW signals. Long duration signals may require bigger clustering grid in order to combine more efficiently pixels that are separated due to noise (see Fig. 3.1b, where 7×7 clustering grid was used for GRB 170817A).

Let us have a look at the most significant events in the O2 and O3a analyses. The more GRBs we analyse, the more we expect for some GRB to have a low p-value just by chance. We can perform a simple back-of-envelope calculation to see how often this happens. The most significant event other than GW170817 during the second observing run had a p-value of 0.0021. We analysed 97 GRBs (excluding GW170817) meaning that in $1 - (1 - 0.0021)^{97} \approx 18\%$ of such analyses we would expect to get a p-value this low or lower. Following this procedure for the O3a sample, we find that $\approx 44\%$ of such analyses we would get a p-value of 0.0055 or lower.

We also perform a weighted binomial test from Aasi et al. (2004) [92] to see if there is a population of weak unresolved GRB–GW events in our sample. To do that, events having the lowest 5% p-values are weighted by interferometer sensitivity at the time of the GRB, and combined using the binomial test. This results in an overall p-value of 0.75 for the O2 and 0.30 for the O3 GRB sets. We can conclude that we found no evidence for a population of weak unresolved GW-GRB events.

3.3.3 Exclusion distance

Given that we found no significant events other than GW170817, we can compute the exclusion distance $D_{90\%}$, previously explained in §3.2. This allows us to constrain the distance of the observed GRB population. Figure 3.4 shows exclusion distance histograms for the O2 and O3a runs for two waveform models, ADI-A and CSG-150 Hz. The median exclusion distance for the ADI-A model was 32 (23) Mpc for O2 (O3a). Similarly, the median exclusion distance for the CSG-150 Hz model was 81 (73) Mpc for O2 (O3a). Table 3.3 provides median 90% confidence level exclusion distances for all CSG and ADI waveforms. Median exclusion distances slightly decreased (with exceptions of CSG-150 Hz and ADI-B) for O3 comparing with O2.

Decreasing exclusion distances in O3a can be explained as follows. Only a minority of the O2 GRBs (13%) were analysed with the Virgo detector while in O3a this number jumped to 71%. Virgo was less sensitive during O3a than any of LIGO detectors at O2 which caused a reduction of the *median* exclusion distances. To prove this point, we estimated the median exclusion distance $D_{90\%}$ for the O3a GRBs analysed with Hanford-Livingston detector network only, see row 'O3a HL' in Table 3.3. It is evident that exclusion distances for the CSG waveforms increased for the O3a run in this case. However, neither O3a nor O3a HL-only exclusion distances are higher than in the O2 run for the ADI waveforms (with an exception of ADI-B). This is related to data quality and the fact that ADI waveforms are much longer than CSGs. To illustrate this point, consider the detection efficiency curves that are used to estimate $D_{90\%}$. If data quality is poor, data will contain more glitches than usual. These glitches can overlap with injected waveforms and cause detection

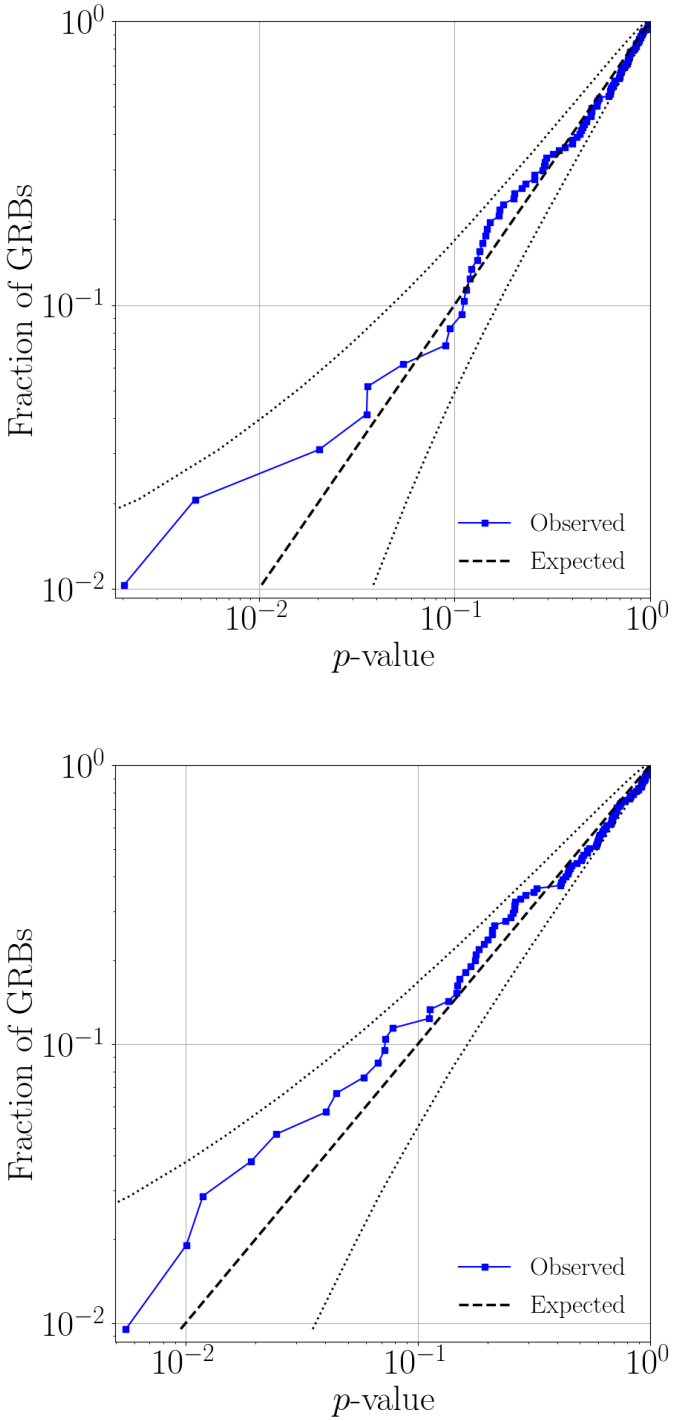

Figure 3.3: Cumulative distribution of p-values for transient GWs associated with GRBs during O2 (above) and O3a (below). In both analyses our results closely follow the null hypothesis (dashed line) and are within the 2σ deviation (dotted line) of the null hypothesis. The combined p-value from the weighted binomial test is 0.75 (0.30) for the O2 (O3a) analysis providing no evidence for a population of weak unresolved GW signals. Note that GW170817 is omitted from the O2 p-value plot.

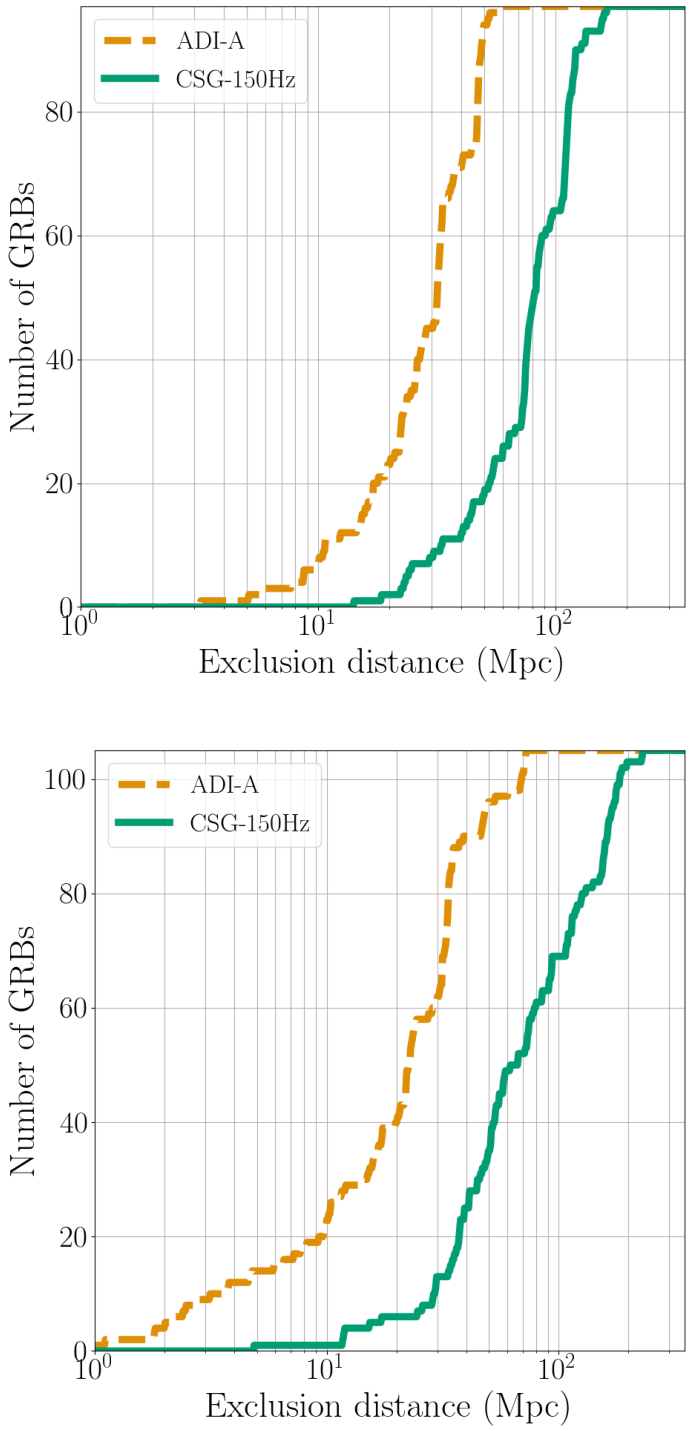

Figure 3.4: Cumulative histograms of the 90% confidence exclusion distances, $D_{90\%}$, for the O2 (above) and O3a GRBs (below) that did not have an identified GW counterpart. For a given GRB and signal model this is the distance within which 90% of simulated signals inserted into off-source data are successfully recovered with a significance greater than the loudest on-source trigger. Median exclusion distances $D_{90\%}$ for the ADI-A waveform model shown in orange are 32 (23) Mpc for O2 (O3a). Median exclusion distances $D_{90\%}$ for the CSG-150 Hz waveforms shown in green are 81 (73) Mpc for O2 (O3a).

Waveform model	CSG 70 Hz	CSG 100 Hz	CSG 150 Hz	CSG 300 Hz
O2 $D_{90\%}$ [Mpc]	112	113	81	38
O3a $D_{90\%}$ [Mpc]	146	104	73	28
O3a HL $D_{90\%}$ [Mpc]	159	125	101	47

Waveform model	ADI A	ADI B	ADI C	ADI D	ADI E
O2 $D_{90\%}$ [Mpc]	32	104	40	15	36
O3a $D_{90\%}$ [Mpc]	23	123	28	11	33
O3a HL $D_{90\%}$ [Mpc]	24	123	24	10	32

Table 3.3: Median 90% confidence level exclusion distance, $D_{90\%}$, for two waveform models, circular sine-Gaussians [46] and accretion disk instabilities [173]. The table shows results from observing runs 2 and 3a where 98 and 105 GRBs were analyzed, respectively. Even though LIGO and Virgo detector sensitivity increased for O3a comparing with the O2 observing run, median exclusion distances $D_{90\%}$ decreased except for the CSG-70 Hz and ADI-B models. The median exclusion distance for the CSG waveforms (except for CSG-70 Hz) decreased because the Virgo detector was used in the O3a analysis more often than in O2 (71% vs 13%) and Virgo was less sensitive in O3a than any of LIGO detectors in O2. Comparison of the O2 exclusion distance $D_{90\%}$ with the O3a exclusion distance $D_{90\%}$ for the GRBs analysed with Hanford and Livingston detectors shows an increase as expected. The increase is not present in ADI waveforms due to poor data quality in O3a. Long waveforms (ADI) have higher chance to overlap a glitch which causes non-monotonic detection efficiency curves leading to poor exclusion distances. The longest ADI waveforms (ADI-C, 236 s duration) are affected more than shorter ADI waveforms (ADI-A, 39 s duration) while the shortest waveforms (ADI-B, 9 s duration) are not affected significantly.

efficiency curves to be non-monotonic (Fig. 3.5). When there are no glitches detection efficiency curves go from 0 to 1 monotonically with increasing amplitude of an injection. If there is a glitch present in the data and it overlaps with an injection, then that injection 'looks' louder than it actually is because it has that extra energy contribution from a glitch. This falsely increases the detection efficiency. In the opposite scenario when there is the same glitch in the data but it does not overlap with an injection (this can happen because injections are performed at random times), the total energy of that injection would be smaller than if a glitch would have overlapped with it. This in turn gives the 'not-glitched' detection efficiency which is smaller than the detection efficiency with a glitch overlapping an injection. Such case would make a dip in detection efficiency curves, e.g. Fig. 3.5. Longer waveforms have a higher chance to overlap with glitches than short waveforms, therefore ADI waveforms are more sensitive to data quality than the CSG waveforms. The duration of the ADI waveforms vary by orders of magnitude, ADI-B being the shortest (9 s duration) and ADI-C being the longest (236 s), see Table 3.2 for reference. As a result, only the ADI-B waveform exclusion distance $D_{90\%}$ increased comparing with O2 while longer waveforms suffered more from glitches and gained no increase in $D_{90\%}$.

Because standard data quality vetoes and coherent tests are applied only after clustering on the time-frequency maps, the most effective way to improve sensitivity for long duration waveforms is to remove glitches before the coherent analysis step. This can be done by gating data around a glitch which 'zeroes' the data, hence removing a portion of the potential signal as well. In the near future it may be possible to remove the glitch and keep the potential signal, which is already possible with wavelet fitting [60], though this is computationally expensive for the use in Burst searches at the moment.

To summarise, median CSG exclusion distances mostly were reduced because more GRBs were analysed with Virgo, and Virgo was less sensitive in O3a than any of LIGO detectors in O2 (although note that adding the Virgo detector allowed to analyse many more GRBs than with a two-detector network, 73% in O3a vs 40% in O2). Median ADI exclusion distances were reduced (except for ADI-B) due to poor data quality which caused injections to overlap with glitches frequently.

We can also see that exclusion distances between individual GRBs vary greatly (Fig. 3.4). All GRBs can be excluded from our galaxy but only a few have exclusion distances greater than 230 Mpc for the CSG-150 Hz model. This mostly depends on the antenna factor for a particular GRB and the detector sensitivity. It is not surprising that we have not detected more GW events except for GW170817 because our distance limits are much lower than the typical distance (where known) of the electromagnetically observed GRB population: roughly 2450 Mpc ($z = 0.44$) and 15 500 Mpc ($z = 1.97$) median distances for short and long GRBs, respectively [5].

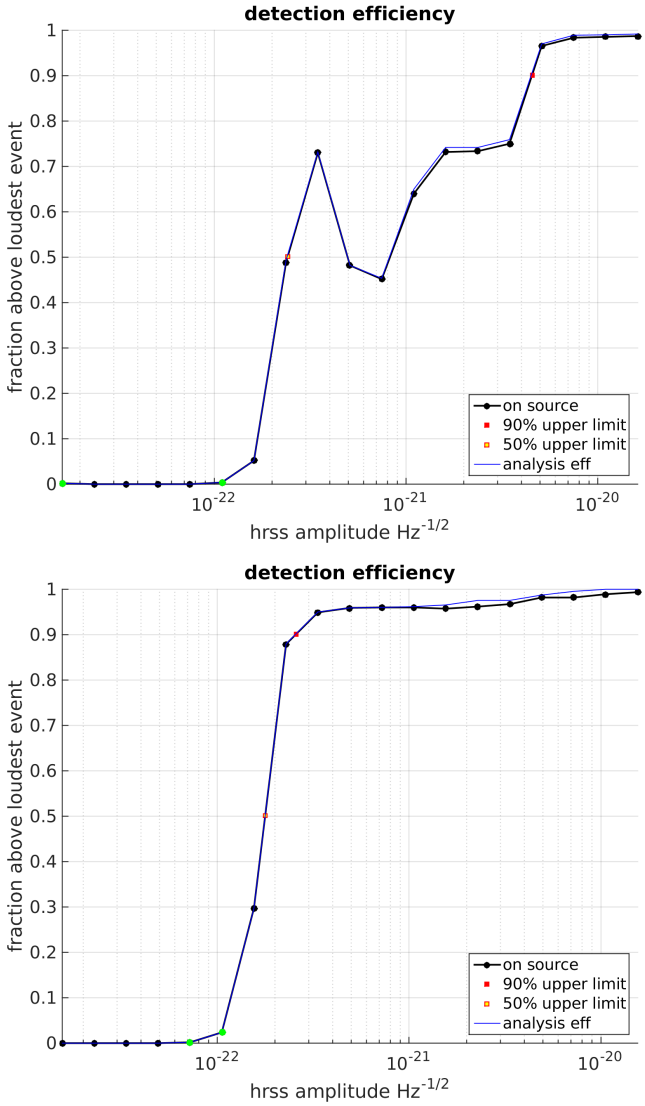

Figure 3.5: Detection efficiency curves for ADI-C (above) and ADI-B (below) for GRB 190620507. Longer waveforms such as ADI-C (236 s duration) have a higher chance to overlap with a glitch than shorter waveforms such as ADI-B (9 s duration). If the data contains many glitches detection efficiency curves become non-monotonic which leads to reduced exclusion distances.

3.3.4 Short GRB population rate

So far we have discussed only the Burst search results. In this section we will demonstrate how the match-filtering search for GWs associated with short GRBs (briefly presented in §2.1.1) allows to constrain the short GRB population rate.

The detection of GW170817–GRB 170817A and the non-detection of any GWs associated with the other 41 short and ambiguous GRBs can be combined to obtain bounds on the short GRB–BNS rate as a function of redshift. This rate depends on parameters that are still uncertain: jet structure, intrinsic GRB luminosity and the observing angle. Here we take a simplistic approach and use an effective luminosity function modelled as a broken power law. We modify the powerlaw by Wanderman & Piran [175] with a second break with a free parameter γ_L to account for a population of very faint GRBs like GRB 170817A. The luminosity function $\phi_o(L_i)$ becomes

$$\phi_o(L_i) = \begin{cases} \left(\frac{L_i}{L_{\star\star}}\right)^{-\gamma_L} \left(\frac{L_{\star\star}}{L_\star}\right)^{-\alpha_L} & L_i < L_{\star\star} \\ \left(\frac{L_i}{L_\star}\right)^{-\alpha_L} & L_{\star\star} < L_i < L_\star \\ \left(\frac{L_i}{L_\star}\right)^{-\beta_L} & L_i > L_\star \end{cases}, \tag{3.25}$$

where L_i is the isotropic equivalent energy. Parameters $L_\star \simeq 2 \times 10^{52}\text{ergs}^{-1}$, $L_{\star\star} \simeq 5 \times 10^{49}\text{ergs}^{-1}$, $\alpha_L \simeq 1$ and $\beta_L \simeq 2$ were found to be the best fit to the observed short GRB redshift distribution [32]. The final observed redshift distribution is normalized by a total Fermi-GBM detection rate of 40 short GRBs per year.

The value of γ_L is constrained using Monte Carlo sampling to agree with current observations: the redshift distribution of observed short GRBs and the O2 GRB analysis results (41 non-detections and a single detection). This yields a posterior of γ_L with 90% confidence bounds of $[0.04, 0.98]$ shown as magenta in Fig. 3.6. Our posterior bounds agree with other observations. The green line shows the observed Fermi short GRB rate calculated in Howell et al. (2019) [87] assuming that all short GRBs are associated with BNS mergers. The sample of observed short GRB redshifts without GW170817 is shown in brown [32]. We also show the BNS merger rate determined from GW observations of $1210^{+3230}_{-1040}\,\text{Gpc}^{-3}\text{yr}^{-1}$ as a reference in black [19]. We can conclude that our model further confirms the hypothesis that at least some short GRB progenitors are BNS mergers. More observations (especially *detections*) would allow to better constrain the powerlaw breaking index γ_L and ultimately GRB properties such as the jet structure, intrinsic GRB luminosity and the fraction of short GRBs caused by the BNS mergers. For the design sensitivity LIGO–Virgo network we expect to see 4–97 BNS mergers per year, while the joint short GRB-BNS rate should be in 0.15–3.90 range per year at 90% confidence. These expectations agree with Mogushi et al. (2019) where they model the short GRB rate

by including the jet geometry [129]. Their estimated short GRB-BNS rate is 0.3–1.8 per year for the design sensitivity LIGO–Virgo network.

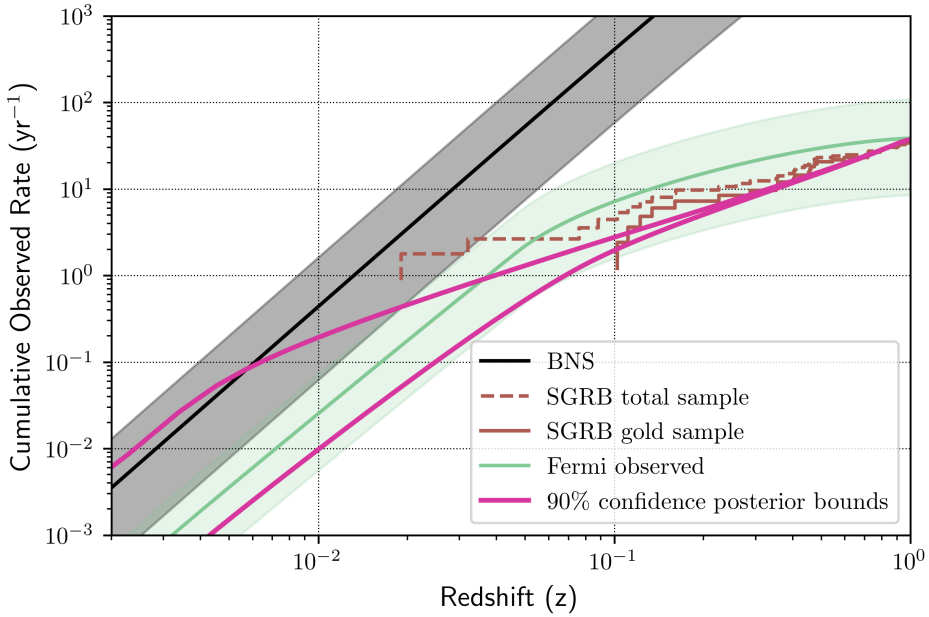

Figure 3.6: Predicted event rates per year as a function of redshift. We provide 90% confidence posterior bounds on a second break index γ_L in the effective luminosity function, Eq. (3.25). The observed short GRB rate by Fermi-GBM is given in green [87] while the measured short GRB distribution without GRB 170817A is shown in brown [32]. The short GRB gold sample refers to GRBs that have more confident localisation than GRBs in the total short GRB sample. As a reference, the BNS merger rate $1210^{+3230}_{-1040}\mathrm{Gpc}^{-3}\,\mathrm{yr}^{-1}$ [19] is given in black. Our results are consistent with the hypothesis that the BNS mergers are short GRB progenitors.

Postface

In this chapter we described how a coherent excess power method, specifically X-Pipeline, can be used for unmodelled GW searches. We also derived some of the coherent energy statistics used in the search such as the standard likelihood E_{SL} and null energy E_{null}, and showed how these statistics can be used for glitch rejection. We presented the results of the unmodelled search for GWs associated with GRBs during the LIGO–Virgo observing runs 2 and 3a, in total 203 GRBs. We found one confident detection, GW170817–GRB 170817A, with a 4.2σ significance. Our population analysis of the other 202 GRBs shows no evidence for weak unresolved GWs, hence we provide exclusion distances $D_{90\%}$ for those GRBs. Finally, using the O2 observations (41 non-detections and 1 detection) we were able to provide a prediction of the future short GRB–GW observation rates. As GW interferometers get better, we expect to see more GWs associated with GRBs; projected rates are 0.15–3.90 such detections per year at design LIGO–Virgo sensitivity.

In the next chapter we will look at the unmodelled GW signal reconstruction – this is the next step after an unknown signal is detected. Specifically, we will investigate BayesWave in three key areas: gravitational waveform reconstruction, sky localisation and signal/glitch discrimination.

Chapter 4

Bayesian inference analysis of gravitational-wave bursts

In the previous chapter we presented X-Pipeline, a coherent search analysis used for searches of GWs associated with GRBs, as well as the search results from LIGO–Virgo observing runs 2 and 3a. We showed that it is possible to detect GWs without relying on precise models, therefore proving that the coherent excess power method is able to detect unmodelled GWs.

In this chapter we will discuss how well a waveform can be reconstructed, among other parameters such as sky localisation and signal/glitch discrimination, without having an astrophysical model. Even more, our study compares Bayesian inference analysis not only with the injected signal parameters but also with theoretical back of envelope estimates. This allows to assess whether the tested pipeline (BayesWave) performs optimally or there is room for improvement. The chapter is based on Pannarale, Macas and Sutton (2018) [142].

4.1 Introduction

The interpretation of signals detected so far (§1.3.5) relied upon precise signal models ('templates'). Yet there are many possible emission mechanisms beyond ordinary coalescences for which the GW radiation cannot be modelled due to unknown physics (e.g. NS equation of state) and/or computational limitations. We presented examples of such sources in Ch. 2, where we discussed generic GW transient emission from GRBS, supernovae, long GRBs, isolated NSs and FRBs. The inability to use matched filtering for GW bursts has spurred the development of tools for the detection and characterisation of GWs that are not model dependent. Among them is BayesWave [60], a Bayesian parameter estimation algorithm for the reconstruction of generic GW transients. Instead of relying on a precise signal model, BayesWave fits linear combinations of basis functions to the data in a manner consistent with either a GW, background noise or glitches. Given a GW candidate provided by a

search pipeline, BayesWave performs a Bayesian analysis under both the signal and the glitch hypotheses, reconstructs the gravitational waveform, and provides estimates of signal parameters, such as the signal duration, bandwith, and sky location. BayesWave has analyzed triggers from low-latency pipelines such as coherent Wave Burst [100, 101], gstLAL [53, 124, 148], or pyCBC [135, 136, 171] including accepted GW events such as GW150914 [13] and GW170817 [16].

We have performed a study to validate BayesWave and assess its performance against first-principle estimates. While there have been some studies of the performance of such algorithms for various kinds of burst signals (see for example [10, 24, 71, 99]), very little has been done to compare their performance to first-principle expectations; i.e. we do not know if presently available tools are performing close to optimally, or if there is significant room for improvement. We address this by assessing BayesWave in three critical areas:

1. *Sky localisation:* How accurately can BayesWave determine the direction to the GW source, compared to ideal matched-filtering algorithms?

2. *Signal–glitch discrimination:* How robustly can BayesWave distinguish true GW signals from non-Gaussian background noise artifacts?

3. *Waveform reconstruction:* How does the accuracy of BayesWave's reconstructed gravitational waveforms compare to first-principles estimates of the possible accuracy of unmodelled reconstructions?

We answer these questions by applying BayesWave to a set of simulated BBH signals added to simulated Advanced LIGO and Advanced Virgo data [86]. While accurate templates are available for BBH signals, BayesWave does not use this information. Using BBH templated signals for our tests allows us to compare the performance of BayesWave to the case of ideal matched-filtering, which does rely on a precise signal model. Despite BayesWave not using a signal model, we find that its performance is remarkably close to optimal in many cases, and we note the conditions under which performance is less than optimal.

4.2 BayesWave

BayesWave is a Bayesian follow-up pipeline for GW triggers. It is designed to distinguish GW signals from non-stationary, non-Gaussian noise transients (i.e. glitches) in interferometric GW detector data, and to characterize the signals themselves [60, 114]. BayesWave uses a multi-component, parametric noise model of variable dimension that accounts for instrument glitches. These are modelled using a linear combination of Morlet-Gabor continuous wavelets. A trans-dimensional reversible jump Markov chain Monte Carlo algorithm allows for the number of wavelets to vary and to explore the parameters of each wavelet. A linear combination of wavelets

constituting a glitch model is built for each individual detector. GW transients of astrophysical origin are (independently) modelled with the same technique: a single GW signal model is built at the center of the Earth and projected onto each detector in the network, taking into account the response of the instrument and the source sky-location, which feeds two parameters (i.e. right ascension and declination) into the reconstruction effort. This procedure enforces the requirement for a signal to be *coherent* across detectors, whereas glitches are reconstructed *independently* for each detector.

The BayesWave algorithm compares the following hypotheses: (1) the data contain only Gaussian noise, (2) the data contain Gaussian noise and glitches, and (3) the data contain Gaussian noise and a GW signal. The comparison is performed in terms of the marginalized posterior (evidence) for each hypothesis.

GW170817 showed that there is a need for additional hypothesis, (4) the data contain Gaussian noise, a GW signal and a glitch. The BNS merger GW170817 signal from Livingston data was contaminated by a glitch just 1.1 s before the coalescence time (see Fig. 2 in [15]). For some analyses the glitch was removed by applying a window function to zero out the data around the glitch while in other cases the glitch was modelled and removed by BayesWave assuming hypothesis no. 4. Our study did not test this hypothesis.

When testing the signal hypothesis (3), BayesWave provides a waveform reconstruction, and posterior distributions for the source sky location parameters and signal characteristics, such as duration, bandwidth, energy, and central frequency. These may be used to compare the data to theoretical models and to assess the performance of the pipeline. Note that the time of the candidate is the only information about the original GW trigger that BayesWave uses.

BayesWave has been used in a number of studies so far. The first BBH detection GW150914 was localized by BayesWave in a 101 sq.deg. region with 50% confidence and a FAR of 1 in 67400 years [45]. Further, Abbott et al. (2016) [13] tested the ability of BayesWave in recovering simulated BBH signals for sources similar to GW150914. The match between the reconstructed and injected waveforms was found to vary between 90% and 95% for systems with total mass between $\sim 60\,M_{\odot}$ and $\sim 100\,M_{\odot}$, and an injected network SNR of 20. The sensitivity range, which is tightly correlated to the total mass and the effective spin of the system, was found to be in the 400–800 Mpc interval. In general, the combined coherent Wave Burst–BayesWave data analysis pipeline was shown to allow for detections across a range of waveform morphologies [95, 115], with confidence increasing with the waveform complexity (at a fixed SNR). This is the case because glitches can be confused more easily with simple, short GW transients, than with complex waveforms in coherent data. Finally, a recent study [24] shows that the two-detector Advanced LIGO network will be able to achieve an 85% and 95% match for BBH signals with network SNR below ~ 20 and ~ 50, respectively. In the same study, the median searched area

and the median angular offset for BBH sources with total mass between $30\,M_\odot$ and $50\,M_\odot$ were found to be 99.2 square degrees and 25.1 square degrees, respectively.

Comparing with these studies our investigation approaches BayesWave testing from a different perspective. Rather than performing only an injection study we also compare results to first principles, for example we compare BayesWave reconstructed GW signal waveform with the expected match from back of envelope calculations. This allows to pinpoint discrepancies between the expected and reconstructed parameters which is crucial not only for using the pipeline but also for further development.

4.3 Analysis setup

The source population we choose for our study consists of non-spinning merging BBHs. Specifically, we use the so-called IMRPhenomB approximant [21]. The values of the individual BH masses that we select are $5\,M_\odot$, $10\,M_\odot$, $50\,M_\odot$, and $100\,M_\odot$. We consider all 10 possible mass combinations: $(5,5)\,M_\odot$, $(5,10)\,M_\odot$, $(5,50)\,M_\odot$, $(5,100)\,M_\odot$, $(10,10)\,M_\odot$, $(10,50)\,M_\odot$, $(10,100)\,M_\odot$, $(50,50)\,M_\odot$, $(50,100)\,M_\odot$, and $(100,100)\,M_\odot$. This population is convenient for a number of reasons.

1. The majority of GW signals detected by LIGO and Virgo to date were emitted by BBH sources [19] , and BBH mergers are expected to dominate the population of GW that we detect with second-generation instruments [66]. The BH masses of the sources detected so far (both the binary constituents and the merger remnants) are all encompassed by our choice of parameter space.

2. Accurate and computationally tractable waveform models exist for these signals, allowing us to compare the BayesWave performance to that of optimal (template-based) algorithms as reported in the literature.

3. BayesWave may be able to resolve aspects of the waveform that are not included in current templated analyses, such as precessing spins or eccentricity. As we shall see, the performance of BayesWave is determined primarily by the time-frequency volume and SNR of the detected signal; we expect other characteristics such as the spin to have little effect. Ultimately it will be useful to characterise BayesWave for the entire family of BBH signals: in this sense, our non-spinning study is a first step in this direction.

4. The SNR of signals from high-mass systems is concentrated in a small time-frequency volume, while the SNR of signals from low-mass systems is spread over a much larger time-frequency volume. This allows us to probe the performance of BayesWave relative to templated algorithms as a function of the signal time-frequency volume, which along with the SNR is the key characteristic of a signal for burst detection algorithms [165].

For each of the 10 mass pairs we generate 20 signals, for a total of 200 simulations, with random sky position, inclination, and polarisation angle. The distances are selected randomly such that the coherent network SNR is in the range 10–35; i.e. we use realistic amplitudes for detectable signals. For this SNR range 20 signals per mass pair are enough to test the performance of BayesWave. The signals are added to simulated data for the LIGO–Virgo network H1-L1-V1, which consists of Gaussian noise following the power spectral density model of [86]. Figure 4.1 shows the noise and signal spectra as a function of frequency.

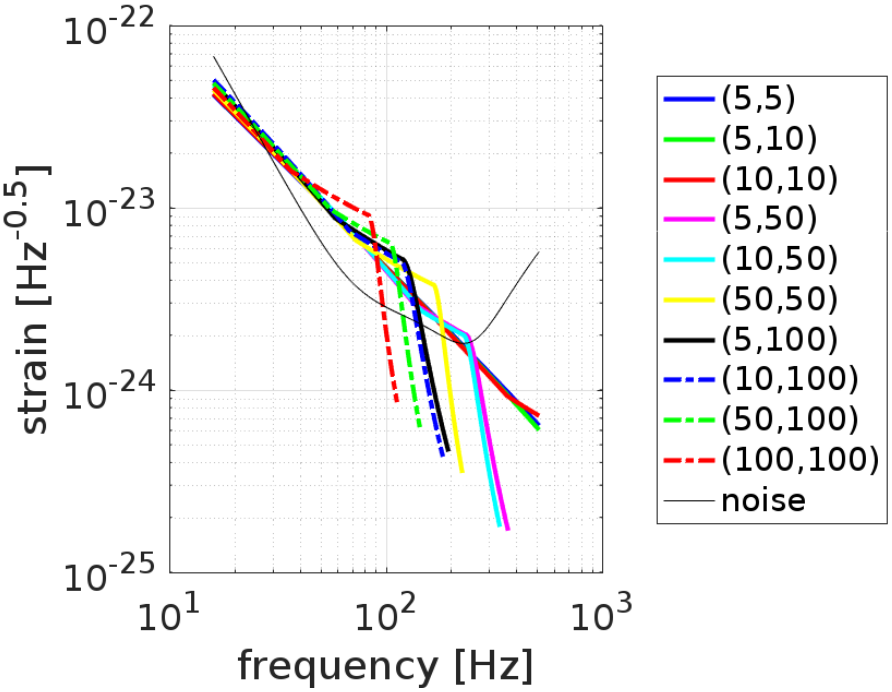

Figure 4.1: Strain spectra for each of the signals tested, compared to the amplitude spectral density of the simulated noise data. As the BHs inspiral, the frequency increases until the two bodies merge and the GW emission cuts off. The merger frequency scales inversely with system mass, so signals from low-mass systems span the full LIGO sensitive band and therefore have large effective bandwidth and time-frequency volume. For high-mass systems the effective bandwidth is much smaller and the signal is concentrated in a relatively small time-frequency volume. These will have implications for localisation accuracy and waveform reconstruction, as discussed in the text.

For each simulation we analyse 4 s of data centred on the binary coalescence time, generated at a sampling rate of 1024 Hz. For comparison, all signals reconstructed by BayesWave in this study were shorter than 1 s. This data is fed into BayesWave for analysis. BayesWave reports the log evidence for the signal vs. glitch and signal vs. noise hypotheses, a sky map, reconstructed time-domain waveforms, spectrograms, and estimates of other properties such as duration, bandwidth, and the SNR recovered in each detector. In the following subsections we focus on BayesWave's

performance on spectrograms, signal vs. glitch discrimination, and the accuracy of sky localisation and waveform reconstruction.

4.4 Results

4.4.1 Time-frequency signal content

As shown in [115], the number of wavelets used by BayesWave to reconstruct a GW signal increases approximately linearly with SNR, at a rate that depends on the signal morphology (higher for more complex waveforms). This is consistent with the behaviour seen in our simulations. For the SNRs considered in our study, the average reconstructed SNR per wavelet is typically 5–10.

For inspiralling BBH signals, the frequency increases until the two bodies merge and the gravitational-wave emission cuts off, as the remnant BH rings down. The merger frequency scales inversely with system mass: low-mass systems produce GW signals that have larger effective bandwidth and time-frequency volume than high-mass systems. Furthermore, the rate of frequency increase in the signal ("chirping") increases with the system mass, so that high-mass systems have a much shorter duration in the detector sensitive band. Together these have an important consequence for burst algorithms such as BayesWave that rely on time-frequency decompositions: signals from low-mass systems are spread over a larger time-frequency area than signals from high-mass systems. Figure 4.2 shows example spectrograms of the simulated and recovered signals for the lowest- and highest-mass systems tested. The low-mass, $(5, 5)\,M_{\odot}$, simulated signal shown on the top left panel occupies a time-frequency area greater than the high-mass, $(100, 100)\,M_{\odot}$, simulated signal shown in the bottom left panel. As a result, BayesWave is able to recover all of the SNR of the high-mass signal (bottom right panel), but not all of the SNR of the low-mass signal (top right panel). Figure 4.3 confirms that the SNR is spread across a larger number of pixels as the system mass decreases. Generally, diluting a given total SNR among a larger number of pixels makes it more difficult for BayesWave to reconstruct the low-SNR portions of the signal, see Figure 4.4. This typically results in a lower reconstructed SNR, duration, and bandwidth for low-mass signals, which in turn lowers the accuracy of the sky localisation, signal classification and waveform reconstruction.

4.4.2 Sky localisation

There are numerous empirical studies of the sky localisation capabilities of existing GW transient detection algorithms, particularly in the context of second-generation GW detector networks (see e.g. [10,24,71,99]). The theoretical basis for sky localisation accuracy is best established for matched-filter searches for binary coalescences. As shown by Fairhurst [75–78], the localisation is based primarily on triangulation

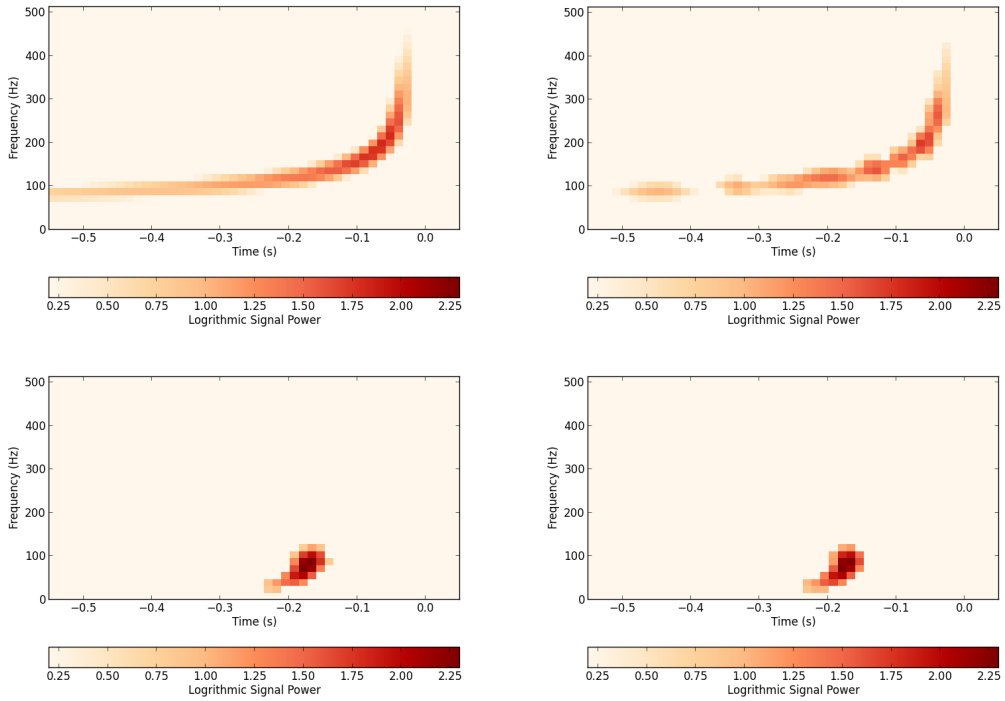

Figure 4.2: Whitened spectrograms for simulated and recovered signals. Top: (5,5) $M_\odot$ simulated (left) and recovered (right) signal. The SNR per time-frequency pixel is lowest at early times and low frequencies; BayesWave only recovers fragments of this portion of the signal. Bottom: (100,100) $M_\odot$ simulated (left) and recovered (right) signal. The SNR is concentrated into a small number of time-frequency pixels which are easily recovered by BayesWave.

via the time-of-arrival differences between the detector sites. The one-sigma measurement uncertainty in the time of arrival is given by

$$\sigma = \frac{1}{2\pi\rho\,\sigma_f}\,, \tag{4.1}$$

where ρ is the matched-filter SNR in the detector and σ_f is the effective bandwidth of the signal; see [76] for definitions. Ignoring the phase and amplitude measured in each detector, Fairhurst shows that one can construct a localisation matrix that defines the contours of fixed probability,

$$\mathbf{M} = \frac{1}{\sum_k \sigma_k^{-2}} \sum_{i,j} \frac{(\mathbf{d}_i - \mathbf{d}_j)(\mathbf{d}_i - \mathbf{d}_j)^T}{2\sigma_i^2\sigma_j^2}\,, \tag{4.2}$$

where $\mathbf{d}_i$ is the position vector of detector i and σ_i is the timing uncertainty in that detector.

The expected sky localisation accuracy with containment probability p is given by

$$A(p, \mathbf{r}) = 2\pi\alpha_1\alpha_2[-\log(1-p)]\,, \tag{4.3}$$

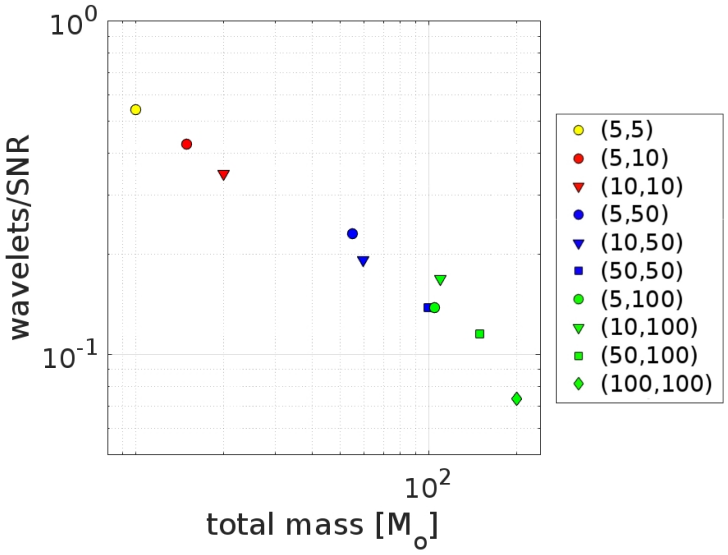

Figure 4.3: Mean number of wavelets per unit injected network SNR vs. system total mass. As the system mass increases, the signal SNR in concentrated into a smaller time-frequency volume, and can be reconstructed with fewer wavelets.

where α_1, α_2 are the inverse square roots of the eigenvalues of the matrix $\mathbf{M}$ after it has been projected onto the sky in the direction $\mathbf{r}$,

$$\mathbf{M}(\mathbf{r}) = \mathbf{P}(\mathbf{r})\,\mathbf{M}\,\mathbf{P}(\mathbf{r})\,, \quad \mathbf{P}(\mathbf{r}) = \mathbf{I} - \mathbf{r}\mathbf{r}^T\,, \tag{4.4}$$

where $\mathbf{I}$ is the identity matrix. Since the approximation (4.3) ignores the phase and amplitude information, it can be considered as a worst-case estimate of the localisation capability.

As shown in [84] and [78], requiring a consistent signal phase and polarisation between the detectors improves the localisation accuracy by an amount which can be approximated by using a timing uncertainty of

$$\sigma_t^c = \frac{1}{2\pi\rho\,\sigma_f}\left(\frac{\sigma_f^2}{\overline{f^2}}\right)^{1/4}\,, \tag{4.5}$$

where $\overline{f^2}$ is the second frequency moment of the signal.

Since $\overline{f^2} > \sigma_f^2$, Eq. (4.5) will yield smaller localisation areas. In their study of binary inspiral signals of total mass up to $20\,M_\odot$, Grover et al. demonstrated that this phase and polarisation correction reduces the predicted localisation areas by a factor of 2–3 relative to timing alone. Finally, Grover et al. also demonstrated that a full Bayesian analysis using signal templates achieves sky localisation accuracies that are still better by a median factor of 1.6; we take this Bayesian analysis to represent the "best possible" performance in the case where the signal waveform is known. [38] found a similar result for BNS sources, with a median factor of ~ 1.3 for the 50% localisation area.

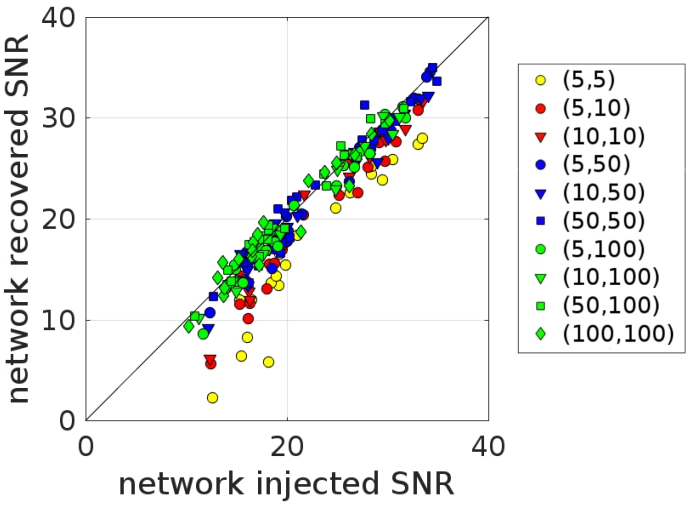

Figure 4.4: Recovered network SNR vs. injected network SNR. BayesWave is able to recover the full SNR of high-mass systems, which occupy a small time-frequency volume. It systematically underestimates the SNR of low-mass systems, which occupy a larger time-frequency volume at a given SNR.

Table 4.1 and Figs. 4.5 and 4.6 compare the 50% and 90% localisation areas reported by BayesWave to the predictions of timing-only ("incoherent") and phase- and polarisation-corrected ("coherent") triangulation. BayesWave typically outperforms the predictions of incoherent (timing-only) triangulation in almost all cases, and outperforms the predictions of coherent (phase- and polarisation-corrected) triangulation for systems of total mass above $50\,M_\odot$. For comparison, the "best possible" templated Bayesian analysis reported in Grover et al. [84] gives 50% localisations that are typically ∼0.6-0.7 of those of coherent triangulation; we see that BayesWave performs comparably for system masses around $100\,M_\odot$ or more.

We conclude that BayesWave is able to localise a gravitational-wave source on the sky as well as a templated analysis despite not using signal templates, provided the signal SNR is concentrated in a sufficiently small time-frequency volume ($\lesssim 10$ wavelets). Furthermore BayesWave still performs reasonably well — within a factor of 2 in area — for higher time-frequency volume signals even for large containment regions.

4.4.3 Signal classification

The confident detection of unmodelled transients depends on the ability to distinguish robustly true signals from the transient noise fluctuations ("glitches") that are common features of the detector noise backgrounds [11]. Searches for generic GW transients typically rely on comparisons of weighted measures of the cross-correlation between detectors to the total energy in the data for signal-glitch discrimination (see, e.g., [13, 100, 144, 155]). BayesWave does this by calculating the log Bayes factors

		Median BayesWave triangulation ratio			
		50% area		90% area	
m_1 $[M_\odot]$	m_2 $[M_\odot]$	incoherent	coherent	incoherent	coherent
5	5	0.7	1.2	0.9	1.6
5	10	0.6	1.1	1.1	2.1
10	10	0.5	1.1	0.7	1.3
5	50	0.4	0.9	0.5	1.0
10	50	0.4	0.8	0.4	0.8
50	50	0.3	0.8	0.3	0.8
5	100	0.2	0.6	0.3	0.7
10	100	0.3	0.7	0.3	0.7
50	100	0.2	0.6	0.2	0.7
100	100	0.1	0.5	0.2	0.8

Table 4.1: Median ratio of 50% and 90% sky localisation areas reported by BayesWave to those predicted by triangulation. BayesWave typically outperforms the predictions of incoherent (timing-only) triangulation in almost all cases, and outperforms the predictions of coherent (phase- and polarisation-corrected) triangulation for systems of total mass above $50\,\mathrm{M}_\odot$. For comparison, [84] report that the 50% localisations from an optimal templated Bayesian analysis are typically ∼0.6-0.7 of those of coherent triangulation [see also [38]]; we see that BayesWave performs comparably for system masses around 100 $\mathrm{M}_\odot$ or more.

for the signal and glitch hypotheses[1]. Under each hypothesis, the transient (either the result of the two GW polarizations, or the glitch time-series in each detector) is fit by a linear combination of Morlet-Gabor wavelets. The Bayes factor depends on both the quality of the fit and the priors; generally, signals which have high SNR-per-pixel throughout a large time-frequency volume are most easily distinguished from glitches. Littenberg et al. [115] argue that the signal-vs.-glitch log Bayes factor

[1]The oLIB pipeline [117] performs a similar analysis, but restricted to a single wavelet. For Bayesian signal-glitch discrimination that relies on the compact binary coalescences model, see e.g. [90, 174].

$\log \mathcal{B}_{\mathcal{S},\mathcal{G}}$ can be approximated by

$$\begin{aligned}
\log \mathcal{B}_{\mathcal{S},\mathcal{G}} &\simeq \frac{5N}{2} + 5N \log\left(\frac{\rho}{\sqrt{N}}\right) \\
&- \sum_{n=1}^{N} \log\left(2^{13/6}\pi^{2/3}\mathcal{Q}_n\right) \\
&+ N \log V_\lambda + \left(2 + \log \frac{\sqrt{\det \mathcal{C}_Q}}{4\pi^2}\right) \\
&\approx \frac{5N}{2} + 5N \log\left(\frac{\rho}{\sqrt{N}}\right) , \qquad (4.6)
\end{aligned}$$

where N is the number of wavelets, ρ is the matched-filter SNR, V_λ is the volume of the intrinsic parameter space, $\mathcal{C}_Q$ is the signal parameter covariance matrix, and $\mathcal{Q}_n$ is the quality factor of the n^{th} wavelet. Equation (4.6) is our approximation, made by keeping only the leading order terms which depend on the SNR and number of pixels, i.e. parameters that define the time-frequency signal content (§4.4.1).

We compare the analytical approximation of $\mathcal{B}_{\mathcal{S},\mathcal{G}}$ in Eq. (4.6) with the measured BayesWave output for a range of BBH masses. As discussed in [115], signal-glitch discrimination improves with the number of detectors that see the transient. A GW can be fit with only two polarisations regardless of the number of detectors, while the glitch model needs to explain simultaneous independent noise fluctuations in each detector.

We find that the best predictions for $\mathcal{B}_{\mathcal{S},\mathcal{G}}$ come from using the *minimum* injected SNR for ρ in Eq. (4.6); i.e. the lowest of the SNR in H1, L1 or V1, as this determines whether the least sensitive instrument detected the GW or not. Because we use a single, common Gaussian noise model for all three instruments (see Sec. 4.3), the SNR values differ due to the different antenna responses of the LIGO and Virgo detectors. We chose to use Gaussian noise rather than the measured PSD because this allows us to assess BayesWave performance without effects of detectors having different sensitivity. This in turn would complicate result comparison from multiple injections.

The results are shown in the left panel of Fig. 4.7, where the correlation between measured and predicted $\log \mathcal{B}_{\mathcal{S},\mathcal{G}}$ is evident. The measured log Bayes factors are lower than predicted for the lowest-mass systems, because BayesWave is unable to recover the full SNR of these signals. Low-mass systems require higher SNR per time-frequency pixel, which in turn limits their reconstruction compared to high-mass systems. The predictive power of Eq. (4.6) can be improved further by using the minimum *recovered* SNR instead of the minimum injected SNR.

We can compare these results to the typical log Bayes factor for background noise to establish what real astrophysical signals could be recovered with high confidence. Using real LIGO noise from the 2009-10 run, Littenberg et al. [115] computed log

Bayes factors for coincident events found by the coherent Wave Burst pipeline [100, 101] and showed that a threshold of $\log \mathcal{B}_{\mathcal{S},\mathcal{G}} = 14.4$ corresponds to a FAR of $1/100\,\mathrm{yr}$. In the first Advanced LIGO run, around the time of GW150914, the same FAR value corresponds to $\log \mathcal{B}_{\mathcal{S},\mathcal{G}} \sim 2$–$3$ (see Fig. 4 in [13]). For illustration, we use the higher of these (14.4) as an indicative threshold; this is represented by the red dashed line in the right panel of Fig. 4.7. We see that low time-frequency volume signals are distinguishable from glitches at this FAR provided the SNR is greater than 5–6 in all three detectors, while high time-frequency volume signals are distinguishable for SNR greater than 7–8 in all three detectors.

Finally, we note that BayesWave also provides a log Bayes factor for the signal vs. Gaussian noise hypotheses. Cornish and Littenberg [60] show that this log Bayes factor can be approximated by[2]

$$\begin{aligned} \log \mathcal{B}_{\mathcal{S},\mathcal{N}} &= M^2 \frac{\rho^2_{\mathrm{net}}}{2} + \Delta \ln \mathcal{O} \\ &\approx M^2 \frac{\rho^2_{\mathrm{net}}}{2}\,, \end{aligned} \tag{4.7}$$

where M is the match (discussed below) and ρ_{net} is the coherent network SNR. $\mathcal{O}$ is the Occam factor, which we ignore for our comparisons.

Figure 4.8 shows that the measured signal to Gaussian noise Bayes factor $\log \mathcal{B}_{\mathcal{S},\mathcal{N}}$ follow the predicted signal to Gaussia noise Bayes factor $\log \mathcal{B}_{\mathcal{S},\mathcal{N}}$ values, but are systematically lower by approximately $\sim 20\%$. As for signal to glitch Bayes factor $\log \mathcal{B}_{\mathcal{S},\mathcal{G}}$, we see that the measured Bayes factors are (slightly) lower than the predicted ones for the lowest-mass systems, because BayesWave is unable to recover the full SNR of these signals (Fig. 4.7).

4.4.4 Waveform reconstruction

Many potential sources of GW transients, such as CCSNe and hypermassive NSs formed in BNS mergers, are too complicated to be modelled accurately. In some cases even parts of the underlying physics are unknown (e.g. equation of state of a NS). The ability to reconstruct the received $h(t)$ signal without reliance on accurate "templates" will therefore be crucial for the exploitation of GWs to probe new and unexpected systems.

Back of envelope estimation of the match between the true GW signal with SNR ρ_{inj} and a maximum-likelihood reconstruction of the signal based on a time-frequency pixel analysis can be derived using only the recovered SNR ρ_{rec} and number of pixels N [166],

$$M \simeq \frac{\rho_{\mathrm{rec}}}{\rho_{\mathrm{inj}}} \left(1 + \frac{2N}{\rho^2_{\mathrm{rec}}}\right)^{-1/2} \tag{4.8}$$

[2]Note that there is an error in Eq. (36) of [60]: (1-FF^2) should be FF^2. We use the symbol M (or match) instead of FF (fitting factor).

with a one-sigma fractional uncertainty of

$$\frac{\delta M}{M} \simeq \frac{\sqrt{3}}{\rho_{\rm rec}} \,. \tag{4.9}$$

The $\rho_{\rm rec}/\rho_{\rm inj}$ factor in Eq. (4.8) is due to portions of the signal that are not included in the reconstruction, such as the low-frequency early-time portions of the low-mass signals. The factor in parentheses is due to the noise contamination of those pixels that are included in the reconstructed waveform. These expressions should be most accurate in the limit of high SNR per pixel, $\rho_{\rm rec}^2/N \gg 1$.

Figure 4.9 compares the *mismatch*, $1 - M$, of the waveform reconstructed by BayesWave to the back of envelope estimate from Eq. (4.8). We see that there is broad agreement between the two, with the measured mismatches typically about 50% higher than the first-principles estimate of the lowest achievable mismatch. Not surprisingly, the lowest mismatches are achieved for the signal with smallest time-frequency volume (high masses), where the entire signal in the sensitive band of the detectors, which is limited by noise contamination, is reconstructed. The highest mismatches are for the largest time-frequency volume signals (low masses), where BayesWave is unable to reconstruct the full signal. In these cases, the mismatch is dominated by the BayesWave reconstruction not including the full signal, as opposed to noise contamination of the reconstruction.

4.5 Discussion

BayesWave localises the source on the sky better than timing-only triangulation in all scenarios, and is outperformed by coherent Bayesian matched-filter analyses only for low-mass systems ($\leq 50\,M_\odot$). The measured log Bayes factor for signal-glitch classification follows analytic predictions based on the waveform match accuracy and the coherent network SNR. As a result, low time-frequency volume signals are distinguishable from noise glitches provided SNR $>$ 5–6 in all detectors, and high time-frequency volume signals at SNR $>$ 7–8, at a false-alarm rate of 1/100y. Finally, the match between reconstructed and injected waveforms depends on the SNR and the time-frequency volume over which it is spread. Low time-frequency volume signals can achieve matches above 0.9, while high time-frequency volume signals are more typically around a match of 0.6–0.8. The main limitation for waveform reconstruction is the inability to reconstruct the full signal when its SNR is spread over a large number of pixels, rather than noise contamination of the reconstructed signal.

While our study used BBH signals, a key strength of the BayesWave pipeline is that its performance does not depend on signal morphology, so we expect to achieve similar results for generic unmodelled GW transients. This should be true as long as the number of wavelets required to model the signal is relatively low ($\lesssim 10$ wavelets).

For example, it would be very interesting to assess the performance of waveform reconstruction for signals from the post-merger remnant from BNS systems [16], given the recent detection of GW170817 [15]. Also, the waveforms used in our study [21] do not include spin, eccentricity, or higher-mode contributions for BBH signals. While these effects require substantial changes to waveform modelling and matched-filter analyses, BayesWave should be able to account for all of these effects automatically without modification.

Postface

We have performed an in-depth analysis of the parameter estimation capabilities of BayesWave, an algorithm used for the reconstruction of GW signals without relying on a specific signal model. By performing an injection study with BBH signals, we evaluated BayesWave in three key areas: sky position estimation (§4.4.2), signal/glitch discrimination (§4.4.3), and waveform reconstruction (§4.4.4), and compared its performance to first-principle estimates. We found that BayesWave effectiveness depends mainly on the time-frequency content of the signal: the fewer wavelets needed to reconstruct a signal, the better the performance (§4.4.1). We specifically showed that BayesWave is able to reconstruct BBH waveforms up to match $M \sim 0.95$ for high-mass systems (Fig. 4.9).

In the next chapter we will derive an algorithm that is able to interpret a reconstructed waveform of a GW transient, specifically to reproduce density perturbations $\delta\rho(t, r, \theta, \phi)$ in the source from the reconstructed GW signal $h(t)$.

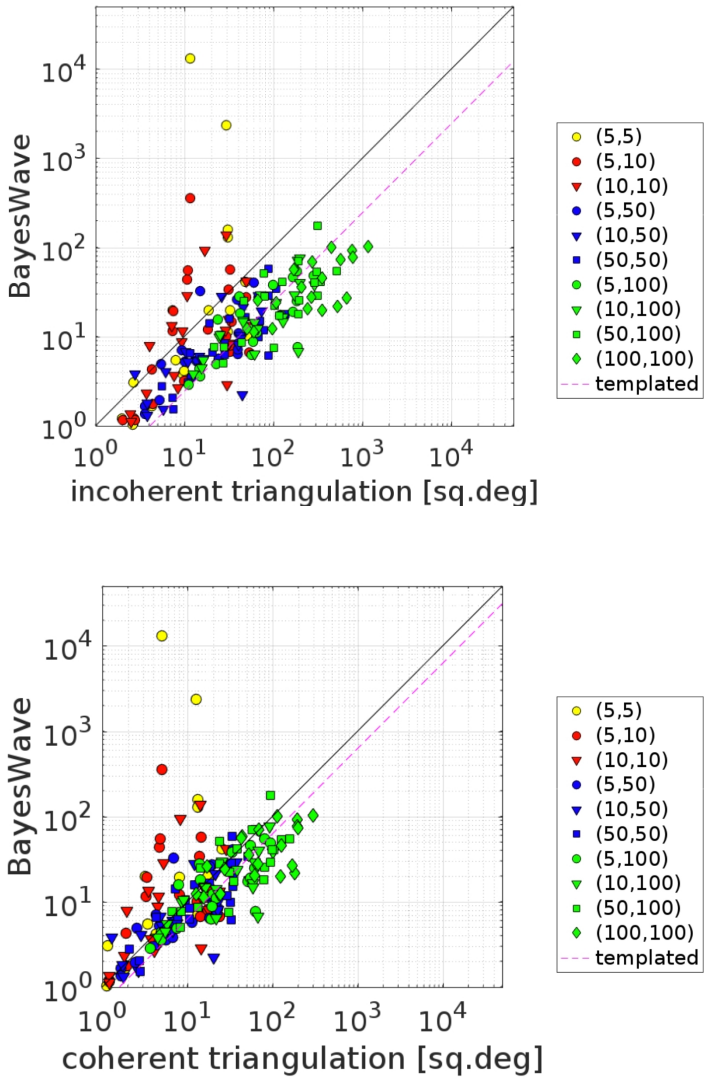

Figure 4.5: 50% containment localisation areas measured by BayesWave versus those predicted by timing-only "incoherent" triangulation (above) and phase- and polarisation-corrected "coherent" triangulation (below). The dashed line indicates the approximate median performance of a templated Bayesian analysis as reported in [84]. BayesWave systematically outperforms the timing-only predictions for all mass pairs. It also systematically outperforms the predictions of phase- and polarisation-corrected triangulation for all but the lowest-mass systems, despite not using a signal template. For system masses above $50\,M_\odot$ the BayesWave performance is approximately equal to that of the templated Bayesian analysis. In both cases smaller-bandwidth signals tend to have larger localisation areas, as expected. The small number of outliers are signals from low-mass systems that BayesWave was unable to reconstruct accurately.

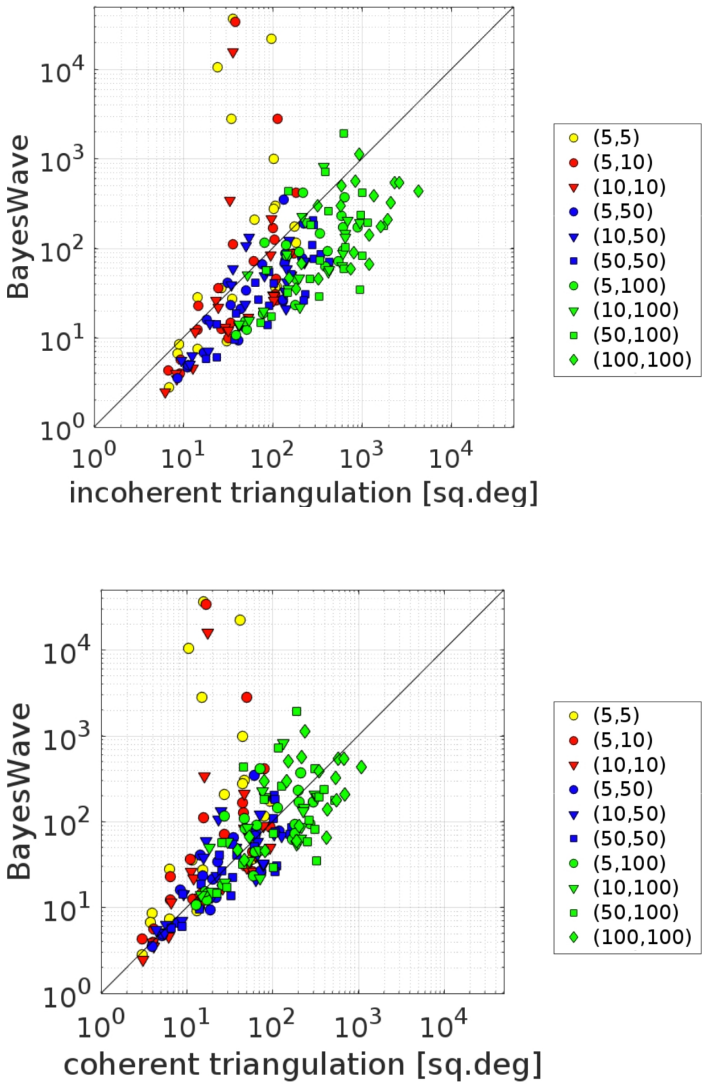

Figure 4.6: 90% containment localisation areas measured by BayesWave versus those predicted by timing-only "incoherent" triangulation (above) and phase- and polarisation-corrected "coherent" triangulation (below). BayesWave systematically outperforms the timing-only predictions for all mass pairs. It also systematically outperforms the predictions of phase- and polarisation-corrected triangulation for all but the lowest-mass systems, despite not using a signal template. In both cases smaller-bandwidth signals tend to have larger localisation areas, as expected. The small number of outliers are signals from low-mass systems that BayesWave was unable to reconstruct accurately.

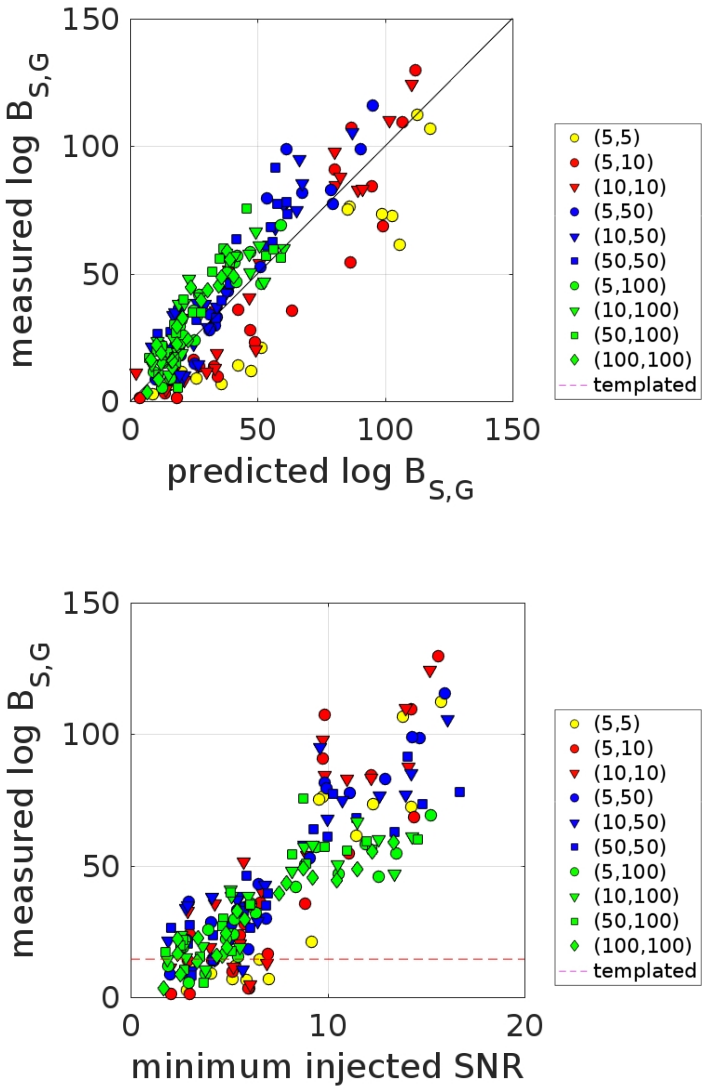

Figure 4.7: (Above) Predicted and measured log Bayes factors for the Signal vs. Glitch test. The measured log Bayes factors are in good agreement with the predicted analytical expressions from [115] and [60], except for the lowest-mass systems, for which BayesWave is unable to recover the full SNR. (Below) Measured log Bayes factors vs. minimum injected SNR. The red dashed line indicates a log $\mathcal{B}_{\mathcal{S},\mathcal{G}}$ threshold that corresponds to a FAR of 1/100 yr. Low time-frequency volume signals are distinguishable from glitches at this FAR provided the SNR is greater than 5–6 in all three detectors. High time-frequency volume signals are distinguishable for SNR greater than 7–8 in all three detectors.

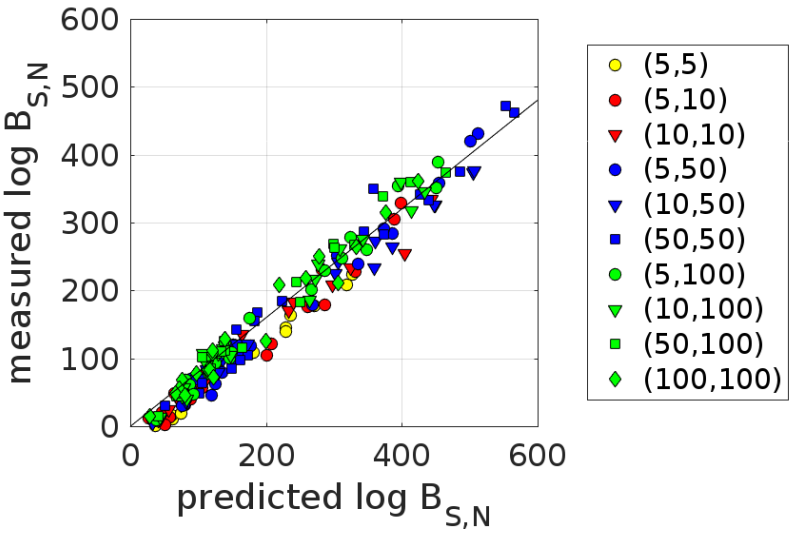

Figure 4.8: Predicted and measured log Bayes factors for the Signal vs. Gaussian noise test. The measured log Bayes factors are in very good agreement with predicted analytical expressions from [115] and [60] based on the total injected network SNR and the time-frequency volume of the signal. The measured log Bayes factors are about 20% systematically lower than the predicted ones. This is slightly more prevalent for the lightest-mass (highest time-frequency volume) systems, for which BayesWave is unable to recover the full SNR.

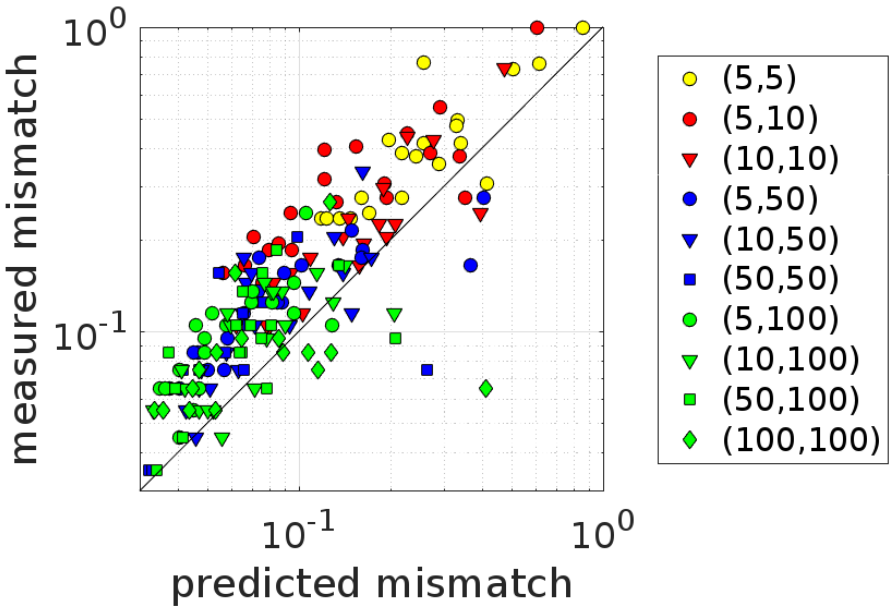

Figure 4.9: Measured mismatches between the true injected signal and that reconstructed by BayesWave, compared to a first-principles estimate of the lowest achievable mismatch. The measured mismatches are in broad agreement with the first-principles estimate, but are typically 50% higher. The mismatches are smallest for the smallest time-frequency volume signals (high-mass systems), and largest for the largest time-frequency volume signals (low-mass systems) for which BayesWave is unable to reconstruct the full signal. [For visual clarity, we do not show the error bars on the measured mismatches.]

Chapter 5

Reconstructing source density perturbations

As a brief reminder, in Chapter 3 we showed how an unmodelled GW transient can be detected using the excess power method. In particular, we introduced a targeted X-Pipeline search for GWs associated with GRBs. In Chapter 4 we presented a study that estimated how well we can reconstruct GW burst parameters such as sky location and especially the waveform $h_{+,\times}(t)$. We demonstrated that the overall reconstruction effectiveness mainly depends on the time-frequency content of the signal; i.e., the fewer wavelets are needed to reconstruct a signal, the better the performance.

In this chapter we present a technique for reconstructing the source density perturbations that produced the gravitational wave. We show that while the GW signal provides some constraints on these perturbations it does not contain sufficient information to determine the perturbations uniquely. We then conclude by presenting a Bayesian formulation that provides a way to systematically incorporate prior information on the source to further constrain the density perturbations.

5.1 Introduction

The history of science teaches us that every new astronomical window unveiled previously unknown phenomena (§2.5). It is possible that gravitational waves, a completely different way of observing the Universe, could lead to undiscovered astrophysics. It is therefore essential to have tools that not only detect unknown GWs but also that are able to interpret the unmodelled signal.

Ideally, we would like to infer the structure of a GW source from its reconstructed waveform $h_{+,\times}(t)$. For example, the particular waveform in Fig. 5.1a is computed from a core-collapse supernova with density evolution over time given in Fig. 5.1b. In this chapter we present an algorithm that is able to reconstruct density perturbations $\delta\rho(t, r, \theta, \phi)$ consistent with the waveform $h_{+,\times}(t)$, although with some limitations.

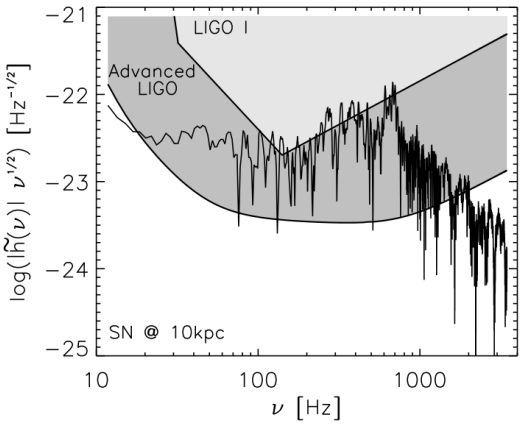

(5.1a) Gravitational waveform $|\tilde{h}(w)|$ of a core-collapse supernova 10 kpc away. LIGO and Advanced LIGO sensitivity curves are shown in light and dark grey, respectively. Figure taken from [131].

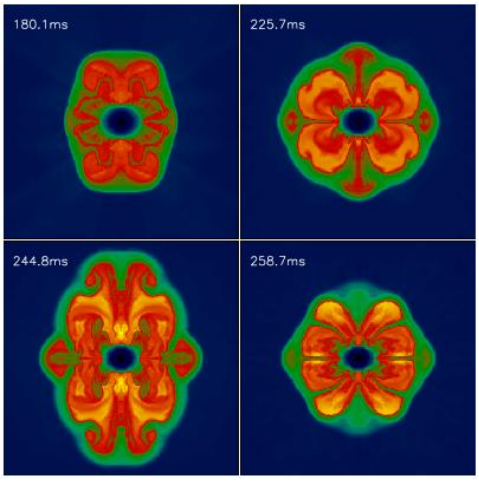

(5.1b) Temporal evolution of non-radial pulsations in the post-shock region of a CCSN from a rotating $15M_{\odot}$ progenitor. The resulting gravitational waveform $|\tilde{h}(w)|$ is given on left. Figure taken from [131].

5.2 Theory

For a slowly moving source in the weak-field limit, the gravitational-wave strain is given by 'reduced' (traceless) quadrupole equation

$$h_{ij}(t) = \frac{2}{D}\frac{\mathrm{d}^2}{\mathrm{d}t^2}\int \rho(t,r,\theta,\phi)[x^i x^j - \frac{1}{3}\delta^{ij}r^2]\mathrm{d}^3\vec{x}, \tag{5.1}$$

where $h_{ij}(t)$ is the gravitational-wave strain, D and ρ are the distance to the source and the density of the source respectively. Eq. (5.1) has the extra $-\frac{1}{3}\delta^{ij}r^2$ term because we will always use coordinates where the observer is on the z-axis, then the δ^{ij} term acts as a transverse-traceless projection.

Eq. (5.1) basically means that any non-spherical accelerating source radiates GWs. Following the example given in the previous section, we want to find $\rho(t,r,\theta,\phi)$ from $h_{ij}(t)$. We cannot expect to reconstruct density $\rho(t,r,\theta,\phi)$ fully only from the waveform $h_{+,\times}(t)$ as the GW signal does not contain enough information. For example, because of the transverse-traceless projection we get only *two* GW polarisations to reconstruct *six* components of the quadrupole moment tensor I^{ij} (§1.1.2). It is also not straightforward to invert this equation because of the triple integration over radial and angular parts, and the second time derivative. We will explore to what extent we can reconstruct $\rho(t,r,\theta,\phi)$ purely from $h_{+,\times}(t)$ and where we need to add physical priors or assumptions.

Let us have a look at the density $\rho(t,r,\theta,\phi)$. Assuming that radiation from a slightly non-spherical compact body is caused by a density perturbation, we can

separate density in two contributions

$$\rho(t, r, \theta, \phi) = \rho_0(t, r, \theta, \phi) + \delta\rho(t, r, \theta, \phi), \tag{5.2}$$

where $\rho_0(t, r, \theta, \phi)$ is density that does not contribute to the GW emission, i.e. monopole and dipole terms of the mass density, as well as any linear dependence of density in time. The other term, which we define as density perturbation $\delta\rho(t, r, \theta, \phi)$, contains the quadrupole term of the mass density.

We can neglect the ρ_0 term from Eq. (5.2) when considering the GW emission. Thus we can write

$$\rho_{GW}(t, r, \theta, \phi) = \delta\rho(t, r, \theta, \phi). \tag{5.3}$$

We can decompose this density perturbation $\delta\rho(t, r, \theta, \phi)$ into modes

$$\delta\rho(t, r, \theta, \phi) = \sum_n \sum_{lm} \delta\rho^{lmn}(t)\ F_n(r)\ Y_{lm}(\theta, \phi), \tag{5.4}$$

where $Y_{lm}(\theta, \phi)$ and $F_n(r)$ are any complete sets of basis functions on the unit sphere and $[0, R]$ respectively, where R is the maximum spatial size of the portion of the source that emits GWs. An upper limit on R can be derived from the maximum observed GW frequency: $R \leq \frac{c}{2f_{max}}$, where f_{max} is the maximum observed GW frequency [52]. In our following calculations we chose spherical harmonics $Y_{lm}(\theta, \phi)$ for the angular part and Fourier modes $F_n(r)$ for the radial part. We discuss our choice of basis functions and the consequences of it in §5.2.

Once the density perturbation $\delta\rho(t, r, \theta, \phi)$ is decomposed into modes, the integral in Eq. (5.1) can be solved. To do that, substitute Eq. (5.4) into Eq. (5.1),

$$\begin{aligned} h_{ij}(t) =& \frac{2}{D} \sum_n \sum_{lm} \left(\frac{\mathrm{d}^2}{\mathrm{d}t^2} \delta\rho^{lmn}(t) \right) \times \\ & \int_0^R \int_0^\pi \int_0^{2\pi} F_n(r)\ Y_{lm}(\theta, \phi)\ \left[x^i x^j - \frac{1}{3}\delta^{ij} r^2 \right]\ r^2 \mathrm{d}r \sin\theta \mathrm{d}\theta \mathrm{d}\phi, \end{aligned} \tag{5.5}$$

where $x^i = (x,\ y,\ z) = r \times (\sin\theta\cos\phi,\ \sin\theta\sin\phi,\ \cos\theta)$ in spherical coordinates.

We can further simplify Eq. (5.5) by change of variables $u = \frac{r}{R}$,

$$\begin{aligned} h_{ij}(t) =& \frac{2R^5}{D} \sum_{lmn} \left(\frac{\mathrm{d}^2}{\mathrm{d}t^2}\ \delta\rho^{lmn}(t) \right) \times \\ & \int_0^1 \int_0^\pi \int_0^{2\pi} F_n(u)\ Y_{lm}(\theta, \phi)\ [\tilde{x}^i \tilde{x}^j - \frac{1}{3}\delta^{ij} u^2]\ u^2 \mathrm{d}u \sin\theta \mathrm{d}\theta \mathrm{d}\phi \\ =& \frac{2R^5}{D} \sum_{lmn} \left(\frac{\mathrm{d}^2}{\mathrm{d}t^2}\ \delta\rho^{lmn}(t) \right) G^{ij}_{lmn}, \end{aligned} \tag{5.6}$$

where $\tilde{x}^i = u \times (\sin\theta\cos\phi,\ \sin\theta\sin\phi,\ \cos\theta)$ in spherical coordinates. We also introduced a new quantity that we call 'emissivity', G^{ij}_{lmn}, which is the triple integral that

depends on basis functions $Y_{lm}(\theta, \phi)$ and $F_n(r)$. For a given set of $\{l, m, n\}$ modes, the emissivity term G^{ij}_{lmn} can be estimated analytically, hence is just a number.

We look for transient sources, i.e. they should emit GWs in the sensitive band of an interferometer over a finite time interval $t \in [0, T]$. Using a change of variables $\tau = \frac{t}{T}$ in Eq. (5.6) we get

$$\begin{aligned} h_{ij}(\tau) &= \frac{2R^5}{D} \sum_{lmn} G^{ij}_{lmn} \; \frac{1}{T^3} \left(\frac{\mathrm{d}^2}{\mathrm{d}\tau^2} \delta\rho^{lmn}(\tau) \right) \\ &= \frac{2R^5}{D} \sum_{lmn} G^{ij}_{lmn} \frac{1}{T^3} \; a^{lmn}(\tau) \\ &= \frac{2R^5}{D} \sum_{lmn} G^{ij}_{lmn} \frac{1}{T^3} \; \sum_k c^{lmn}_k \, p^k(\tau) \\ &= \frac{2R^5}{DT^3} \sum_{lmn} G^{ij}_{lmn} \sum_k c^{lmn}_k \, p^k(\tau), \end{aligned} \tag{5.7}$$

where we defined $a^{lmn}(\tau) \equiv \frac{\mathrm{d}^2}{\mathrm{d}\tau^2} \delta\rho^{lmn}(\tau)$ and $p^k(\tau)$ is any complete set of orthonormal basis functions on $[0, 1]$. For convenience we chose Fourier modes $p^k(\tau) = e^{-i2\pi k\tau}$, where $k \in \mathbb{Z}$. Then $w = \frac{2\pi k}{T}$ is the physical angular frequency.

Now integrate both sides of Eq. (5.7) by $\int_0^1 p^*_\lambda(\tau)\mathrm{d}\tau$

$$\begin{aligned} \int_0^1 h_{ij}(\tau)\, p^*_\lambda(\tau)\mathrm{d}\tau &= \frac{2R^5}{DT^3} \sum_{lmn} G^{ij}_{lmn} \sum_k c^{lmn}_k \int_0^1 p^k(\tau) p^*_\lambda(\tau)\mathrm{d}\tau \\ \tilde{h}_{ij}(w) &= \frac{2R^5}{DT^3} \sum_{lmn} G^{ij}_{lmn} \, c^{lmn}_\lambda, \end{aligned} \tag{5.8}$$

where we used orthonormality, $\int_0^1 p^k(\tau) p^*_\lambda(\tau) d\tau = \delta^k_\lambda$. In the burst searches the waveform $\tilde{h}_{ij}(w)$ is reconstructed using an unmodelled wavelet fitting, e.g. BayesWave [60] or coherent Wave Burst [100]. The emissivity G^{ij}_{lmn} is fixed by the choice of basis modes and can be computed (analytically or numerically) for each $\{l, m, n\}$. This leaves only two unknown quantities in Eq. (5.8): the scaling constant $\frac{2R^5}{DT^3}$ and the mode coefficients c^{lmn}_λ.

Assuming that coefficients $\{l, m, n\}$ are finite, we can simplify Eq. (5.8) by combining $\{l, m, n\}$ into a single index α such that α spans over all distinct combinations of $\{l, m, n\}$,

$$\tilde{h}_{ij}(w) = \frac{2R^5}{DT^3} \sum_{lmn} G^{ij}_{lmn} \, c^{lmn}_\lambda = \frac{2R^5}{DT^3} \sum_\alpha G^{ij}_\alpha \, c^\alpha_\lambda, \tag{5.9}$$

or in matrix notation

$$\tilde{\mathbf{h}}_{\mathbf{ij}} = \frac{2R^5}{DT^3} \, \mathbf{G^{ij}} \, \mathbf{c}, \tag{5.10}$$

where $\tilde{\mathbf{h}}_{\mathbf{ij}}$ is the Fourier transformed $h_{ij}(t)$ and is a row vector of dimensions $(1, N_k)$, where N_k is the number of temporal modes. The emissivity $\mathbf{G^{ij}}$ is a row vector of

dimensions $(1, N_\alpha)$ where α spans over all possible $\{l, m, n\}$ combinations. The factor $\mathbf{c}$ is a (N_α, N_k) matrix.

We can solve Eq. (5.10) for the coefficient c using the Moore-Penrose inverse[1] of G^{ij},

$$\begin{aligned}\frac{DT^3}{2R^5}\big(\mathbf{G^{ij,\dagger}}\,\mathbf{G^{ij}}\big)^{-1}\mathbf{G^{ij,\dagger}}\;\tilde{\mathbf{h}}_{\mathbf{ij}} &= \big(\mathbf{G^{ij,\dagger}}\,\mathbf{G^{ij}}\big)^{-1}\big(\mathbf{G^{ij,\dagger}}\,\mathbf{G^{ij}}\big)\mathbf{c}\\ \Rightarrow \mathbf{c} &= \frac{DT^3}{2R^5}\big(\mathbf{G^{ij,\dagger}}\,\mathbf{G^{ij}}\big)^{-1}\mathbf{G^{ij,\dagger}}\;\tilde{\mathbf{h}}_{\mathbf{ij}}\\ &= K\,\mathcal{G}^{\mathbf{ij}}\,\tilde{\mathbf{h}}_{\mathbf{ij}},\end{aligned} \tag{5.11}$$

where † denotes the complex conjugate, $K \equiv \frac{DT^3}{2R^5}$ and $\mathcal{G}^{ij} \equiv \big(\mathbf{G^{ij,\dagger}}\,\mathbf{G^{ij}}\big)^{-1}\mathbf{G^{ij,\dagger}}$. It is important to note that the solution for c depends on which projection ij we use. That is, we may get different answers if we compute c using the plus or cross polarisation of the waveform. We will show in §5.5 that the individual estimates of c can be combined to one by a weighted sum of both detected GW polarisations.

We can now rewrite $\delta\rho(\tau, r, \theta, \phi)$ from Eq. (5.4) using the solution for c (Eq. (5.11)):

$$\delta\rho(\tau, r, \theta, \phi) = \sum_{lmn} \delta\rho^{lmn}(\tau)\, F_n(r)\, Y_{lm}(\theta, \phi) \tag{5.12}$$

$$= \sum_{lmn} \int^{\tau} \left(\int^{\tau'} a^{lmn}(\tau'')\mathrm{d}\tau'' \right) \mathrm{d}\tau'\, F_n(r)\, Y_{lm}(\theta, \phi) \tag{5.13}$$

$$= \sum_{k} \sum_{lmn} c_k^{lmn} \left(\frac{e^{-iw_k\tau}}{-w_k^2} \right) F_n(r) Y_{lm}(\theta, \phi) \tag{5.14}$$

$$= \sum_{k} \sum_{lmn} K\, \mathcal{G}^{ij,\,lmn} \tilde{h}_{ij,\,k} \left(\frac{e^{-iw_k\tau}}{-w_k^2} \right) F_n(r) Y_{lm}(\theta, \phi) \tag{5.15}$$

$$= K \times \left[\sum_{lmn} \mathcal{G}^{ij,\,lmn} F_n(r) Y_{lm}(\theta, \phi) \right] \times \left[\sum_{k} \tilde{h}_{ij,\,k} \frac{e^{-iw_k\tau}}{-w_k^2} \right] \tag{5.16}$$

$$= \text{constant} \times \text{purely spatial part} \times \text{purely temporal part.} \tag{5.17}$$

Equation (5.16) is a formal solution which allows us to reconstruct the density perturbation $\delta\rho(\tau, r, \theta, \phi)$ using the waveform $\tilde{h}_{ij,\,k}(w_k)$ and emissivity $\mathcal{G}^{ij}$ (Eq. (5.11)). In other words, we derived a solution to infer a density perturbation $\delta\rho(\tau, r, \theta, \phi)$ of a GW source that is consistent with reconstructed waveform $h_{+,\times}(t)$. The factor $\mathcal{G}^{ij}$ is responsible for reconstructing the spatial part, while the waveform $\tilde{h}_{ij,\,k}$ reconstructs the time part of the signal. It is also worth noting that the $\frac{1}{-w_k^2}$ factor in Eq. (5.16) will cause problems at low frequencies if the measured signal $\tilde{h}_{ij,\,k}$ is contaminated by noise.

[1] Moore-Penrose inverse is a least-squares ('best-fit') method to solve a linear equation. Another way to inverse Eq. (5.10) could be achieved with Bayes thorem; we will considerthis in §5.5.

Emissivity G^{ij}_{lmn}

Our derived solution (Eq. (5.16)) relies on decomposition using basis functions, therefore it is important to understand the emissivity term G^{ij}_{lmn} used in our calculations. The emissivity was introduced in Eq. (5.6) which is simply an integral that entirely depends on the $\{l, m, n\}$ modes,

$$G^{ij}_{lmn} = \int_0^1 \int_0^\pi \int_0^{2\pi} F_n(u)\ Y_{lm}(\theta, \phi)\ [\tilde{x}^i \tilde{x}^j - \frac{1}{3}\delta^{ij} u^2]\ u^2 \mathrm{d}u \sin\theta \mathrm{d}\theta \mathrm{d}\phi, \tag{5.18}$$

where $\tilde{x}^i = u \times (\sin\theta\cos\phi,\ \sin\theta\sin\phi,\ \cos\theta)$ in spherical coordinates. We refer to the G^{ij}_{lmn} as emissivity because it defines how strong the emission of a GW source is due to a particular mode $\{l, m, n\}$.

For our tests we choose the function $F_n(u)$ in Eq. (5.18) to be Fourier modes, defined as $F_n(u) = e^{-i2\pi nu}$, where $n \in \mathbb{Z}$. The spherical harmonics $Y_{l,m}(\theta, \phi)$ are defined as

$$\begin{aligned} Y_{l,m}(\theta, \phi) &= \sqrt{\frac{(2l+1)}{4\pi}\frac{(l-m)!}{(l+m)!}}\ e^{im\phi} P_l^m(x) \\ &= \frac{(-1)^m}{2^l l!}\sqrt{\frac{(2l+1)}{4\pi}\frac{(l-m)!}{(l+m)!}}\, e^{im\phi}\,(1-x^2)^{\frac{m}{2}}\frac{\mathrm{d}^{l+m}}{\mathrm{d}x^{l+m}}(x^2-1)^l, \end{aligned} \tag{5.19}$$

where $P_l^m(x)$ is the associated Legendre polynomial and $x \equiv \cos\theta$. For negative m values, $Y_{l,-m}(\theta, \phi) = (-1)^m \bar{Y}_{l,m}(\theta, \phi)$, where $\bar{Y}_{l,m}(\theta, \phi)$ is complex conjugate of $Y_{l,m}(\theta, \phi)$.

We chose spherical harmonics $Y_{l,m}(\theta, \phi)$ and Fourier modes $F_n(u)$ as our basis functions for the emissivity integral, but any other complete set of orthonormal basis functions could be chosen instead. The best choice of modes is the set that is able to model the motion of a source with as fewer modes as possible.

The spherical harmonics basis is a natural choice of modes for reconstructing the angular part because the gravitational radiation is dominated by the quadrupole term, and $Y_{l=2,\, m\pm2}(\theta, \phi)$ represents this motion very well. In fact it can be shown that for an observer on the z-axis all other $Y_{l,\, m}(\theta, \phi)$ modes than $l = 2$, $m = \pm 2$ are zero for $h_{+,\times}(t)$ from Eq. (5.1). We choose to define our coordinate system so that this is always the case. For other coordinate choices reconstructing the quadrupole radiation would require other m modes of degree $l = 2$, e.g. $|m| = 1$.

For the radius part reconstruction we chose Fourier modes $F_n(u)$ for simplicity. There could be other modes that encapsulate the gravitational radiation in the radial part more efficiently, but we do not consider them here.

5.3 Testing the algorithm

5.3.1 Spinning quadrupole ('220')

One of the simplest sources to test is a spinning quadrupole source defined as

$$\delta\rho(t, r, \theta, \phi) = A\ e^{-\frac{t^2}{2\sigma^2}}\ \Theta(R-r)\ \mathrm{Re}\big[Y_{2,2}(\theta, \phi - \Omega_0 t)\big], \tag{5.20}$$

where A, σ and Ω_0 have units of density, time and frequency respectively. $\Theta(R-r)$ is a step function and Ω_0 is the angular rotation frequency. In our example we chose $t = [-0.5, 0.5]\,\mathrm{s}$, $\sigma = 0.1\,\mathrm{s}$ and $\Omega_0 = 200\pi\,\mathrm{rad/s}$. Essentially, this density perturbation is a spinning quadrupole around the z-axis with a Gaussian envelope.

Using Eq. (5.1) we can estimate the waveform $h(t)$ for the sample source:

$$h_{xx}(t) = -h_{yy}(t) = \frac{4}{25}\sqrt{\frac{5\pi}{6}}\ \frac{AR^5}{d}\ e^{-\frac{t^2}{2\sigma^2}}\ \Bigg[\cos(2\Omega_0 t)\bigg(\frac{t^2}{\sigma^4} - \frac{1}{\sigma^2} - 4\Omega_0^2\bigg) + \\ + \sin(2\Omega_0 t)\frac{4\Omega_0 t}{\sigma^2}\Bigg], \tag{5.21}$$

and

$$h_{xy}(t) = h_{yx}(t) = \frac{4}{25}\sqrt{\frac{5\pi}{6}}\ \frac{AR^5}{d}\ e^{-\frac{t^2}{2\sigma^2}}\ \Bigg[\sin(2\Omega_0 t)\big(\frac{t^2}{\sigma^4} - \frac{1}{\sigma^2} - 4\Omega_0^2\big) - \\ - \cos(2\Omega_0 t)\frac{4\Omega_0 t}{\sigma^2}\Bigg]. \tag{5.22}$$

It is trivial to convert Eqs. (5.21) and (5.22) to the frequency domain:

$$\tilde{h}_{xx}(w) = -\frac{2\pi}{25}\sqrt{\frac{5}{3}}\ \frac{AR^5}{d}\ \sigma\ \Omega_o^2\ \Big[e^{-2\sigma^2(\frac{w}{2}+\Omega_o)^2} + e^{-2\sigma^2(\frac{w}{2}-\Omega_o)^2}\Big], \tag{5.23}$$

$$\tilde{h}_{xy}(w) = -i\frac{2\pi}{25}\sqrt{\frac{5}{3}}\ \frac{AR^5}{d}\ \sigma\ \Omega_o^2\ \Big[e^{-2\sigma^2(\frac{w}{2}+\Omega_o)^2} - e^{-2\sigma^2(\frac{w}{2}-\Omega_o)^2}\Big], \tag{5.24}$$

where we keep t instead of τ because $T = 1\,\mathrm{s}$, hence $t = \tau$. For illustration purposes we show $h_+ = \frac{h_{xx}-h_{yy}}{2}$ for an observer on the z-axis in the time and frequency domains (Figs. 5.2a and 5.2b). As expected, one can see that the 220 source has an exponential envelope $e^{-\frac{t^2}{2\sigma^2}}$ (Fig. 5.2a). The frequency domain plot (Fig. 5.2b) shows that the signal oscillates at the angular frequency $w = 400\pi\,\mathrm{rad/s}$, i.e. twice the rotational frequency $\Omega_0 = 200\pi\,\mathrm{rad/s}$.

Procedure

In this section we describe the step-by-step procedure to reconstruct $\delta\rho(t, r, \theta, \phi)$ for the spinning quadrupole ('220') source. The flowchart is shown in Fig. 5.3.

Firstly, we analytically derive the GW strain in the plus and cross polarisa-

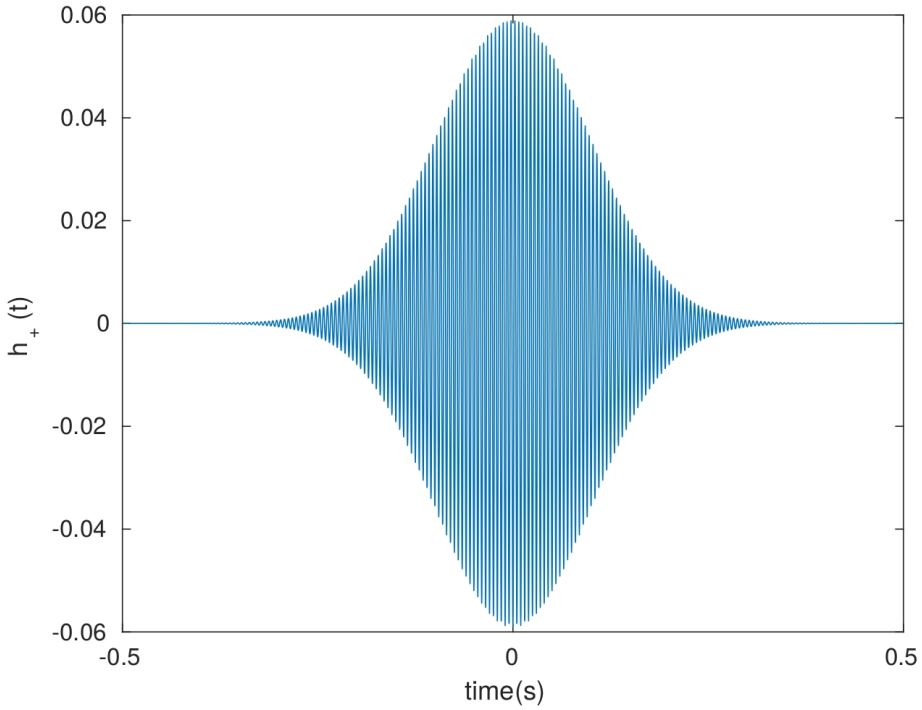

(5.2a) Gravitational waveform $h_+(t)$ for the spinning quadrupole ('220') source. The figure clearly shows a Gaussian envelope with a maximum at time $t = 0$.

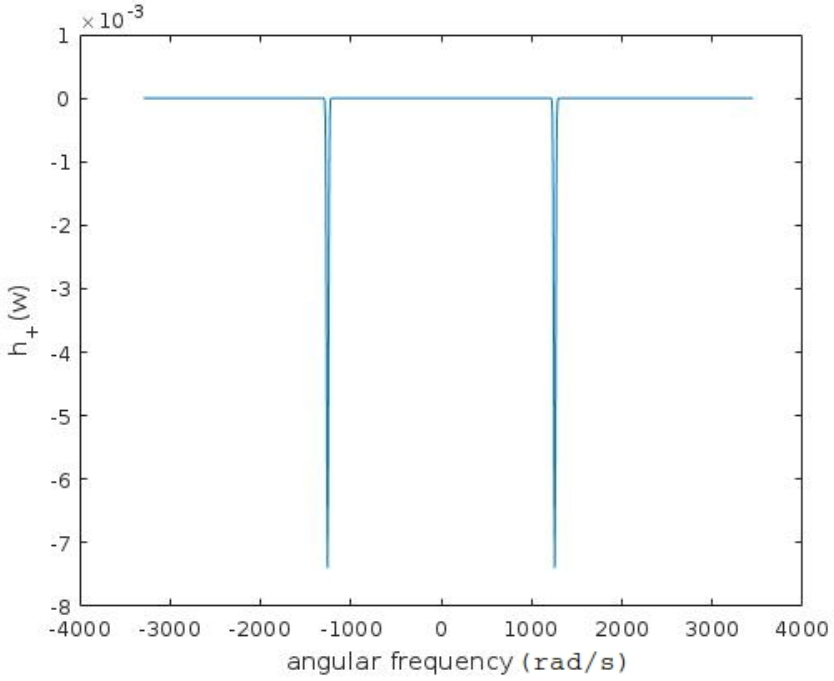

(5.2b) Gravitational waveform $\tilde{h}_+(w)$ in the frequency domain for the spinning quadrupole ('220') source. The two peaks indicate an oscillation frequency of 400π rad/s which is twice the source angular rotational frequency $\Omega_0 = 200\pi$ rad/s.

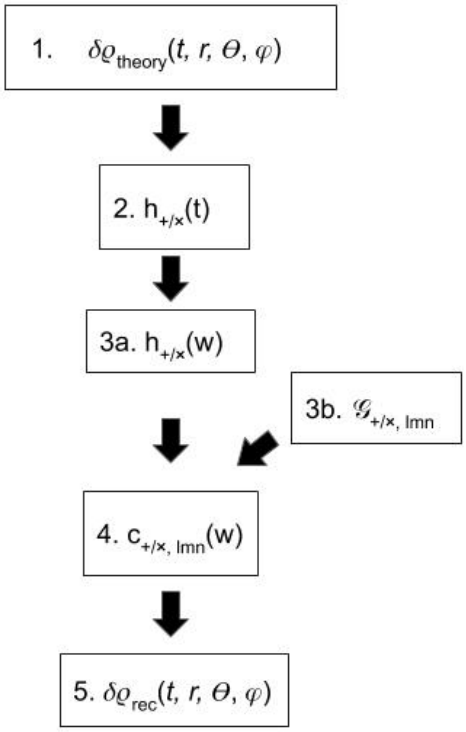

Figure 5.3: The flowchart that describes the procedure to calculate $\delta\rho_{\text{rec}}(t, r, \theta, \phi)$ from $\delta\rho_{\text{theory}}(t, r, \theta, \phi)$ for the spinning quadrupole source.

tions $h_{+,\times}$ using Eqs. (5.20) and (5.1). Then we find the Fourier transform of $h_{+,\times}(t)$ to get $\tilde{h}_{+,\times}(w)$ (step 3a). In step 3b we choose $\{l, m, n\}$ modes in order to calculate the emissivity G^{ij}_{lmn} (Eq. (5.18)) for the plus and cross polarisations. Since the source density is constant in radius, the $n = 0$ mode is enough to reconstruct it[2]. For the angular part we pick $l = 2$, $m = \pm 2$ because these are the only non-zero $Y_{l,m}(\theta, \phi)$ modes for the quadrupole approximation for an observer on the z-axis. Having $\{\tilde{h}_+(w), \tilde{h}_\times(w)\}$ and $\{G_{+,\{2,\pm2,0\}}, G_{\times,\{2,\pm2,0\}}\}$ we can estimate $\{c_{+,\{2,\pm2,0\}}(w), c_{\times,\{2,\pm2,0\}}(w)\}$ using Eq. (5.11) in step 4. Finally, we can substitute coefficients $\{c_{+,\{2,\pm2,0\}}(w), c_{\times,\{2,\pm2,0\}}(w)\}$ into Eq. (5.16) to reconstruct $\delta\rho(t, u, \theta, \phi)$.

Match: no noise

Following the procedure outlined in the previous section, we are able to reconstruct $\delta\rho(t, u, \theta, \phi)$ from $\delta\rho_{\text{theory}}(t, u, \theta, \phi)$ for the spinning quadrupole source. This allows us to compare reconstructed and theoretical density perturbations using the 'match':

$$M = \frac{(\delta\rho_{\text{theory}} \,|\, \delta\rho_{\text{rec}})}{\sqrt{(\delta\rho_{\text{theory}}|\delta\rho_{\text{theory}})(\delta\rho_{\text{rec}}|\delta\rho_{\text{rec}})}}, \tag{5.25}$$

[2]For real sources we could not make this assumption.

where $(.|.)$ is the inner product for functions a and b defined as

$$(a\,|\,b) = 2\int_0^t \int_0^1 \int_0^\pi \int_0^{2\pi} \big[a(t,u,\theta,\phi)\, b^*(t,u,\theta,\phi) + a^*(t,u,\theta,\phi)\, b(t,u,\theta,\phi)\big] u^2 \sin\theta \,\mathrm{d}t\,\mathrm{d}u\,\mathrm{d}\theta\,\mathrm{d}\phi. \tag{5.26}$$

For the case when there is no noise, our algorithm is able to fully reconstruct the original density perturbation $\delta\rho(t,u,\theta,\phi)$ for the 220 source, i.e. $M = 1$.

Match: Gaussian noise

We find that even with a very small amount of noise added to the waveform $h_{+,\times}(t)$ our algorithm does not work anymore. For example, we get match $M = 0.02$ for a signal of SNR ≈ 2000. This is caused by noise at low frequency being 'up-weighted' due to the factor $1/w_k^2$ in Eq. (5.16), see Fig. 5.4a.

There are three ways to deal with this issue, namely

1. Regularisation when w_k^2 is replaced by $(w_k^2 + C)$ where C is some constant. This down-weights frequencies below $\sim \sqrt{C}$ and the solution does not go to infinity at low values of w_k^2.

2. Applying a bandpass filter to remove low frequencies from the signal, hence avoiding the solution going to infinity at low frequencies.

3. Use only the frequencies included in the detected event, e.g. the wavelets in the BayesWave trigger. This option is left for future study.

The algorithm works much better by applying the bandpass filter; i.e. solution no. 2. It is enough to remove everything below $|w| = 120\pi$ rad/s to achieve $M > 0.99$ for a signal with SNR ≈ 2000 instead of $M = 0.02$ when no filter is applied. Figure 5.4b shows how the filtered $\tilde{h}_+(w)$ looks for the spinning quadrupole source.

After the data is bandpassed with the filter we have just defined, we can estimate the match M dependence on the SNR for Gaussian noise. Figure 5.5 shows how match M varies with SNR for the spinning quadrupole 220 source. The density perturbation $\delta\rho(t,u,\theta,\phi)$ is reconstructed with $M = 0.9\,(0.5)$ for SNR $\approx 130\,(35)$.

5.3.2 Binary black hole merger

The next source that we test is a BBH merger. Comparing with the previous example, a BBH merger is a more complicated source: radius decreases, frequency increases and mass density is essentially a point rather than uniform. We use a numerical waveform of a BBH merger GW150914 shown in Fig. 5.6a from [111]. In order to avoid the low frequency up-weighting, we bandpass the waveform $h(t)$ with a filter, i.e. we zero the data below $|f| = 60\,\mathrm{Hz}$. As can be seen from Figure 5.6b, the bandpassed waveform does not have an early inspiral part as expected.

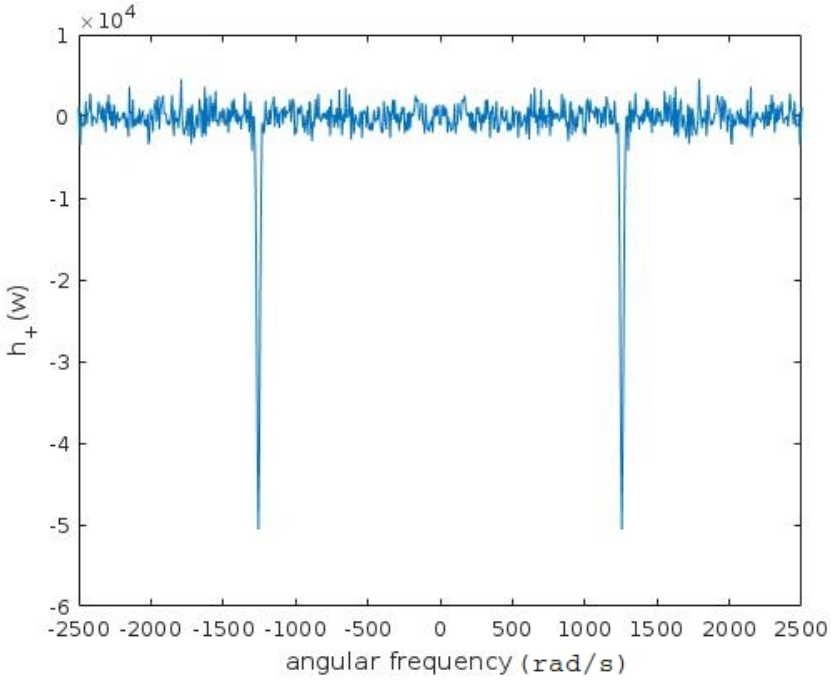

(5.4a) Gravitational waveform $|\tilde{h}_+(w)|$ for the spinning quadrupole ('220') source with added Gaussian noise and no bandpass filter applied. Signal-to-noise ratio is 53 while the match $M = 0.0013$.

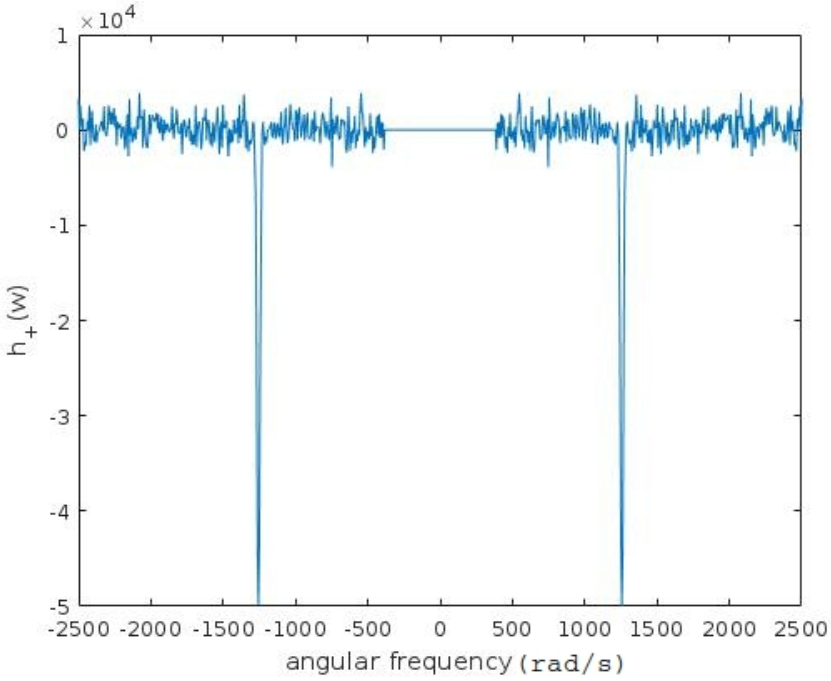

(5.4b) Gravitational waveform $|\tilde{h}_+(w)|$ for the spinning quadrupole ('220') source with added Gaussian noise and a bandpass filter applied for $|w| < 120\pi$ rads. Signal-to-noise ratio is 53 while the match $M = 0.68$.

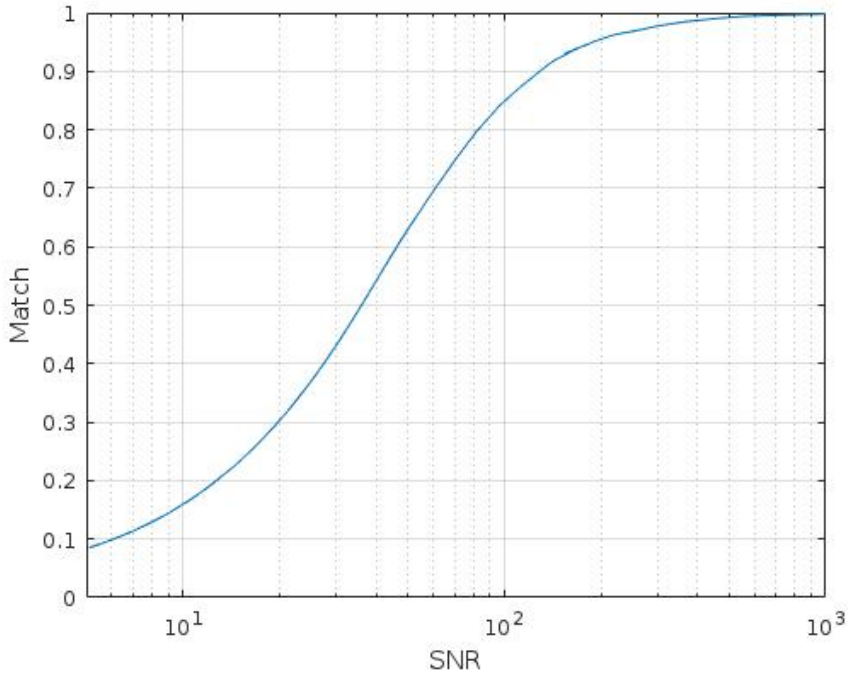

Figure 5.5: Match dependence on the signal-to-noise ratio for the spinning quadrupole source with Gaussian noise. The density perturbation $\delta\rho(t, r, \theta, \phi)$ is reconstructed with $M = 0.9\,(0.5)$ for SNR $\approx 130\,(35)$.

We use this waveform $\tilde{h}(w)$ to reconstruct the density perturbation $\delta\rho(t, u, \theta, \phi)$ with the procedure outlined in §5.3.1. We start from step 2 since we do not have a theoretical $\delta\rho(t, u, \theta, \phi)$, only the waveform $h(t)$. For the reconstruction we select the following parameters:

- $l = 2$,
- $m = \pm 2$,
- $n = [-10, 10]$.

Temporal part: It is not straightforward to represent a four dimensional quantity $\delta\rho_{\rm rec}(t, u, \theta, \phi)$ on paper, however you can see from Fig. 5.6c that the reconstructed density perturbation looks very similar to the filtered $h(t)$ (Fig. 5.6b), i.e. they both follow similar frequency and amplitude evolution over time. The amplitude and frequency of the reconstructed density perturbation $\delta\rho_{\rm rec}(t, u = 0.6, \theta = \pi/12, \phi = \pi/6)$ increases over time until the merger time similarly to $h(t)$. This is expected because $h(t) \propto \frac{{\rm d}^2}{{\rm d}t^2}\delta\rho(t, u, \theta, \phi)$ (Eq. (5.1)).

Angular part: Snapshots of the reconstructed BBH density perturbation show the angular change over time (Fig. 5.7). The angular change over time, i.e. spinning, is imprinted in the spherical harmonic modes $\{l, m\}$, and is reconstructed using our technique.

Radial part: Figure 5.7 shows how the angular part of the density perturbation $\delta\rho$ changes over time. If the source is merging as in the BBH merger case, Fig. 5.7 should show the inward motion over time, which it does not. It looks that our algorithm is not able to reconstruct the radial behaviour of the source. We discuss issues and possible solutions for the radial reconstruction in the following section.

5.4 Radial reconstruction

In this section we attempt to explain why the radial evolution cannot be reconstructed using our algorithm without additional assumptions on the source. To do that, we look in more detail how a function reconstruction is performed in our algorithm. We also show a purely analytical example of $\delta\rho_{\mathrm{rec}}(t, u, \theta, \phi)$ being identical for two very distinct cases: (1) radius changing over time, (2) radius constant over time.

5.4.1 Function reconstruction

Our technique reconstructs the density perturbation $\delta\rho_{\mathrm{rec}}(t, u, \theta, \phi)$ using mode decomposition:

$$\delta\rho(t, r, \theta, \phi) = \sum_{n} \sum_{lm} \delta\rho^{lmn}(t)\ F_n(r)\ Y_{lm}(\theta, \phi), \tag{5.27}$$

as given in Eq. (5.16). We have shown that Eq. (5.27) can be expressed as Eqs. (5.16) and (5.17)

$$\delta\rho(\tau, r, \theta, \phi) = K \times \left[\sum_{lmn} \mathcal{G}^{ij,\,lmn} F_n(r) Y_{lm}(\theta, \phi)\right] \times \left[\sum_{k} \tilde{h}_{ij,\,k} \frac{e^{-iw_k\tau}}{-w_k^2}\right] \tag{5.28}$$

$$= \text{constant} \times \text{purely spatial part} \times \text{purely temporal part.} \tag{5.29}$$

Eqs. 5.28 and 5.29 mean that any information for a specific mode, e.g. the $n = 1$ mode, must come from the emissivity $\mathcal{G}^{ij,\,lmn}$ factor, i.e. purely spatial part. Likewise all temporal information comes only from the factor $\tilde{h}_{ij,\,k}$, i.e. purely temporal part. In order to reconstruct a density perturbation change in radius over time, the radial modes n must have a different weighting factors over time.

Consider the following example. Suppose that the density perturbation is constant in radius at time $t = 0.2$. Then the only non-zero radial mode should be $n = 0$. If the density perturbation $\delta\rho$ is no longer constant in radius at time $t = 0.3$, then there should be other non-zero modes than $n = 0$. This information can be passed only in time (or frequency) dimension. However Eq. (5.28) shows that *all modes are equally weighted* by $\tilde{h}_{ij,\,k}$. This is the reason why it is not possible to reconstruct density perturbation $\delta\rho(t, r, \theta, \phi)$ change in radius over time.

We can actually go one step further and interpret Eq. (5.28) by saying that we essentially reconstruct the temporal evolution of the emissivity term $\mathcal{G}^{ij,\,lmn}$. The

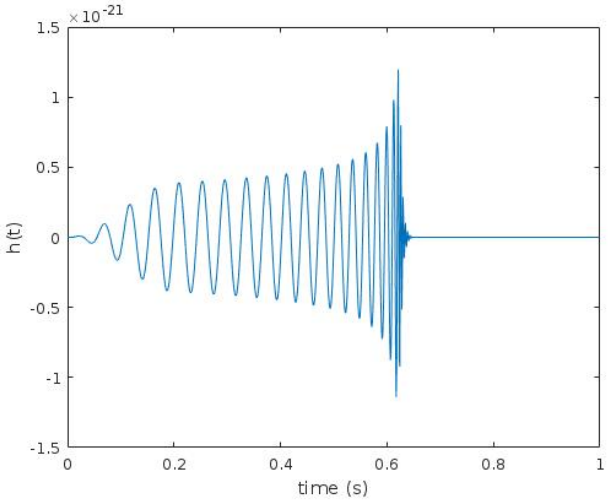

(5.6a) Numerical waveform $h(t)$ for a BBH merger GW150914. We tapered the start of the waveform so that both ends of the waveform would go smoothly to 0. Data taken from [111].

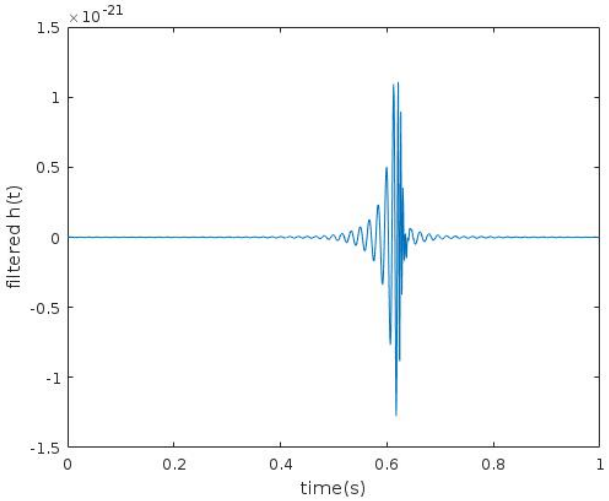

(5.6b) Filtered waveform from Fig. 5.6a with no contribution from frequencies below $f = 60\,\mathrm{Hz}$.

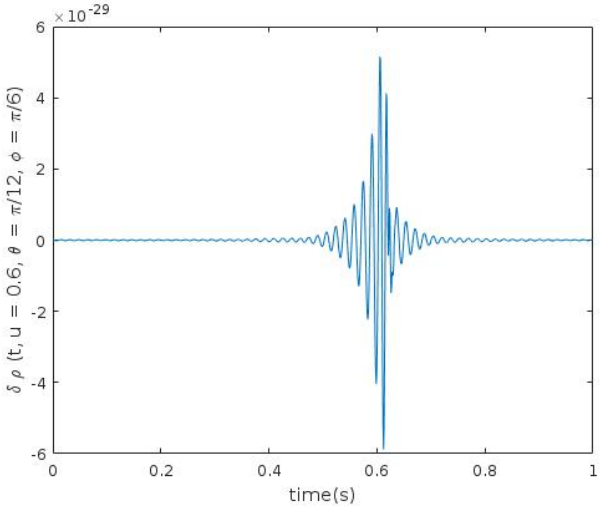

(5.6c) Reconstructed density perturbation $\delta\rho_{\mathrm{rec}}(t, u = 0.6, \theta = \pi/12, \phi = \pi/6)$. The amplitude and frequency gets higher over time similarly to the waveform (Fig. 5.6b) as expected.

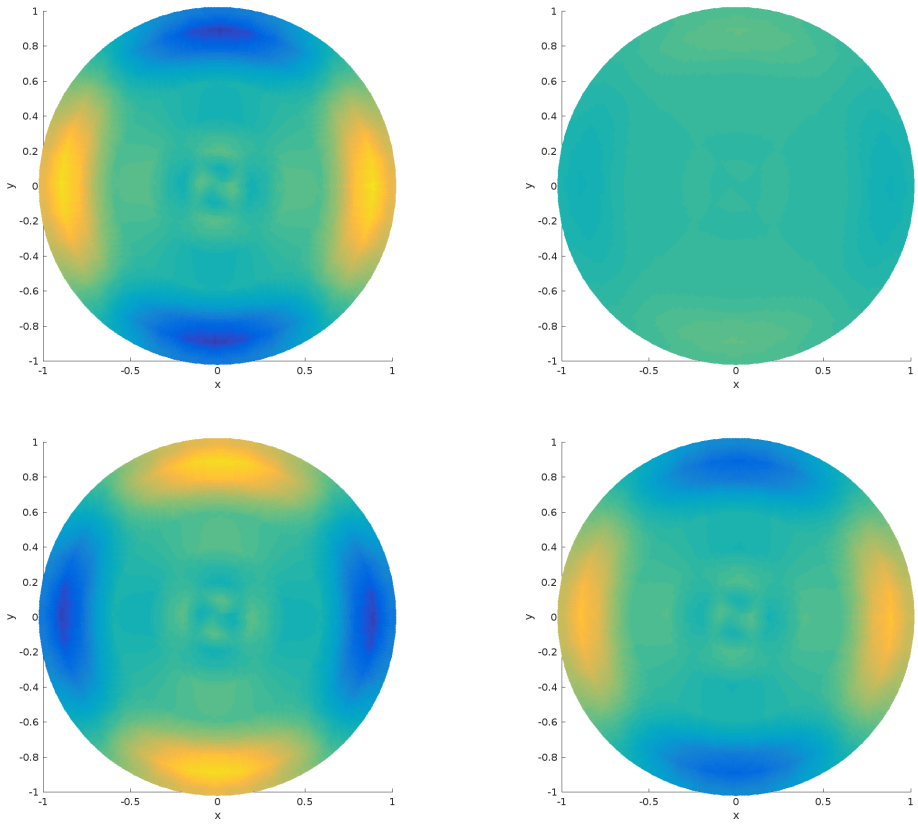

Figure 5.7: Snapshots of the reconstructed density perturbation $\delta\rho_{\mathrm{rec}}$ of a binary black hole merger in the $x-y$ plane at $\theta = \pi/2$ for times spaced by $\Delta t = 1/256\,\mathrm{s}$ starting from $t = 0.6055\,\mathrm{s}$. Snapshots are shown from top to bottom and from left to right order. These figures illustrate the fact that the source is a spinning quadrupole. However the radius is not changing.

emissivity term (discussed in §5.2) reconstructs the angular part correctly because it is non-zero only for $l = 2$, $m = \pm 2$ due to the quadrupole approximation, Eq. (5.1). For the radial part the emissivity term (Eq. (5.18)) is made out of the integral

$$\int_0^1 F_n(u)\,[\tilde{x}^i\tilde{x}^j - \frac{1}{3}\delta^{ij}u^2]\,u^2\mathrm{d}u \propto \int_0^1 F_n(u)\,u^4\mathrm{d}u, \tag{5.30}$$

which reconstructs $f(u) = u^4$.

We can see that our algorithm is doing exactly that, i.e. it reconstructs the function $f(u) = u^4$. Figure 5.8a shows the magnitude of the density perturbation $\delta\rho$ as a function of normalised radius u for all time instances. The blue line indicates $f(u) = u^4$ normalised to the maximum absolute value of $\delta\rho(t, u, \theta, \phi)$. The absolute value of the density perturbation $\delta\rho(t, u, \theta, \phi)$ changes over time because it is weighted by $\tilde{h}(w)$, nonetheless it clearly follows the u^4 function. Furthermore, Gibbs phenomena kinks can be seen in Fig. 5.8a. A separate plot (Fig. 5.8b) shows how the function $f(u) = u^4$ is reconstructed with Fourier modes (not by our algorithm). Using the same number of modes ($n = [-10, 10]$) for our algorithm (Fig. 5.8a) and an independent reconstruction (Fig. 5.8b), one can see that the reconstructed functions are identical. This proves the argument that our technique reconstructs the emisivity term G^{ij}_{lmn} evolving over time, hence the radius reconstruction is not possible without additional modifications or constraints.

5.4.2 Inability to infer (some) radius changes

Here we will show a purely analytical example of $\delta\rho_{\mathrm{rec}}(t, u, \theta, \phi)$ being degenerate for two very distinct radius change cases. Let us assume that the observer is on the z axis of a Cartesian coordinate system. Consider a source consisting of two point masses, each of mass M, moving symmetrically in the $x - z$ plane:

$$\begin{aligned}\rho(t, \vec{x}) = {} & M\delta(x - \xi(t))\delta(y)\delta(z - \zeta(t)) \\ & + M\delta(x + \xi(t))\delta(y)\delta(z + \zeta(t)).\end{aligned} \tag{5.31}$$

Substituting Eq. (5.31) into the quadrupole approximation Eq. (5.1) we get

$$h_{ij} = \frac{4M}{r}\frac{\mathrm{d}^2}{\mathrm{d}t^2}\begin{pmatrix} \xi^2 & 0 & \xi\zeta \\ 0 & 0 & 0 \\ \xi\zeta & 0 & \zeta^2 \end{pmatrix}. \tag{5.32}$$

The components seen by the observer are those after transverse projection, with

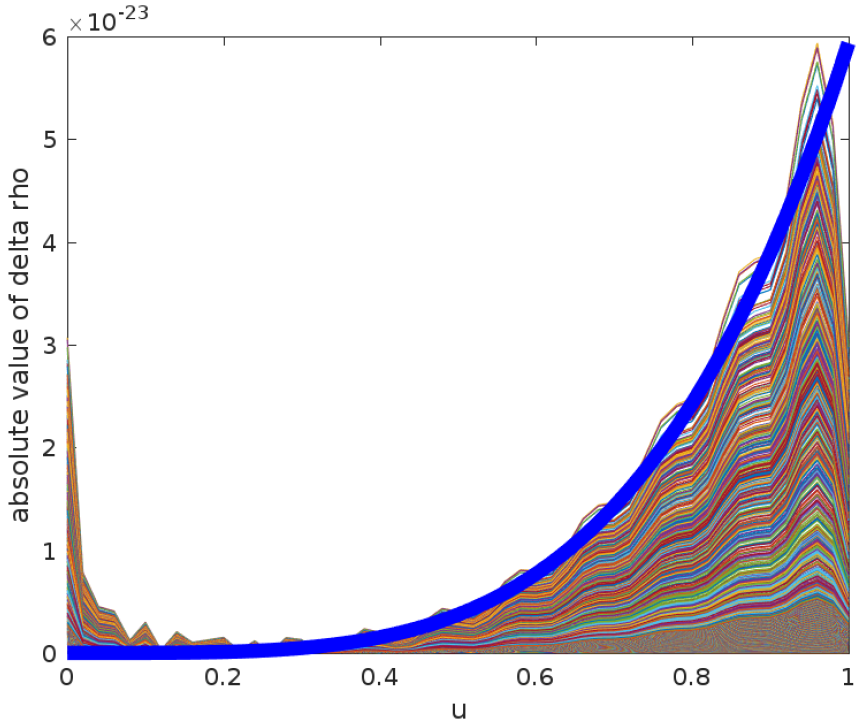

(5.8a) Absolute value of $\delta\rho(t, u, \theta = \pi/12, \phi = \pi/6)$ change in normalised radius u plotted for all instances of time. Fourier modes $n = [-10, 10]$ were used for the radial part reconstruction. The thick blue line shows the function $f(u) = u^4$ normalised to the maximum absolute value of $\delta\rho$.

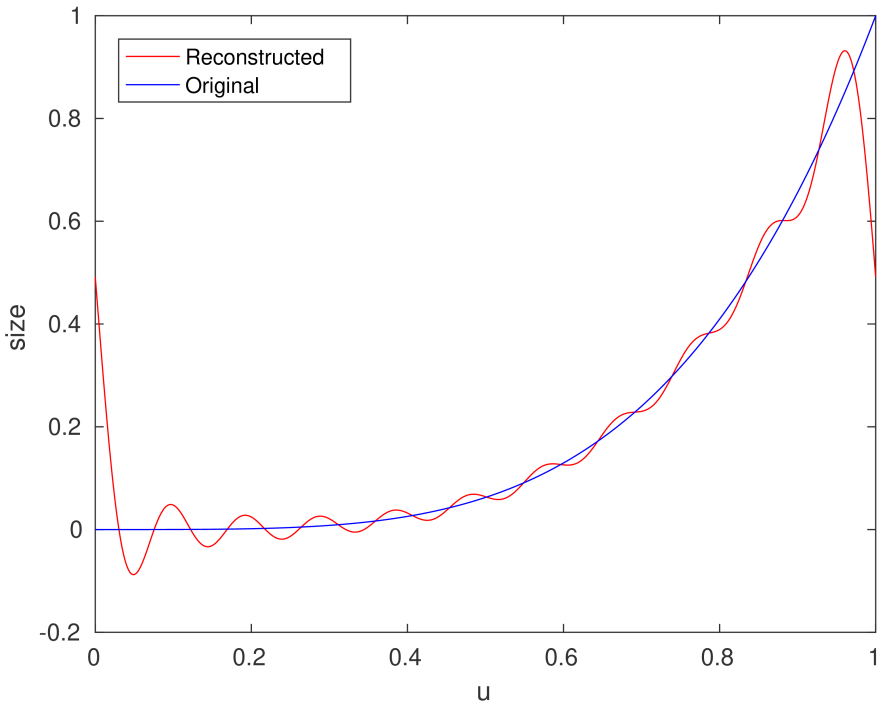

(5.8b) Function $f(u) = u^4$ (blue) reconstructed with Fourier modes $n = [-10, 10]$ (red). The reconstructed function has kinks at $u = 0, 1$ caused by Gibbs phenomena. Such kinks are also seen in Fig. 5.8a. The similarity of this plot to the plot showing $\delta\rho(t, r, \theta, \phi)$ reconstruction (above) suggests that the algorithm simply reconstructs $f(u) = u^4$ from the emissivity (Eq. (5.18)) rather than the actual radius evolution of the source.

operator $P = I - \hat{z} \otimes \hat{z}$, and removal of the trace:

$$h_{ij} \to (P^T h P)^{ij} - \frac{1}{2} tr\left(P^T h P\right) P^{ij} \tag{5.33}$$

$$= \frac{4M}{r}\frac{d^2}{dt^2}\left[\begin{pmatrix} \xi^2 & 0 & 0 \\ 0 & 0 & 0 \\ 0 & 0 & 0 \end{pmatrix} - \frac{1}{2}\xi^2 \begin{pmatrix} 1 & 0 & 0 \\ 0 & 1 & 0 \\ 0 & 0 & 0 \end{pmatrix}\right]$$

$$= \frac{2M}{r}\frac{d^2(\xi^2)}{dt^2}\begin{pmatrix} 1 & 0 & 0 \\ 0 & -1 & 0 \\ 0 & 0 & 0 \end{pmatrix}. \tag{5.34}$$

The observed polarisations are therefore

$$\begin{aligned} h_+ &= \frac{2M}{r}\frac{d^2(\xi^2)}{dt^2} \\ h_\times &= 0\,. \end{aligned} \tag{5.35}$$

This is independent of the z motion of the source (described by $\zeta(t)$). So for example, we get the same GW signal for these two cases:

Binary observed in orbital plane:

$$\xi(t) = R\cos(\Omega t)$$

$$\zeta(t) = R\sin(\Omega t)$$

In this case the radial size of the system is fixed.

'Cannonball' particles fired radially outward and falling back:

$$\xi(t) = R\cos(\Omega t)$$

$$\zeta(t) = 0$$

In this case the radial size of the system is changing over with time.

While these two cases have different radial evolution, they produce the same GW signature according to Eq. (5.35). Because they produce the same waveform $h(t)$, the reconstructed density perturbation $\delta\rho(t, r, \theta, \phi)$ would also be identical. This is an example of mathematical degeneracy when we attempt to reconstruct a four dimensional quantity $\delta\rho(t, r, \theta, \phi)$ from a one dimensional waveform $h(t)$.

5.5 Bayesian formulation

In order to reconstruct the density perturbation $\delta\rho(t, r, \theta, \phi)$, Eq. (5.10) needs to be inverted so that the coefficients c_{ij} can be found. Our original derivation inverts the

equation using the Moore-Penrose inverse, which is a best-fit method to solve a linear equation, and does not take into account possible dependencies, e.g. coefficient c_{ij} dependence on frequency. More importantly, we have shown in the previous section that we cannot reconstruct the radial part of the perturbation without additional information. We attempt to address these issues by deriving our algorithm in a Bayesian formulation.

Let us rewrite Eq. (5.10) as

$$\tilde{h}[k] = \begin{pmatrix} \tilde{h}_+[k] \\ \tilde{h}_\times[k] \end{pmatrix} = w\,\mathcal{H}\,\mathbf{c}_k\,, \tag{5.36}$$

where $w = \frac{2R^5}{DT^3}$, $\mathcal{H}$ is a matrix of dimensions $2 \times N_\alpha$ and $\mathbf{c}_k$ is a matrix of dimensions $N_\alpha \times 1$ (for each k).

Equation (5.36) gives the *true* GW signal as a function of the true mass density perturbation (expressed as a mode decomposition). The *measured* GW signal $\hat{h}$ will differ due to noise. The (unknown) error in $\hat{h}$ is

$$\Delta h = \tilde{h} - \hat{h} = -F_{MP}^{-1} n\,,$$

where $F_{MP}^{-1} = (F^T F)^{-1} F^T$ is the Moore-Penrose inverse of F and n is the vector of whitened detector noise values. This is the error for the simplest case of a maximum-likelihood reconstruction of h. We assume n to be unit-variance Gaussian, in which case Δh will be Gaussian with covariance matrix

$$\Sigma = \langle \Delta h\, \Delta h^T \rangle = (F^T F)^{-1}\,.$$

Bayes's theorem then tells us that the probability of the source being described by particular decomposition coefficients $\mathbf{c}$ given a measured GW signal $\hat{h}$ is

$$\begin{aligned} p(\mathbf{c}|\hat{h}) &= \frac{p(\hat{h}|\mathbf{c})p(\mathbf{c})}{p(\hat{h})} && (5.37)\\ &= \frac{p(\Delta h = \tilde{h} - \hat{h}|\mathbf{c})p(\mathbf{c})}{p(\hat{h})} && (5.38)\\ &= \exp\left\{-\frac{1}{2}(\tilde{h} - \hat{h})^T \Sigma^{-1} (\tilde{h} - \hat{h})\right\} \times \frac{p(\mathbf{c})}{p(\hat{h})} && (5.39)\\ &= \exp\left\{-\frac{1}{2}(w\,\mathcal{H}\,\mathbf{c}_k - \hat{h})^T F^T F (w\,\mathcal{H}\,\mathbf{c}_k - \hat{h})\right\} \times \frac{p(\mathbf{c})}{p(\hat{h})}\,. && (5.40) \end{aligned}$$

Uniform prior: Let us consider the case where the prior $p(\mathbf{c})$ is uniform (independent of $\mathbf{c}$). Then the log-probability is

$$\Lambda \equiv \ln p(\mathbf{c}|\hat{h}) = -\frac{1}{2}(w\,\mathcal{H}\,\mathbf{c}_k - \hat{h})^T F^T F (w\,\mathcal{H}\,\mathbf{c}_k - \hat{h}) \quad + \text{ terms independent of } \mathbf{c}\,.$$

The probability is maximised for the coefficients $\hat{\mathbf{c}}$ such that

$$\left.\frac{d\Lambda}{d\mathbf{c}^T}\right|_{\mathbf{c}=\hat{\mathbf{c}}} = 0\,.$$

The solution is

$$\begin{aligned}\hat{\mathbf{c}}_k &= w^{-1}(\mathcal{H}^T F^T F \mathcal{H})^{-1}\mathcal{H}^T F^T F \hat{h} && (5.41)\\ &= w^{-1}(F\mathcal{H})^{-1}_{MP} F\hat{h}\,, && (5.42)\end{aligned}$$

where $(F\mathcal{H})^{-1}_{MP}$ is the Moore-Penrose inverse of the $N_D \times N_\alpha$ matrix $F\mathcal{H}$. This gives the maximum-likelihood estimate $\hat{\mathbf{c}}$ of the source density perturbation as a function of the maximum-likelihood estimate $\hat{h}$ of the GW signal. Comparing Eq. (5.42) with the original Eq. (5.11), we see the advantages of a Bayesian derivation: it shows how to account for both polarisations self-consistently (remember the argument made for Eq. (5.11) that the solution for c depends on the projection ij), and also includes uncertainties in the reconstructed GW signal due to the background noise and antenna patterns of the detectors. The weighting of the two polarisations follows expectations: the $\mathcal{H}$ factor weights by the efficiency with which the mode emits each polarisation, while the $F^T F$ factor weights each polarisation by the detector's expected SNR^2 (squared antenna response divided by the noise power spectrum).

Since the maximum-likelihood estimate $\hat{h}$ of the GW signal will be contaminated by noise, so too will $\hat{\mathbf{c}}$. The (unknown) error will be

$$\begin{aligned}\Delta\mathbf{c}_k &= \mathbf{c} - \hat{\mathbf{c}} && (5.43)\\ &= w^{-1}(F\mathcal{H})^{-1}_{MP} F\Delta h\,, && (5.44)\end{aligned}$$

which gives the covariance matrix for the $\hat{\mathbf{c}}$ as

$$\begin{aligned}\langle \Delta\mathbf{c}\,\Delta\mathbf{c}^T\rangle &= w^{-2}(F\mathcal{H})^{-1}_{MP} F\langle\Delta h\Delta h^T\rangle F^T (F\mathcal{H})^{-1T}_{MP} && (5.45)\\ &= w^{-2}(F\mathcal{H})^{-1}_{MP} F(F^T F)^{-1} F^T (F\mathcal{H})^{-1T}_{MP} && (5.46)\\ &= w^{-2}(\mathcal{H}^T F^T F\mathcal{H})^{-1}\,. && (5.47)\end{aligned}$$

In this section we derived the term $\mathbf{c}_k$ (Eq. (5.42)) with error $\Delta\mathbf{c}_k$ (Eq. (5.44)) for uniform prior in $p(\mathbf{c})$ using Bayes theorem. Equation (5.44) is more general than the derivation using the frequentist inference (Eq. (5.11)) because Eq. (5.44) naturally combines both GW polarisations and accounts for the uncertainties due to noise. For a simplified case when there is only one polarisation and no noise, Eq. (5.44) is identical to Eq. (5.11); this is expected because uniform prior in $p(\mathbf{c})$ corresponds to the maximum likelihood value.

We already used priors in our frequentist-approach analysis when we filtered data to remove the low frequency content (see §5.3.1). Without it the algorithm would

not have worked for any signal that contains some noise. The Bayesian formalism provides us a systematic way to incorporate prior information. Adding constraints such as energy and momentum conservation could reduce the degeneracy between $\delta\rho(t, r, \theta, \phi)$ and $h(t)$.

5.6 Discussion

We have derived an algorithm that reconstructs a density perturbation $\delta\rho(t, u, \theta, \phi)$ of a source consistent with the GW signal $h(t)$ using mode decomposition. There is an unknown overall scaling constant $2R^5/DT^3$ where R is the maximum radius of the source, T is the duration of the GW emission, and D is the distance to the source. While it is relatively easy to put a limit on the duration of the GW emission (it is just the duration of the reconstructed waveform), limits on R and D strongly depend on the source type. Becsy et al. (2020) [52] reports that limits on the maximum radius of the source R and distance to the source D can be constrained to several order of magnitudes for BBH systems, however these estimates become more uncertain for the burst-type sources.

Furthermore, the algorithm reconstructs the density *perturbation* (i.e. quadrupolar contribution) (Eq. (5.3)), not the density itself that is made of monopole, dipole and all other higher order terms. Many GW burst sources are expected to emit relatively small amounts of energy in GWs (e.g. $10^{-8}M_{\odot}c^2$ for SN explosions) compared to CBC sources, mostly because many GW burst sources are nearly spherically symmetric. This means that our technique would reconstruct only a minor part of the whole density (Eq. (5.2)). Yet reconstructing the density perturbation, the component that produced the GWs, could be crucial to understand the physics of the source in the abscence of GW models.

The solution depends on basis functions and modes we choose to reconstruct, therefore it is important to understand how basis functions are implemented. An 'unnatural' choice of basis function would require many modes to be used for the reconstruction which could be a problem if the SNR of a signal is low. We discussed this in more detail in §5.2 where we argued that spherical harmonics $Y_{l,m}(\theta, \phi)$ as a choice for the angular reconstruction works well because the only non-zero modes for the quadrupole approximation (Eq. (5.1)) are $l = 2$, $m \pm 2$.

We have tested the algorithm with several simple test cases. Firstly, we tested how well the algorithm reconstructs a spinning quadrupole source that could be described by a single radial mode (Eq. (5.20)). We found that in case when there is no noise, the perturbation is reconstructed ideally, i.e. match $M = 1$ (§5.3.1). For Gaussian noise we find the match between reconstructed and original density perturbations to be $M = 0.9\,(0.5)$ for SNR $\approx 130\,(35)$, see Fig. 5.5. We also noticed that the algorithm is susceptible to noise: adding even extremely small noise to the signal the match becomes unreasonably small, e.g. $M = 0.02$ for SNR ≈ 2000. This

happens because we invert $\frac{d^2}{dt^2}$ term from Eq. (5.1) by double time integral resulting in the factor $\frac{1}{-w_k^2}$ (Eq. (5.16)). We show that we can overcome this problem by bandpassing the data with a filter that zeroes the data for $|w| < 120\,\mathrm{rads}^{-1}$ for the spinning quadrupole case.

We also tested the algorithm with a merger of two black holes. Using bandpassed numerical waveform as the input, we show that the algorithm is able to reconstruct temporal and angular parts of the density perturbation. However, our method is not able to reconstruct how density perturbation $\delta\rho(t, r, \theta, \phi)$ changes in radius over time. We provide an explanation as to why this happens in §5.4.1 where we argue that the algorithm essentially reconstructs temporal evolution of the emissivity G^{ij}_{lmn}. This works well for the angular part because the quadrupole approximation (Eq. (5.1) allows only the $l = 2$, $m \pm 2$ spherical harmonics to radiate GWs. The quadrupole approximation does not constrain the radial part in such a way, therefore the radial part of the density perturbation cannot be reconstructed using our method.

The inability to reconstruct the radial part is related to probably one of the biggest limitations of the method: it attempts to reconstruct a four dimensional quantity, $\delta\rho(t, r, \theta, \phi)$, from a one dimensional waveform, $h(t)$. Such a reconstruction is going to be highly degenerate; i.e. multiple $\delta\rho(t, r, \theta, \phi)$ can map into one $h(t)$. As a result, it will commonly be the case that we cannot reconstruct the correct $\delta\rho(t, r, \theta, \phi)$ because it is degenerate with another density perturbation. Indeed, we show a simple example of this degeneracy by considering two completely diferent cases: (1) a binary observed in the orbital plane where the radial size of the system is fixed and (2) 'cannonball' particles fired linearly outward and falling back (§5.4.2). Both of these cases provide identical $h(t)$, hence the reconstructed density perturbation must be identical.

The most systematic way to include prior knowledge, either for solving degenerate cases or for dealing with noisy data, is to use a Bayesian formalism. We showed in Ch. 5.5 that c_k^{lmn} from Eq. (5.11) is just the limiting case when the prior on $p(\mathbf{c})$ is uniform (Eq. (5.42)). However a uniform prior on $p(\mathbf{c})$ allows the mode amplitudes in the reconstruction to be arbitrarily large, therefore a more constrained prior would be better. Another prior that is commonly used in Bayesian analysis is the Gaussian prior, $\exp(-c^2/2\sigma^2)$, which would tend to constrain mode amplitudes to magnitudes of some characteristic size σ. The derived Bayesian formalism also allows to combine information from both GW polarisations, and accounts for the antenna response.

For future development it would be beneficial to look at how specific physical information could be included as priors in the Bayesian formalism of the algorithm. It remains to be determined to what extent, additional constraints (e.g. conservation of energy, expected frequency range, etc.) could disentangle the mathematical degeneracy between different cases.

It would be also beneficial to look at other choices of modes for radius reconstruc-

tion. We already mentioned that the angular evolution of the density perturbation $\delta\rho(t, u, \theta, \phi)$ can be reconstructed because the quadrupole equation (Eq. (5.1)) limits spherical harmonics to only $l = 2, m \pm 2$ modes. Perhaps there is a more 'natural' choice of modes for radius reconstruction of GW sources other than Fourier modes, and there would be a limited number of relevant modes, similarly to spherical harmonics.

Finally, it could be worth going further than the quadrupole approximation. Currently we assume that the source is emitting only quadrupolar GWs which is a good approximation to the first order. Higher order moments (e.g. octupole radiation) would allow to reconstruct sources that have a more complicated profile than the one described only by the quadrupole moment. It could even potentially allow to break some degeneracy and reconstruct the radial part of the perturbation. However it is worth noting that the higher order radiation such as octupole is expected to be much weaker than the quadrupole radiation, hence only *very* strong signals would benefit from this extension.

Postface

In this chapter we presented a novel method to interpret unmodelled GW signals, specifically to reconstruct the density perturbation $\delta\rho(t, r, \theta, \phi)$ of a source from the GW signal $h(t)$. We derived the algorithm in §5.2 with a special focus on emissivity $G_{ij,lmn}$ (§5.2). We found that density perturbation for the 220 source is reconstructed with match $M = 1$ when there is no noise (§5.3.1). For the 220 source with Gaussian noise density perturbation $\delta\rho(t, r, \theta, \phi)$ is reconstructed with $M = 0.9\,(0.5)$ for SNR $\approx 130\,(35)$ (§5.3.1). For a binary black hole merger we are able to reconstruct the temporal and angular parts of the perturbation but not the radial part (§5.3.2). In §5.4 we provided an explanation as to why the radial part cannot be reconstructed with our method and provided an example of a mathematical degeneracy between $\delta\rho(t, r, \theta, \phi)$ and $h(t)$. We also introduced Bayesian formalism by deriving one of the key equations of the algorithm (§5.5). Finally, we ended the chapter by discussion and future work on the method (§5.6).

Chapter 6

Concluding remarks

We used Einstein field equations to prove the existence of gravitational waves, 'ripples' of a spacetime traveling at the speed of light, c. We presented the four main categories of GW sources, and briefly mentioned the first detection of gravitational waves, GW150914. We also explained how GW detectors – interefometers – work, and their antenna pattern which is different from electromagnetic telescopes. The summary of the most recent LIGO–Virgo observing runs indicates that detectors continue to increase their sensitivity which leads to more detections and, more importantly, more varied detections. During the first observing run there were 3 BBH detections, during the second one LIGO–Virgo observed 7 BBH and 1 BNS, while the third observing run had 56 candidate events of which only 38 were binary black holes.

Given that GW detectors are becoming more sensitive and they start observing not only well modelled and strong BBH signals, we could expect to detect an unmodelled GW burst. We reviewed the most promising sources of GW bursts such as gamma-ray bursts, supernovae, isolated neutron stars and fast radio bursts. A special attention was given to short GRB–compact binary coalescence and long GRB–supernova sources because these are well linked phenomena. We argued that the observation of a GW burst (especially with an electromagnetic counterpart) could be extremely rewarding for fundamental physics, for example the equation of state of a neutron star or the mechanism of a core-collapse supernova. We showed that a detection of a GW burst can be expected with either current generation detectors (Advanced LIGO and Virgo) or with the third generation interferometers such as Einstein Telescope, depending on the amount of energy emitted via GWs.

Due to unknown (or very computationally intensive) physics GW bursts do not have reliable GW models, therefore a coherent search pipeline is necessary. We introduced X-Pipeline, an analysis package used for GW burst searches, its theoretical framework and its practical application for searches for GWs associated with GRBs. Over the last two LIGO–Virgo observing runs (2 and 3a), X-Pipeline analysed 202 GRBs in total and found one confident detection, GRB 170817A – GW170817, with

4.2σ significance. For other GRBs we estimated exclusion distances that can be used for population studies. Using a subset of short GRBs from LIGO–Virgo observing run 2 that were followed-up separately with a matched filtering search PyGRB, we were able to make a prediction on future rates of joint short GRB–CBC detections.

After we showed how unmodelled GW bursts can be detected using X-Pipeline, the next step is to ask how well can we reconstruct parameters of a GW burst. Our study investigated BayesWave, a Bayesian parameter estimation algorithm, in three key areas: sky localisation accuracy, signal/noise discrimination and waveform reconstruction accuracy. To do that we injected simulated BBH signals into LIGO–Virgo data and recovered them with BayesWave. We then compared recovered parameters not only to the injected ones but also to the first-principle estimates, which in turn allows to see if the pipeline performs optimally, or is there a room for improvement. We found that BayesWave's effectiveness depends mainly on the the time-frequency content of the signal: the fewer wavelets needed to reconstruct a signal, the better the performance. For example, BayesWave is able to localise gravitational-wave sources as well as a template analysis for signals that require $\lesssim 10$ wavelets. The study also demonstrated that BBH waveforms can be reconstructed with up to the match $M \sim 0.95$ for signals that require small time-frequency volume (i.e. high-mass systems). We could expect a similarly high match reconstruction of GW burst waveforms because such signals also occupy a relatively small time-frequency volume.

For unmodelled GW signals that the waveform $h(t)$ can be reconstructed, we presented a novel method to reconstruct the source density perturbations $\delta\rho(t, r, \theta, \phi)$. We derived an algorithm that decomposes a density perturbation into modes which then allows to invert the quadrupole equation. We found that density perturbations of the source can be reconstructed from the GW signal $h(t)$ in principle by testing a spinning quadrupole source with no radius evolution. In such case we get the match $M = 1$ between the reconstructed and original density perturbations. For Gaussian noise we find $M = 0.9\,(0.5)$ for SNR $= 135\,(35)$. We also tested the algorithm with a BBH merger where we investigated each dimension reconstruction separately. The algorithm reconstructs temporal and angular parts quite well, however the radial evolution is not reconstructed, i.e. the binary spins but does not merge. We explain that this is caused by the algorithm reconstructing the emissivity integral G^{ij}_{lmn} which does contain information about the radius change over time. We also show an analytical example where two distinct cases of different radial evolution produce the same gravitational waveform $h(t)$. This is an example of the biggest limitation of the algorithm: a mathematical degeneracy when we attempt to reconstruct a four dimensional mass density perturbation $\delta\rho(t, r, \theta, \phi)$ from a one dimensional waveform $h(t)$. It should be possible to resolve this limitation in some cases by including additional constraints. A systematic approach to incorporate prior information is by using a Bayesian formalism. We derived the equation for mode coefficients c^{lmn}_{k}

using Bayes theorem which not only shows how to account for both polarisations self-consistenly but also includes uncertainties from the reconstructed GW signal.

Bibliography

[1] *2704 BATSE Gamma-Ray Bursts*, (accessed February 27, 2020). `https://heasarc.gsfc.nasa.gov/docs/cgro/batse/`.

[2] *BeppoSAX instrument description*, (accessed February 27, 2020). `https://heasarc.gsfc.nasa.gov/docs/sax/sax.html`.

[3] *FRB online catalogue*, (accessed February 27, 2020). `http://frbcat.org/`.

[4] *GCN 289: measured flux for GRB 970228*, (accessed February 27, 2020). `https://gcn.gsfc.nasa.gov/gcn3/289.gcn3`.

[5] A. de Ugarte Postigo et al. Searching for differences inswift's intermediate grbs. *Astronomy and Astrophysics*, 525:A109, Dec 2010.

[6] A. Harrison et al. Optical and radio observations of the afterglow from GRB 990510: Evidence for a jet. *The Astrophysical Journal*, 523(2):L121–L124, Oct 1999.

[7] A. Riess et al. A 2.4% determination of the local value of the Hubble constant. *ApJ*, 826(1):56, July 2016.

[8] J. Aasi et al. Directed search for gravitational waves from Scorpius X-1 with initial LIGO data. *Phys. Rev.*, D91(6):062008, 2015.

[9] B. Abbott, R. Abbott, T. Abbott, F. Acernese, K. Ackley, C. Adams, T. Adams, P. Addesso, R. Adhikari, V. Adya, and et al. Constraints on cosmic strings using data from the first advanced ligo observing run. *Physical Review D*, 97(10), May 2018.

[10] B. P. Abbott et al. Implementation and testing of the first prompt search for gravitational wave transients with electromagnetic counterparts. *Astron. Astrophys.*, 539:A124, 2012.

[11] B. P. Abbott et al. Characterization of transient noise in Advanced LIGO relevant to gravitational wave signal GW150914. *Class. Quant. Grav.*, 33(13):134001, 2016.

[12] B. P. Abbott et al. GW150914: Implications for the stochastic gravitational wave background from binary black holes. *Phys. Rev. Lett.*, 116(13):131102, 2016.

[13] B. P. Abbott et al. Observing gravitational-wave transient GW150914 with minimal assumptions. *Phys. Rev.*, D93(12):122004, 2016. [Addendum: Phys. Rev. D94, 069903 (2016)].

[14] B. P. Abbott et al. Estimating the contribution of dynamical ejecta in the kilonova associated with GW170817. *Astrophys. J.*, 850(2):L39, 2017.

[15] B. P. Abbott et al. GW170817: Observation of gravitational waves from a binary neutron star inspiral. *Phys. Rev. Lett.*, 119(16):161101, 2017.

[16] B. P. Abbott et al. Search for post-merger gravitational waves from the remnant of the binary neutron star merger GW170817. *Astrophys. J.*, 851(1):L16, 2017.

[17] B. P. Abbott et al. Prospects for observing and localizing gravitational-wave transients with Advanced LIGO, Advanced Virgo and KAGRA. *Living Rev. Rel.*, 21(1):3, 2018.

[18] B. P. Abbott et al. Search for transient gravitational-wave signals associated with magnetar bursts during Advanced LIGO's second observing run. *Astrophys. J.*, 874(2):163, 2019.

[19] Abbott, B. P. et al. GWTC-1: A gravitational-wave transient catalog of compact binary mergers observed by LIGO and Virgo during the first and second observing runs. *Phys. Rev. X*, 9:031040, Sep 2019.

[20] E. Abdikamalov, S. Gossan, A. M. DeMaio, and C. D. Ott. Measuring the angular momentum distribution in core-collapse supernova progenitors with gravitational waves. *Physical Review D*, 90(4), Aug 2014.

[21] P. Ajith et al. Inspiral-merger-ringdown waveforms for black-hole binaries with non-precessing spins. *Phys. Rev. Lett.*, 106:241101, 2011.

[22] N. Andersson and G. L. Comer. Probing neutron-star superfluidity with gravitational-wave data. *Physical Review Letters*, 87(24), Nov 2001.

[23] N. Andersson and K. D. Kokkotas. Towards gravitational wave asteroseismology. *Monthly Notices of the Royal Astronomical Society*, 299(4):1059–1068, Oct 1998.

[24] B. Becsy et al. Parameter estimation for gravitational-wave bursts with the BayesWave pipeline. *Astrophys. J.*, 839(1):15, 2017.

[25] B. P. Abbott et al. Search for gravitational wave radiation associated with the pulsating tail of the SGR 1806-20 hyperflare of 27 December 2004 using LIGO. *Phys. Rev. D*, 76(6):062003, Sept. 2007.

[26] B. P. Abbott et al. Search for Gravitational-Wave Bursts from Soft Gamma Repeaters. *Phys. Rev. Letters*, 101(21):211102, Nov. 2008.

[27] B. P. Abbott et al. Binary black hole mergers in the first Advanced LIGO observing run. *Physical Review X*, 6(4):041015, Oct. 2016.

[28] B. P. Abbott et al. GW151226: Observation of gravitational waves from a 22-Solar-mass binary black hole coalescence. *Phys. Rev. Lett.*, 116:241103, Jun 2016.

[29] B. P. Abbott et al. Upper limits on the rates of binary neutron star and neutron star-black hole mergers from advanced LIGO's first observing run. *ApJ Letters*, 832(2):L21, Dec. 2016.

[30] B. P. Abbott et al. A gravitational-wave standard siren measurement of the Hubble constant. *Nature*, 551(7678):85–88, Nov. 2017.

[31] B. P. Abbott et al. Exploring the sensitivity of next generation gravitational wave detectors. *Classical and Quantum Gravity*, 34(4):044001, Jan 2017.

[32] B. P. Abbott et al. Gravitational waves and gamma-rays from a binary neutron star merger: GW170817 and GRB 170817A. *The Astrophysical Journal*, 848(2):L13, Oct 2017.

[33] B. P. Abbott et al. Multi-messenger observations of a binary neutron star merger. *The Astrophysical Journal*, 848(2):L12, Oct 2017.

[34] B. P. Abbott et al. First measurement of the Hubble constant from a dark standard siren using the Dark Energy Survey galaxies and the LIGO/Virgo binary-black-hole merger GW170814. *ApJ Letters*, 876(1):L7, May 2019.

[35] B. P. Abbott et al. Search for the isotropic stochastic background using data from advanced ligo's second observing run. *Physical Review D*, 100(6), Sep 2019.

[36] B. Swinkels. *aLOG:37972*, (accessed February 27, 2020). `https://logbook.virgo-gw.eu/virgo/?r=37972`.

[37] S. A. Balbus and J. F. Hawley. Instability, turbulence, and enhanced transport in accretion disks. *Rev. Mod. Phys.*, 70:1–53, Jan 1998.

[38] C. P. L. Berry et al. Parameter estimation for binary neutron-star coalescences with realistic noise during the Advanced LIGO era. *Astrophys. J.*, 804(2):114, 2015.

[39] N. T. Bishop and L. Rezzolla. Extraction of gravitational waves in numerical relativity. *Living Reviews in Relativity*, 19(1), Oct 2016.

[40] L. Blanchet. Gravitational radiation from post-Newtonian sources and inspiralling compact binaries. *Living Rev. Rel.*, 9:4, 2006.

[41] J. S. Bloom. *What are gamma-ray bursts?*, page 66. Princeton University Press, 2011.

[42] C. Bond, D. Brown, A. Freise, and K. A. Strain. Interferometer techniques for gravitational-wave detection. *Living Reviews in Relativity*, 19(1):1, Dec. 2016.

[43] S. Boran, S. Desai, E. Kahya, and R. Woodard. GW170817 falsifies dark matter emulators. *Physical Review D*, 97(4), Feb 2018.

[44] B.P. Abbott et al. Search for gravitational waves associated with the gamma ray burst GRB 030329 using the LIGO detectors. *Physical Review D*, 72(4), Aug 2005.

[45] B.P. Abbott et al. Observation of gravitational waves from a binary black hole merger. *Phys. Rev. Lett.*, 116(6):061102, 2016.

[46] B.P. Abbott et al. Search for gravitational waves associated with gamma-ray bursts during the first advanced LIGO observing run and implications for the origin of GRB 150906B. *The Astrophysical Journal*, 841(2):89, May 2017.

[47] B.P. Abbott et al. All-sky search for long-duration gravitational wave transients in the first advanced LIGO observing run. *Classical and Quantum Gravity*, 35(6):065009, Feb 2018.

[48] B.P. Abbott et al. All-sky search for continuous gravitational waves from isolated neutron stars using advanced LIGO O2 data. *Phys. Rev. D*, 100:024004, Jul 2019.

[49] B.P. Abbott et al. Search for gravitational-wave signals associated with gamma-ray bursts during the second observing run of advanced LIGO and advanced Virgo. *The Astrophysical Journal*, 886(1):75, Nov 2019.

[50] B.P. Abbott et al. An optically targeted search for gravitational waves emitted by core-collapse supernovae during the first and second observing runs of advanced LIGO and advanced Virgo. *Physical Review D*, 101(8), Apr 2020.

[51] G. E. Brown and C.-H. Lee. The case for Case C mass transfer in the galactic evolution of black hole binaries. *New Astronomy*, 9(3):225–237, Mar. 2004.

[52] B. Bécsy, P. Raffai, K. Gill, T. B. Littenberg, M. Millhouse, and M. J. Szczepańczyk. Interpreting gravitational-wave burst detections: constraining source properties without astrophysical models. *Classical and Quantum Gravity*, 37(10):105011, Apr 2020.

[53] K. Cannon et al. Toward early-warning detection of gravitational waves from compact binary coalescence. *Astrophys. J.*, 748:136, 2012.

[54] S. M. Carroll. *Spacetime and geometry: an introduction to general relativity*. Cambridge University Press, 2019.

[55] R. Chapman, N. R. Tanvir, R. S. Priddey, and A. J. Levan. How common are long gamma-ray bursts in the local Universe? *Monthly Notices of the Royal Astronomical Society: Letters*, 382(1):L21–L25, 11 2007.

[56] H.-Y. Chen, M. Fishbach, and D. E. Holz. A two per cent Hubble constant measurement from standard sirens within five years. *Nature*, 562(7728):545–547, Oct. 2018.

[57] CHIME/FRB collaboration. *A bright millisecond-timescale radio burst from the direction of the Galactic magnetar SGR 1935+2154*, (accessed June 25, 2020). `http://www.astronomerstelegram.org/?read=13681`.

[58] J. Clark, H. Evans, S. Fairhurst, I. W. Harry, E. Macdonald, D. Macleod, P. J. Sutton, and A. R. Williamson. Prospects for joint gravitational wave and short gamma-ray burst observations. *ApJ*, 809(1):53, Aug. 2015.

[59] J. M. Cordes and S. Chatterjee. Fast radio bursts: an extragalactic enigma. *Annual Review of Astronomy and Astrophysics*, 57:417–465, Aug. 2019.

[60] N. J. Cornish and T. B. Littenberg. Bayeswave: Bayesian inference for gravitational wave bursts and instrument glitches. *Classical and Quantum Gravity*, 32(13):135012, Jun 2015.

[61] A. Corsi and B. J. Owen. Maximum gravitational-wave energy emissible in magnetar flares. *Phys. Rev. D*, 83(10):104014, May 2011.

[62] M. B. Davies, A. King, S. Rosswog, and G. Wynn. Gamma-ray bursts, supernova kicks, and gravitational radiation. *The Astrophysical Journal*, 579(2):L63–L66, Nov 2002.

[63] V. Decoene, C. Guépin, K. Fang, K. Kotera, and B. D. Metzger. High-energy neutrinos from fallback accretion of binary neutron star merger remnants. 2019.

[64] Derek Davis et al. Improving the sensitivity of advanced LIGO using noise subtraction. *Classical and Quantum Gravity*, 36(5):055011, Feb 2019.

[65] E. Dimastrogiovanni, M. Fasiello, and T. Fujita. Primordial gravitational waves from axion-gauge fields dynamics. *JCAP*, 1701(01):019, 2017.

[66] M. Dominik, E. Berti, R. O'Shaughnessy, I. Mandel, K. Belczynski, C. Fryer, D. E. Holz, T. Bulik, and F. Pannarale. Double compact objects III: Gravitational wave detection rates. *Astrophys. J.*, 806(2):263, 2015.

[67] E. J. Daw et al. Long-term study of the seismic environment at LIGO. *Classical and Quantum Gravity*, 21(9):2255–2273, Apr 2004.

[68] D. Eichler, M. Livio, T. Piran, and D. N. Schramm. Nucleosynthesis, neutrino bursts and γ-rays from coalescing neutron stars. *Nature*, 340(6229):126–128, July 1989.

[69] A. Einstein. The field equations of gravitation. *Proceedings of Prussian Academy of Sciences*, page 844, 1915.

[70] A. Einstein. Approximative integration of the field equations of gravitation. *Proceedings of Prussian Academy of Sciences*, page 688, 1916.

[71] R. Essick, S. Vitale, E. Katsavounidis, G. Vedovato, and S. Klimenko. Localization of short duration gravitational-wave transients with the early advanced LIGO and Virgo detectors. *Astrophys. J.*, 800(2):81, 2015.

[72] E. C. et al. Enhancing gravitational-wave science with machine learning, 2020.

[73] R. A. et al.". GWTC-2: Compact binary coalescences observed by LIGO and Virgo during the first half of the third observing run. 2020.

[74] R. A. et al.". Search for gravitational waves associated with gamma-ray bursts detected by Fermi and Swift during the LIGO-Virgo run O3a. 2020.

[75] S. Fairhurst. Triangulation of gravitational wave sources with a network of detectors. *New J. Phys.*, 11:123006, 2009. [Erratum: New J. Phys. 13, 069602 (2011)].

[76] S. Fairhurst. Source localization with an advanced gravitational wave detector network. *Class. Quant. Grav.*, 28:105021, 2011.

[77] S. Fairhurst. Improved source localization with LIGO India. *J. Phys. Conf. Ser.*, 484:012007, 2014.

[78] S. Fairhurst. Localization of transient gravitational wave sources: beyond triangulation. *Classical and Quantum Gravity*, 35(10):105002, May 2018.

[79] A. Feo, R. D. Pietri, F. Maione, and F. Löffler. Modeling mergers of known galactic systems of binary neutron stars. *Classical and Quantum Gravity*, 34(3):034001, Dec 2016.

[80] F. Foucart, T. Hinderer, and S. Nissanke. Remnant baryon mass in neutron star-black hole mergers: Predictions for binary neutron star mimickers and rapidly spinning black holes. *Phys. Rev.*, D98(8):081501, 2018.

[81] W. L. Freedman. Correction: Cosmology at a crossroads. *Nature Astronomy*, 1:0169, June 2017.

[82] A. Goldstein, V. Connaughton, M. S. Briggs, and E. Burns. Estimating long GRB jet opening angles and rest-frame energetics. *Astrophys. J.*, 818(1):18, 2016.

[83] J. H. Groh, C. Georgy, and S. Ekström. Progenitors of supernova Ibc: a single Wolf-Rayet star as the possible progenitor of the SN Ib iPTF13bvn. *Astronomy and Astrophysics*, 558:L1, Oct 2013.

[84] K. Grover, S. Fairhurst, B. F. Farr, I. Mandel, C. Rodriguez, T. Sidery, and A. Vecchio. Comparison of gravitational wave detector network sky localization approximations. *Phys. Rev.*, D89(4):042004, 2014.

[85] J. W. T. Hessels. A radio pulsar spinning at 716 Hz. *Science*, 311(5769):1901–1904, Mar 2006.

[86] S. Hooper, S. K. Chung, J. Luan, D. Blair, Y. Chen, and L. Wen. Summed parallel infinite impulse response (SPIIR) filters for low-latency gravitational wave detection. *Phys. Rev.*, D86:024012, 2012.

[87] E. J. Howell, K. Ackley, A. Rowlinson, and D. Coward. Joint gravitational wave – gamma-ray burst detection rates in the aftermath of gw170817. *Monthly Notices of the Royal Astronomical Society*, 485(1):1435–1447, Feb 2019.

[88] R. A. Hulse and J. H. Taylor. Discovery of a pulsar in a binary system. *ApJ Letters*, 195:L51–L53, Jan. 1975.

[89] J. Isern, E. Garcia-Berro, J. Guerrero, J. A. Lobo, and J. M. Ibáñez. *Gravitational waves from the merging of white dwarfs*, pages 295–298. Springer Netherlands, Dordrecht, 2003.

[90] M. Isi, R. Smith, S. Vitale, T. J. Massinger, J. Kanner, and A. Vajpeyi. Enhancing confidence in the detection of gravitational waves from compact binaries via Bayesian model comparison. 2018.

[91] J. Aasi et al. Gravitational waves from known pulsars: results from the initial detector era. *The Astrophysical Journal*, 785(2):119, Apr 2014.

[92] J. Aasi et al. Methods and results of a search for gravitational waves associated with gamma-ray bursts using the GEO 600, LIGO, and Virgo detectors. *Phys. Rev. D*, 89(12):122004, June 2014.

[93] J. Bloom et al. Observations of the Naked-Eye GRB 080319B: Implications of Nature's Brightest Explosion. *ApJ*, 691(1):723–737, Jan. 2009.

[94] S. Kalita and B. Mukhopadhyay. Continuous gravitational wave from magnetized white dwarfs. In *IAU Symposium 357: White Dwarfs as probes of fundamental physics and tracers of planetary, stellar and galactic evolution Hilo, Big Island, Hawaii, United States, October 21-25, 2019*, 2020.

[95] J. B. Kanner, T. B. Littenberg, N. Cornish, M. Millhouse, E. Xhakaj, F. Salemi, M. Drago, G. Vedovato, and S. Klimenko. Leveraging waveform complexity for confident detection of gravitational waves. *Phys. Rev.*, D93(2):022002, 2016.

[96] E. F. Keane, B. W. Stappers, M. Kramer, and A. G. Lyne. On the origin of a highly dispersed coherent radio burst. *Monthly Notices of Royal Astronomical Society*, 425(1):L71–L75, Sept. 2012.

[97] S. Khan, S. Husa, M. Hannam, F. Ohme, M. Pürrer, X. J. Forteza, and A. Bohé. Frequency-domain gravitational waves from nonprecessing black-hole binaries. II. A phenomenological model for the advanced detector era. *Physical Review D*, 93(4), Feb 2016.

[98] R. W. Klebesadel, I. B. Strong, and R. A. Olson. Observations of gamma-ray bursts of cosmic origin. *ApJ Letters*, 182:L85, June 1973.

[99] S. Klimenko, G. Vedovato, M. Drago, G. Mazzolo, G. Mitselmakher, C. Pankow, G. Prodi, V. Re, F. Salemi, and I. Yakushin. Localization of gravitational wave sources with networks of advanced detectors. *Phys. Rev.*, D83:102001, 2011.

[100] S. Klimenko, G. Vedovato, M. Drago, F. Salemi, V. Tiwari, G. A. Prodi, C. Lazzaro, K. Ackley, S. Tiwari, C. F. Da Silva, and G. Mitselmakher. Method for detection and reconstruction of gravitational wave transients with networks of advanced detectors. *Phys. Rev. D*, 93:042004, Feb 2016.

[101] S. Klimenko, I. Yakushin, A. Mercer, and G. Mitselmakher. Coherent method for detection of gravitational wave bursts. *Class. Quant. Grav.*, 25:114029, 2008.

[102] K. Kotake. Multiple physical elements to determine the gravitational-wave signatures of core-collapse supernovae. *Comptes Rendus Physique*, 14(4):318–351, Apr. 2013.

[103] L. Kreidberg, C. D. Bailyn, W. M. Farr, and V. Kalogera. Mass measurements of black holes in x-ray transients: Is there a mass gap? *The Astrophysical Journal*, 757(1):36, Sep 2012.

[104] L. Spitler et al. A repeating fast radio burst. *Nature*, 531(7593):202–205, Mar. 2016.

[105] M. Leng and D. Giannios. Testing the neutrino annihilation model for launching grb jets. *Monthly Notices of the Royal Astronomical Society: Letters*, 445(1):L1–L5, Aug 2014.

[106] A. Levan. *Gamma-Ray Bursts*. 2514-3433. IOP Publishing, 2018.

[107] Y. Levin and M. van Hoven. On the excitation of f modes and torsional modes by magnetar giant flares. *Monthly Notices of Royal Astronomical Society*, 418(1):659–663, Nov. 2011.

[108] L.-X. Li and B. Paczyński. Transient events from neutron star mergers. *ApJ Letters*, 507(1):L59–L62, Nov. 1998.

[109] LIGO and Virgo collaborations. *LIGO/Virgo O3 Public Alerts*, (accessed June 25, 2020). `https://gracedb.ligo.org/superevents/public/O3/`.

[110] LIGO and Virgo collaborations. *Suspending LIGO/Virgo Observing run 3*, (accessed June 25, 2020). `https://www.ligo.caltech.edu/news/ligo20200326`.

[111] LIGO Collaboration. *Gravitational Wave Open Science Center: GW150914*, (accessed June 25, 2020). `https://www.gw-openscience.org/events/GW150914/`.

[112] LIGO Scientific Collaboration. *Science summary of GW150914*, (accessed February 27, 2020). `https://www.ligo.org/science/Publication-GW150914/`.

[113] M. Lingam and A. Loeb. Fast radio bursts from extragalactic light sails. *ApJ Letters*, 837(2):L23, Mar. 2017.

[114] T. B. Littenberg and N. J. Cornish. Bayesian inference for spectral estimation of gravitational wave detector noise. *Phys. Rev.*, D91(8):084034, 2015.

[115] T. B. Littenberg, J. B. Kanner, N. J. Cornish, and M. Millhouse. Enabling high confidence detections of gravitational-wave bursts. *Phys. Rev.*, D94(4):044050, 2016.

[116] D. R. Lorimer, M. Bailes, M. A. McLaughlin, D. J. Narkevic, and F. Crawford. A bright millisecond radio burst of extragalactic origin. *Science*, 318(5851):777, Nov. 2007.

[117] R. Lynch, S. Vitale, R. Essick, E. Katsavounidis, and F. Robinet. Information-theoretic approach to the gravitational-wave burst detection problem. *Physical Review D*, 95(10), May 2017.

[118] D. C. M., D. Rickles, and R. Jurgen. *The role of gravitation in physics report from the 1957 Chapel Hill Conference*. Ed. Open Access, 2011.

[119] M. Ackermann et al. Fermi observations of GRB 090510: A short-hard gamma-ray burst with an additional, hard power-law component from 10 keV to GeV energies. *ApJ*, 716(2):1178–1190, June 2010.

[120] M. Zevin et al. Gravity spy: integrating advanced LIGO detector characterization, machine learning, and citizen science. *Classical and Quantum Gravity*, 34(6):064003, Feb 2017.

[121] G. A. MacLachlan, A. Shenoy, E. Sonbas, K. S. Dhuga, B. E. Cobb, T. N. Ukwatta, D. C. Morris, A. Eskandarian, L. C. Maximon, and W. C. Parke. Minimum variability time-scales of long and short grbs. *Monthly Notices of the Royal Astronomical Society*, 432(2):857–865, 2013.

[122] E. P. Mazets, S. V. Golentskii, V. N. Ilinskii, R. L. Aptekar, and I. A. Guryan. Observations of a flaring X-ray pulsar in Dorado. *Nature*, 282(5739):587–589, Dec. 1979.

[123] J. Melinder, T. Dahlen, L. Mencía Trinchant, G. Östlin, S. Mattila, J. Sollerman, C. Fransson, M. Hayes, E. Kankare, and S. Nasoudi-Shoar. The rate of supernovae at redshift 0.1-1.0. The Stockholm VIMOS Supernova Survey III. *Astronomy & Astrophysics*, 545:A96, Sept. 2012.

[124] C. Messick et al. Analysis framework for the prompt discovery of compact binary mergers in gravitational-wave data. *Phys. Rev.*, D95(4):042001, 2017.

[125] B. D. Metzger. Welcome to the multi-messenger era! Lessons from a neutron star merger and the landscape ahead. 2017.

[126] A. A. Michelson and E. W. Morley. On the relative motion of the Earth and of the luminiferous ether. *Sidereal Messenger*, 6:306–310, Nov. 1887.

[127] C. W. Misner, K. S. Thorne, and J. A. Wheeler. *Gravitation*. Princeton University Press, 2017.

[128] M. Modjaz. Stellar forensics with the supernova-GRB connection. *Astron. J.*, 332:434, 2011.

[129] K. Mogushi, M. Cavaglià, and K. Siellez. Jet geometry and rate estimate of coincident gamma-ray burst and gravitational-wave observations. *The Astrophysical Journal*, 880(1):55, Jul 2019.

[130] B. Müller, H.-T. Janka, and A. Marek. A new multi-dimensional general relativistic neutrino hydrodynamics code of core-collapse supernovae. III. Gravitational wave signals from supernova explosion models. *ApJ*, 766(1):43, Mar. 2013.

[131] E. Muller, M. Rampp, R. Buras, H.-T. Janka, and D. H. Shoemaker. Toward gravitational wave signals from realistic core-collapse supernova models. *The Astrophysical Journal*, 603(1):221–230, Mar 2004.

[132] J. W. Murphy, C. D. Ott, and A. Burrows. A model for gravitational wave emission from neutrino-driven core-collapse supernovae. *ApJ*, 707(2):1173–1190, Dec. 2009.

[133] P. Mészáros. Gamma-ray bursts. *Reports on Progress in Physics*, 69(8):2259–2321, Jul 2006.

[134] R. J. Nemiroff. A century of gamma ray burst models. *Comments on Astrophysics*, 17:189, Jan. 1994.

[135] A. H. Nitz, T. Dal Canton, D. Davis, and S. Reyes. Rapid detection of gravitational waves from compact binary mergers with PyCBC Live. *Phys. Rev.*, D98(2):024050, 2018.

[136] Nitz, A. et al. gwastro/pycbc: 1.12.3 release, Sept. 2018.

[137] C. D. Ott. The gravitational-wave signature of core-collapse supernovae. *Classical and Quantum Gravity*, 26(6):063001, Feb 2009.

[138] Ott C. D., Santamaria, L. Gravitational wave emission from accretion disk instabilities. Technical report, 2013.

[139] D. J. Ottaway, P. Fritschel, and S. J. Waldman. Impact of upconverted scattered light on advanced interferometric gravitational wave detectors. *Opt. Express*, 20(8):8329–8336, Apr 2012.

[140] D. Palaniswamy, Y. Li, and B. Zhang. Are there multiple populations of fast radio bursts? *ApJ Letters*, 854(1):L12, Feb. 2018.

[141] F. Pannarale, E. Berti, K. Kyutoku, B. D. Lackey, and M. Shibata. Gravitational-wave cutoff frequencies of tidally disruptive neutron star-black hole binary mergers. *Phys. Rev. D*, 92(8):081504, Oct. 2015.

[142] F. Pannarale, R. Macas, and P. J. Sutton. Bayesian inference analysis of unmodelled gravitational-wave transients. *Classical and Quantum Gravity*, 36(3):035011, Jan 2019.

[143] F. Pannarale and F. Ohme. Prospects for joint gravitational-wave and electromagnetic observations of neutron star-black hole coalescing binaries. *The Astrophysical Journal*, 791(1):L7, Jul 2014.

[144] Patrick J Sutton et al. X-pipeline: an analysis package for autonomous gravitational-wave burst searches. *New Journal of Physics*, 12(5):053034, May 2010.

[145] T. Piran. Gamma-ray bursts and the fireball model. *Physics Reports*, 314(6):575 – 667, 1999.

[146] A. L. Piro and E. Pfahl. Fragmentation of collapsar disks and the production of gravitational waves. *The Astrophysical Journal*, 658(2):1173–1176, Apr 2007.

[147] Planck Collaboration. Planck 2015 results. XIII. Cosmological parameters. *Astronomy and Astrophysics*, 594:A13, Sept. 2016.

[148] S. Privitera, S. R. P. Mohapatra, P. Ajith, K. Cannon, N. Fotopoulos, M. A. Frei, C. Hanna, A. J. Weinstein, and J. T. Whelan. Improving the sensitivity of a search for coalescing binary black holes with nonprecessing spins in gravitational wave data. *Phys. Rev.*, D89(2):024003, 2014.

[149] D. Radice, A. Perego, F. Zappa, and S. Bernuzzi. GW170817: Joint constraint on the neutron star equation of state from multimessenger observations. *ApJ Letters*, 852(2):L29, Jan. 2018.

[150] M. J. Rees and P. Meszaros. Unsteady outflow models for cosmological gamma-ray bursts. *ApJ Letters*, 430:L93, Aug. 1994.

[151] D. E. Reichart. GRB 970228 revisited: Evidence for a supernova in the light curve and late spectral energy distribution of the afterglow. *ApJ Letters*, 521(2):L111–L115, Aug. 1999.

[152] Robert Shofield et al. *aLOG:37630*, (accessed February 27, 2020). `https://alog.ligo-wa.caltech.edu/aLOG/index.php?callRep=37630`.

[153] X. Roca-Maza and N. Paar. Nuclear equation of state from ground and collective excited state properties of nuclei. *Progress in Particle and Nuclear Physics*, 101:96–176, Jul 2018.

[154] S. Chatterjee et al. A direct localization of a fast radio burst and its host. *Nature*, 541(7635):58–61, Jan. 2017.

[155] S. Chatterji et al. Coherent network analysis technique for discriminating gravitational-wave bursts from instrumental noise. *Phys. Rev.*, D74:082005, 2006.

[156] B. S. Sathyaprakash and B. F. Schutz. Physics, astrophysics and cosmology with gravitational waves. *Living Rev. Rel.*, 12:2, 2009.

[157] P. R. Saulson. Interferometric gravitational wave detectors. *International Journal of Modern Physics D*, 27(7):1840001, Jan. 2018.

[158] B. F. Schutz. Determining the Hubble constant from gravitational wave observations. *Nature*, 323(6086):310–311, Sept. 1986.

[159] B. F. Schutz. *A first course in general relativity*. Cambridge University Press, 2018.

[160] A. Shahmoradi and R. J. Nemiroff. Short versus long gamma-ray bursts: a comprehensive study of energetics and prompt gamma-ray correlations. *Monthly Notices of Royal Astronomy*, 451(1):126–143, July 2015.

[161] A. Shahmoradi and R. J. Nemiroff. A catalog of redshift estimates for 1366 BATSE long-duration gamma-ray bursts: Evidence for strong selection effects on the phenomenological prompt gamma-ray correlations. *arXiv e-prints*, page arXiv:1903.06989, Mar. 2019.

[162] N. Stone, A. Loeb, and E. Berger. Pulsations in short gamma ray bursts from black hole-neutron star mergers. *Phys. Rev. D*, 87(8):084053, Apr. 2013.

[163] E. Stopnitzky and S. Profumo. Gravitational waves from gamma-ray pulsar glitches. *Astrophys. J.*, 787:114, 2014.

[164] H. Sun, B. Zhang, and H. Gao. X-ray counterpart of gravitational waves due to binary neutron star mergers: Light curves, luminosity function, and event rate density. *ApJ*, 835(1):7, Jan. 2017.

[165] P. J. Sutton. A rule of thumb for the detectability of gravitational-wave bursts. *arXiv e-prints*, page arXiv:1304.0210, Mar. 2013.

[166] P. J. Sutton. Reconstructing the gravitational-wave signals of relativistic transients. *In preparation*, 2020.

[167] J. Sylvestre. Time-frequency detection algorithm for gravitational wave bursts. *Phys. Rev. D*, 66:102004, Nov 2002.

[168] T. Galama et al. An unusual supernova in the error box of the γ-ray burst of 25 April 1998. *Nature*, 395(6703):670–672, Oct. 1998.

[169] Y. T. Tanaka, T. Terasawa, N. Kawai, A. Yoshida, I. Yoshikawa, Y. Saito, T. Takashima, and T. Mukai. Comparative study of the initial spikes of soft gamma-ray repeater giant flares in 1998 and 2004 observed with GEOTAIL: Do magnetospheric instabilities trigger large-scale fracturing of a magnetar's crust? *The Astrophysical Journal*, 665(1):L55–L58, Jul 2007.

[170] The LIGO Scientific Collaboration and the Virgo Collaboration and the KAGRA Collaboration. Prospects for observing and localizing gravitational-wave transients with Advanced LIGO, Advanced Virgo and KAGRA, 2013.

[171] S. A. Usman et al. The PyCBC search for gravitational waves from compact binary coalescence. *Class. Quant. Grav.*, 33(21):215004, 2016.

[172] M. H. P. M. van Putten. Gravitational waveforms of kerr black holes interacting with high-density matter. *The Astrophysical Journal*, 684(2):L91–L94, Aug 2008.

[173] M. H. P. M. van Putten and A. Levinson. Theory and astrophysical consequences of a magnetized torus around a rapidly rotating black hole. *ApJ*, 584(2):937–953, Feb. 2003.

[174] J. Veitch and A. Vecchio. Bayesian coherent analysis of in-spiral gravitational wave signals with a detector network. *Phys. Rev.*, D81:062003, 2010.

[175] D. Wanderman and T. Piran. The rate, luminosity function and time delay of non-Collapsar short GRBs. *Monthly Notices of the Royal Astronomical Society*, 448(4):3026–3037, 03 2015.

[176] L. Wang, D. A. Howell, P. Hoflich, and J. C. Wheeler. Bipolar supernova explosions. *The Astrophysical Journal*, 550(2):1030–1035, Apr 2001.

[177] M. Was, P. J. Sutton, G. Jones, and I. Leonor. Performance of an externally triggered gravitational-wave burst search. *Physical Review D*, 86(2), Jul 2012.

[178] A. Williamson, C. Biwer, S. Fairhurst, I. Harry, E. Macdonald, D. Macleod, and V. Predoi. Improved methods for detecting gravitational waves associated with short gamma-ray bursts. *Physical Review D*, 90(12), Dec 2014.

[179] S. E. Woosley. Gamma-ray bursts from stellar mass accretion disks around black holes. *ApJ Letters*, 405:273, Mar. 1993.

[180] S. E. Woosley and A. Heger. The progenitor stars of gamma-ray bursts. *The Astrophysical Journal*, 637(2):914–921, Feb 2006.

[181] F. Zappa, S. Bernuzzi, F. Pannarale, M. Mapelli, and N. Giacobbo. Black hole remnants from black hole-neutron star mergers. *Physical Review Letters*, 123(4), Jul 2019.